

Dynamical Masses of Low Mass Spectroscopic Binary Stars

A Dissertation Presented

by

Chad Frederick Bender

to

The Graduate School

in Partial fulfillment of the

Requirements

for the Degree of

Doctor of Philosophy

in

Physics

Stony Brook University

December 2006

Stony Brook University

The Graduate School

Chad Frederick Bender

We, the dissertation committee for the above candidate for the
Doctor of Philosophy degree,
hereby recommend acceptance of this dissertation.

Dr. Michal Simon (Thesis Advisor)

Professor, Department of Physics and Astronomy

Dr. Frederick Walter (Chair)

Professor, Department of Physics and Astronomy

Dr. James Lattimer

Professor, Department of Physics and Astronomy

Dr. Gene Sprouse

Professor, Department of Physics and Astronomy

Dr. David Latham

Senior Astronomer, Smithsonian Astrophysical Observatory

This dissertation is accepted by the Graduate School.

Dean of the Graduate School

Abstract of the Dissertation
**Dynamical Masses of Low Mass
Spectroscopic Binary Stars**

by

Chad Frederick Bender

Doctor of Philosophy

in

Physics

Stony Brook University

2006

Theoretical models of star formation and stellar evolution have improved significantly over the past few decades. Their accuracy, however, is still limited. I present three investigations using high resolution spectroscopy in the infrared to make dynamical measurements of nearby stars, with the goal of providing useful constraints for improving models.

The Hyades cluster contains a well defined stellar sample with constrained age and metallicity, in a distinct star forming region, and is an excellent laboratory for testing models of star formation. I obtained *H*-band spectra of 32 spectroscopic binary stars with low mass companions. In 27 of these systems I detected the companion and derived the companion-to-primary mass ratio.

Together with visible light measurements from Latham and colleagues, my results indicate a mass ratio distribution for Hyades spectroscopic binaries that decreases towards smaller mass ratios. If combined with the mass ratios derived by Patience and colleagues for a sample of wide Hyades binaries, the measured distribution is consistent with a flat distribution.

Gl569 is a nearby multiple system believed to contain an M-star, Gl569A, and a brown dwarf binary, Gl569B. Colleagues and I observed the system with high spectral and angular resolution, intending to measure the dynamical masses of the brown dwarf binary. My analysis did not yield this result, but instead revealed two surprises. First, at age ~ 100 Myr, the system is younger than reported by earlier investigators. Second, the spectroscopic and photometric results support earlier indications that Gl569B is actually a hierarchical brown dwarf triple rather than a binary, and suggest that the three components have roughly equal masses of $\sim 0.04 M_{\odot}$.

ρ Coronae Borealis was among the first stars identified with a candidate extra-solar planet companion, but later reports suggested the companion is really a low-mass star with mass $0.14 \pm 0.05 M_{\odot}$. Colleagues and I did not detect evidence of such a companion in high resolution spectra, and placed upper bounds on the flux ratio at $1.6 \mu\text{m}$ of less than 0.0024 and 0.005 at the 90% and 99% confidence levels, respectively. Using an H -band mass-luminosity relationship, the corresponding upper limits on the companion mass are $0.11 M_{\odot}$ and $0.15 M_{\odot}$.

Contents

List of Figures	ix
List of Tables	xi
Acknowledgments	xiii
1 Introduction	1
1.1 Scientific Motivation	1
1.2 Spectroscopic Binary Stars	3
1.3 Outline of the Dissertation	4
Bibliography	6
2 Techniques for Measuring Spectroscopic Binary Stars	7
2.1 Dynamical Mass Ratios and The Two-Dimensional Cross-Correlation Analysis	7
2.2 Spectroscopic Observations and Data Reduction	11
2.2.1 NIRSPEC Spectroscopy	11
2.2.2 CSHELL Spectroscopy	13
2.3 Spectral Type Templates	16

	Bibliography	20
3	Dynamical Mass Ratio Distribution of Spectroscopic Binaries in the Hyades Cluster	30
3.1	Introduction	30
3.2	The Hyades Binary Sample	32
3.3	Observations and Data Reduction	34
3.4	Results	36
3.4.1	Velocity Measurements: Slow Rotators	36
3.4.2	Velocity Measurements: Rapid Rotators	39
3.4.3	Non-detections	39
3.4.4	Double Lined Spectroscopic Binary Solutions	40
3.5	Mass Ratio Distribution	42
3.6	Discussion	44
3.6.1	Component Masses	44
3.6.2	Angular Momentum of Spectroscopic Binaries	45
3.6.3	Comparison with Wide Binary Population	47
3.7	Summary and Suggestions for Future Work	49
	Bibliography	53
4	The G1569 Multiple System	80
4.1	Introduction	80
4.2	Observations and Processing	81
4.2.1	NIRSPEC Spectroscopy	81

4.2.2	NIRC2 Imaging	81
4.3	Results: GL 569A	82
4.4	Results: Gl569B	84
4.4.1	Photometry, Astrometry, and Orbital Parameters of Gl569B as a Visual Binary	84
4.4.2	Velocities of the Gl569B Spectroscopic Binary	86
4.4.3	Dynamical Masses of the Components	89
4.5	Discussion	93
4.5.1	The Gl569 Quadruple?	93
4.5.2	The Lithium Test	95
4.6	Summary and Suggestions for Future Work	96
	Bibliography	99
5	An Upper Bound on the 1.6 μm Flux Ratio of the Companion to ρ Coronae Borealis	115
5.1	Introduction	115
5.2	Observations and Data Reduction	116
5.3	The Companion-to-Primary Flux Ratio of ρ Coronae Borealis	118
5.4	Estimate of the Flux Ratio Upper Bound	120
5.4.1	Model Binaries	120
5.4.2	Flux Ratio Upper Bound	122
5.5	Discussion	123
5.6	Summary	124

	Bibliography	127
6	Closing Remarks	134

List of Figures

2.1	Synthetic spectra for a sample low mass binary	23
2.2	NIRSPEC spectrum of the A0 star HD133772 for orders 45–53.	24
2.3	NIRSPEC order 46 templates	25
2.4	NIRSPEC order 47 templates	26
2.5	NIRSPEC order 48 templates	27
2.6	NIRSPEC order 49 templates	28
2.7	CSHELL templates	29
3.1	Distribution of H -mag for the Hyades SB1 sample	63
3.2	Velocity reference frame comparison	64
3.3	Distribution of q_{\min} for infrared SB2 detections and non-detections	65
3.4	Velocity versus phase curves for Hyades SB2s, R.A. 3^h59^m to 4^h26^m	66
3.5	Velocity versus phase curves for Hyades SB2s, R.A. 4^h26^m to 4^h33^m	67
3.6	Velocity versus phase curves for Hyades SB2s, R.A. 4^h34^m to 5^h59^m	68
3.7	Measured Hyades q_{\min} versus q	69
3.8	Measures Hyades α versus q	70
3.9	Measured Hyades SB2 mass ratio distribution	71

3.10	Smoothed Hyades SB2 mass ratio distribution	72
3.11	Distribution of Hyades SB2 primary masses	73
3.12	Distribution of Hyades SB2 secondary masses	74
3.13	IMF of Hyades SB2 secondary masses	75
3.14	J/M for Hyades SB2s	76
3.15	Mass ratio distribution for Hyades SB2s and speckle binaries	77
3.16	J/M for Hyades speckle binaries	78
3.17	J/M for Hyades SB2s and speckle binaries	79
4.1	The position of Gl569B with respect to A	105
4.2	Gl569A compared to theoretical isochrones	106
4.3	Gl569A on a color-magnitude diagram of the Pleiades	107
4.4	NIRC2 adaptive optics images of Gl569Ba and Bb at H and K	108
4.5	The astrometric orbit of Gl569Bb with respect to Ba	109
4.6	A sample profile of the AO angularly resolved Gl569B spectrum	110
4.7	Angularly resolved spectra of Gl569Ba and Bb	111
4.8	Velocity versus orbital phase measurements for Gl569Ba and Bb	112
4.9	Gl569Bb compared to theoretical isochrones	113
4.10	Gl569Ba and Bb velocity difference versus orbital phase	114
5.1	NIRSPEC spectrum of ρ CrB from 2001 June 2 for orders 46–49.	129
5.2	Sample primary spectra from the 2001 January 7 model set.	130
5.3	Distribution of derived flux ratios in a sample of model binaries	131
5.4	Measured flux ratio probabilities	132
5.5	Absolute H -band magnitude versus mass	133

List of Tables

2.1	NIRSPEC Template Library	21
2.2	CSHELL Template Library	22
3.1	Hyades SB1 Sample	54
3.1	Hyades SB1 Sample	55
3.2	Log of Hyades Observations	56
3.2	Log of Hyades Observations	57
3.2	Log of Hyades Observations	58
3.3	Measured Mass Ratios for IR SB2s	59
3.3	Measured Mass Ratios for IR SB2s	60
3.4	Derived Component Masses for IR SB2s	61
3.4	Derived Component Masses for IR SB2s	62
4.1	Log of Gl569 Observations	100
4.2	Astrometry of Gl569AB	100
4.3	Radial Velocity Measurements of Gl569A	101
4.4	Photometry and Astrometry of Gl569B	102
4.5	Orbital Parameters of Gl569Bab	103

4.6	Radial Velocity Measurements of Gl569Bab	104
5.1	Log of ρ CrB Observations	128
5.2	Measured Companion-to-Primary Flux Ratios at 1.6 μm	128

Acknowledgments

I must begin by wholeheartedly thanking my advisor, Mike Simon. Through his guidance and support, Mike contributed immeasurably to my growth as an astronomer and as a person over the past five years. I will miss the easy opportunity to tap into his considerable knowledge about science and life that our frequent conversations have offered. I sincerely hope that we continue to collaborate for years to come.

I thank Fred Walter for chairing my dissertation committee and for mentoring me during my time at Stony Brook through numerous courses and other events. I also thank Jim Lattimer and Gene Sprouse for serving on my committee and for providing many suggestions that strengthened the content of my research. I particularly thank Dave Latham, not only for serving on my defense committee, but also for his active participation throughout the Hyades research. His contribution of decades worth of Hyades observations at visible wavelengths made possible my small addition in the infrared.

I am grateful to a number of other members of the astronomical community for the assistance they have provided me over the years. Deane Peterson was always willing and able to answer all manner of stellar atmospheres questions

that I posed to him. Lisa Prato provided the Hyades observations at Keck II, as well as considerable advice on all aspects of NIRSPEC data. Alan Tokunaga facilitated some early observations of Gl569 with Subaru. Tsevi Maze's insights into the ρ CrB, Gl569, and Hyades analyses were invaluable. Peter McCullough guided me through my first astronomical research at Illinois and is responsible for my fastidiously neat lab notebook habit. Jake Winemiller's energetic instruction throughout my years in Lincoln contributed significantly to my early astronomy education and played a large role in my decision to pursue this career.

My sister Amy has provided a much needed glimpse of sanity over the years, and I offer her my best wishes as she pursues her own career in astronomy. I look forward to future collaborations where I will surely benefit from her brilliance. My parents, John and Gail, deserve a special acknowledgment and thanks for their unwavering encouragement in all of my pursuits, but particularly throughout my education. Finally, I must thank Lynn for sticking with me during all of these long distance years. She inspired me to persevere through it all, and I am a better person because of her.

Chapter 1

Introduction

1.1 Scientific Motivation

Our understanding of the processes behind the formation and evolution of stars has improved over the past few decades, but is still limited in some respects. Numerical models of these processes are rapidly becoming very sophisticated, and have outpaced the observations that are necessary to test them. Understanding the formation of binary stars is of particular interest in creating a complete picture of star formation. Observations have shown for some time that the majority of stars in the solar neighborhood are binaries (Duquennoy & Mayor, 1991; Abt & Levy, 1976). These systems probably formed through the process of fragmentation, wherein multiple proto-stellar cores were created during the collapse of a molecular cloud. Bate & Bonnell (1997) simulated this process to produce isolated binary systems, and found that the mass ratio with which a binary forms is correlated with the separation of the two components, and hence the orbital period of the system. They determined that binaries with long periods are

expected to have small mass ratios, while binaries with short periods should have components of more equal mass. For a sample of medium to long period binaries, Duquennoy & Mayor (1991) derived a mass ratio distribution that increases sharply towards small mass ratios. More recently, Mazeh et al. (2003) measured a flat mass ratio distribution for a sample of short period binaries. Bate et al. (2002) simulated the collapse of an entire molecular cloud into a cluster and found that fragmentation does not produce binaries with separation less than about 10 AU. Instead, these close systems form through dynamical interactions, which preferentially create binaries with components of similar masses. Additional direct observations of star forming regions and clusters are needed to test these and future results, particularly as the simulations become more realistic.

Detailed models of stellar evolution are also now widely available (e.g. Vandenberg et al., 2006; Baraffe et al., 2003, 1998; Yi et al., 2001; Burrows et al., 1997), and are routinely used to estimate the physical properties of stars (e.g. mass, luminosity, temperature) from photometric measurements and low resolution spectroscopy. For stars with young ages ($\lesssim 100$ Myr) and low masses ($\lesssim 0.5 M_{\odot}$), however, the models yield discrepant results because few observations are available in these regimes to provide constraints. At a basic level, these models are dependent on five stellar parameters: mass, age, initial helium mass fraction, metallicity, and the characteristic mixing length (Berthomieu et al., 2002). The direct measurement of some or all of these parameters for a variety of stars will provide the constraints necessary for modelers to improve the accuracy of their predictions. Observations of binary stars can provide dynamical mass measure-

ments, which are very difficult to obtain for single stars.

Here I present results from observations of spectroscopic binary stars. Some of these observations were designed to test our understanding of binary star formation processes. Others were intended to provide input for stellar evolution models. The observations are connected through the use of high resolution infrared spectroscopy. This technology has only become widely available in the past decade, and provides the opportunity to directly detect low mass companions that cannot be observed in the visible.

1.2 Spectroscopic Binary Stars

Observations of spectroscopic binary stars provide instantaneous measurements of the radial component of binary motion, in the form of a Doppler shift in the spectral lines. Measuring this velocity can yield many parameters of the binary orbit, including P , e , T_0 , ω , K_1 , K_2 , and γ : the period, eccentricity, time of periastron passage, longitude of periastron, semi-major amplitude of the primary, and secondary, and the systemic, or center-of-mass, velocity. In a single-lined spectroscopic binary (SB1), where only one component of the binary is detected in the observed spectrum, all of the parameters except for K_2 can still be determined.

From Heintz (1978), the radial velocity of a binary component, at a specified time, is given by

$$V_{1,2} = \gamma + K_{1,2}[e \cos \omega + \cos(v + \omega)], \quad (1.1)$$

where v is the true anomaly, or the orbital polar angle measured relative to periastron, and is determined from P , T_0 , and the time of the observation. Given sufficient velocity measurements, Eq. 1.1 can be solved for each of the listed orbital parameters. The semi-major axis of a binary, a , is easily calculated as

$$a_{1,2} \sin i = 13751 K_{1,2} P \sqrt{(1 - e^2)}, \quad (1.2)$$

with a and K in km, P in days, and $a = a_1 + a_2$. Spectroscopic binary orbits, however, do not provide information about the orbital inclination, i . By substituting into Kepler's third law, SB1s yield the mass function,

$$f(M) = \frac{M_2^3}{(M_1 + M_2)^2} \times \sin^3 i = 1.036 \times 10^{-7} K_1^3 P (1 - e^2)^{3/2}, \quad (1.3)$$

where the inclination is inseparable from the masses. In a double-lined spectroscopic binary (SB2), where lines from both components are detected, the mass ratio, q can be calculated dynamically as, $q = K_1 / K_2 = M_2 / M_1$.

1.3 Outline of the Dissertation

In the chapters that follow, I present three investigations using high resolution spectroscopy in the infrared to make dynamical measurements of nearby stars. First, though, in Chapter 2 I describe the aspects that are common to all three investigations. I discuss the principles behind the analysis of binary spectra, and the software and calibration spectra used in later chapters. I also describe the infrared spectrometers which make possible the detection of binaries

with low mass companions as SB2s. In Chapter 3, I describe a study to measure a dynamical mass ratio distribution for spectroscopic binaries in the Hyades cluster. My results, in context with SB2s observed in the visible and wide binaries observed with speckle imaging, provide important diagnostics for improving theories of binary formation and for understanding the star formation history of the Hyades. In Chapter 4, I present an analysis of the Gl569 multiple system that I carried out in collaboration with M. Simon and L. Prato, and which is also reported in Simon et al. (2006). We began the investigation in order to provide precise dynamical mass measurements of brown dwarfs to constrain models of stellar evolution. Our results only partially accomplished this, but also strongly suggest problems with models of more massive stars. In Chapter 5, I describe an attempt to directly detect the candidate extra-solar planet companion to the nearby star ρ CrB, which I undertook with M. Simon, L. Prato, T. Mazeh, and S. Zucker; these results also appear in Bender et al. (2005). The analysis uses stellar evolution models to constrain the companion mass, and demonstrates the very small secondary-to-primary flux ratios to which our technique for analyzing binary spectra is sensitive. Finally, in Chapter 6, I remark on the future prospects for studying low mass stars, brown dwarfs, and planets with high resolution spectroscopy in the infrared.

Bibliography

- Abt, H. A. & Levy, S. G. 1976, *ApJS*, 30, 273
- Baraffe, I., Chabrier, G., Allard, F., & Hauschildt, P. H. 1998, *A&A*, 337, 403
- Baraffe, I., Chabrier, G., Barman, T. S., Allard, F., & Hauschildt, P. H. 2003, *A&A*, 402, 701
- Bate, M. R. & Bonnell, I. A. 1997, *MNRAS*, 285, 33
- Bate, M. R., Bonnell, I. A., & Bromm, V. 2002, *MNRAS*, 336, 705
- Bender, C., Simon, M., Prato, L., Mazeh, T., & Zucker, S. 2005, *AJ*, 129, 402
- Berthomieu, G., Morel, P., Provost, J., & Thevenin, F. 2002, in *ASP Conf. Ser. 274*, ed. T. Lejeune & J. Fernandes, 199
- Burrows, A., Marley, M., Hubbard, W. B., Lunine, J. I., Guillot, T., Saumon, D., Freedman, R., Sudarsky, D., & Sharp, C. 1997, *ApJ*, 491, 856
- Duquennoy, A. & Mayor, M. 1991, *A&A*, 248, 485
- Heintz, W. D. 1978, *Double Stars* (Revised ed. Dordrecht; Reidel)
- Mazeh, T., Simon, M., Prato, L., Markus, B., & Zucker, S. 2003, *ApJ*, 599, 1344
- Simon, M., Bender, C., & Prato, L. 2006, *ApJ*, 644, 1183
- VandenBerg, D. A., Bergbusch, P. A., & Dowler, P. D. 2006, *ApJS*, 162, 375
- Yi, S., Demarque, P., Kim, Y.-C., Lee, Y.-W., Ree, C. H., Lejeune, T., & Barnes, S. 2001, *ApJS*, 136, 417

Chapter 2

Techniques for Measuring Spectroscopic Binary Stars

2.1 Dynamical Mass Ratios and The Two-Dimensional Cross-Correlation Analysis

Determining the mass ratio, $q = M_2/M_1$, of a spectroscopic binary requires detecting both the primary and secondary components of the system, and measuring their radial velocities. Detecting only the primary component results in a single-lined spectroscopic binary (SB1) and yields only the mass function,

$$f(M) = \frac{M_2^3}{(M_1 + M_2)^2} \times \sin^3 i, \quad (2.1)$$

where the masses are inseparable from the inclination, i . Detecting both the primary and the secondary results in a double-lined spectroscopic binary (SB2). The method of calculating the mass ratio of a binary depends on how many detections of the secondary are available and how much is known *a priori* about the system from single-lined or astrometric observations (Mazeh et al., 2002; Wilson, 1941).

Observing a system as an SB1 provides many of its orbital parameters, including P , e , T_0 , ω , K_1 , and γ : the period, eccentricity, time of periastron passage, longitude of periastron, semi-major amplitude of the primary, and the systemic, or center-of-mass, velocity. If these parameters are well determined from SB1 observations, as in the case of the Hyades binaries presented in Chapter 3, they can be fixed when solving the binary as an SB2 and the measurements of the secondary velocity need only constrain the semi-major axis of the secondary, K_2 , to yield the mass ratio, $q = K_1/K_2$. This is a useful procedure when many SB1 observations, but only a few SB2 observations, are available.

If the γ velocity is known, but the other orbital parameters are unconstrained (e.g., an SB1 solution with a large scatter in the velocity measurements, or a long period system with observations at only a small range of phases), each observation of the system as an SB2 yields a measurement of q , given by

$$q = -\frac{V_1 - \gamma}{V_2 - \gamma}, \quad (2.2)$$

where V_1 and V_2 are the primary and secondary radial velocities, respectively. If, however, the systemic velocity is not known *a priori*, then two pairs of radial velocity measurements taken at different epochs, i and j , give the mass ratio

$$q = -\frac{V_{1,i} - V_{1,j}}{V_{2,i} - V_{2,j}}. \quad (2.3)$$

Neither of these approaches require extensive observations over the entire orbit. Both work best if the measurements are made when the velocity difference between the components is at its maximum. The method shown in Eq. 2.3, in particular, needs measurements at phases such that the velocity differences are large compared to the measurement uncertainties.

Observations of a spectroscopic binary usually provide a single target spectrum containing the blended light of both components. The individual component velocities are measured with a two-dimensional cross-correlation analysis. The target spectrum is cross-correlated against pairs of template spectra, combined at specified flux ratios, $\alpha = F_2/F_1$, and over a range of velocity separations. The template spectra are single stars with known spectral type, and should have a high signal-to-noise ratio. A peak in the calculated correlation surface indicates the primary and secondary velocities. Zucker & Mazeh (1994) developed the TODCOR algorithm to carry out this cross-correlation analysis, and provided it to M. Simon and myself in the form of a binary executable. For a specified pair of template spectra, TODCOR optimizes the velocity separation and the flux ratio to best match the input target spectrum. I developed a similar algorithm, SBCCORR, using the IDL programming language. SBCCORR is capable of simultaneously searching over an additional parameter, the template spectral type, by using multiple templates of varying spectral types for each component. This is useful when the spectral type of one or both of the target SB2 components is unknown. On synthetic test systems and observed binaries SBCCORR yields results that are identical to TODCOR to within the measurement precision.

Detecting both the primary and secondary components of a spectroscopic binary using a cross-correlation analysis is limited by the flux ratio between the components at the wavelength being observed. At visible wavelengths a higher mass primary star is much brighter than a lower mass companion. Figure 2.1 shows synthetic spectra from the library of Lejeune et al. (1997) for stars of $1 M_{\odot}$

and $0.2 M_{\odot}$, with solar metallicity and an age of 1 Gyr. A binary system with such components has a flux ratio that is ~ 10 times larger in the H -band at $1.6 \mu\text{m}$ than in the V -band at $0.55 \mu\text{m}$. The very small V -band flux ratio makes detection of such a system as an SB2 at those wavelengths all but impossible, and so observations in the visible often result in many SB1 detections; only systems with a large flux ratio, and hence q biased towards one, are detected in the visible as SB2s. The much more favorable H -band flux ratio demonstrates that observations of SBs in the infrared can probe the companions in binaries with low q .

Until recently, high resolution spectrometers sensitive in the infrared did not exist, so studies of spectroscopic binaries were carried out in the visible where these instruments have been available for a few decades (*e.g.* Latham et al., 2002; Duquennoy & Mayor, 1991). The infrared spectrometers that now exist allow one to detect the secondary in many known SB1s. Prato et al. (2002) use this technique on pre-main sequence binaries with mass ratios as low as $q = 0.2$; Mazeh et al. (2003) and Bender et al. (2005) demonstrate sensitivity to SB2s with flux ratios as low as $\alpha = 0.04$ and $\alpha = 0.01$, respectively.

An additional limit on SB2 detection is the velocity separation of the primary and secondary components. To measure an SB2 mass ratio with high precision, the uncertainties in the measured velocities should be small relative to the velocity separation of the components. This makes detecting both components in systems with long periods, large eccentricities, or low masses, and hence small orbital velocities, difficult. Furthermore, all systems, even those with large maximum velocity separation, have phases where the velocity separation is at or

near zero; observations at these times contribute very little to a precise SB2 solution. However, pre-existing SB1 solutions can predict phases, and hence epochs, of zero velocity separation, so that observations can be planned at appropriate times.

2.2 Spectroscopic Observations and Data Reduction

The projects that I discuss in later chapters (the Hyades mass ratio distribution in Chapter 3; the Gl569 multiple system in Chapter 4; and the ρ CrB flux ratio in Chapter 5) use data from two spectrometers: NIRSPEC on the Keck II telescope and CSHELL on the NASA IRTF telescope, each in a single observing mode. In this section I describe both instruments, and technical details of the observations and data reduction that are common to all three analyses.

2.2.1 NIRSPEC Spectroscopy

NIRSPEC is the W. M. Keck Observatory's cryogenic cross-dispersed near-infrared spectrograph (McLean et al., 1998, 2000). The spectroscopic detector is a 1024×1024 pixel ALADDIN III InSb array that is sensitive from $0.95 - 5.5 \mu\text{m}$. In its high resolution (echelle) mode, NIRSPEC has a plate scale of $0.''144 \text{ pixel}^{-1}$ in the dispersion direction and $0.''198 \text{ pixel}^{-1}$ in the cross-dispersion direction. NIRSPEC normally operates under natural seeing conditions, but it can also be used behind the Keck adaptive optics (AO) system (Wizinowich et al., 2000), where the AO re-imaging optics reduce the plate scale by a factor of 10.6. This provides the opportunity to resolve spatially the individual components of binary

systems with small angular separation. However, the observed throughput of NIRSPEC with the AO system is $\sim 10\% - 20\%$ of that without AO¹; the signal-to-noise achieved in a given exposure time with AO at, for example, the *H*-band, is about half that achieved without AO.

Colleagues and I used NIRSPEC on the 10 m Keck II telescope to observe ρ CrB in 2001 (see Table 5.1), Gl569 from 2002 through 2005 (see Table 4.1), and the Hyades in 2005 (see Table 3.2). We observed both with and without the AO system. All of the observations used the 2-pixel wide slit and were centered in the *H*-band at $1.555 \mu\text{m}$. The echelle and cross-disperser grating angles were 63.04° and 36.3° , respectively. This provided nine spectral orders, 45–53, from $1.450 - 1.705 \mu\text{m}$, with spectral resolution $\sim 34,000$ with AO and $\sim 31,000$ without it. We observed the targets in series of integrations with the targets nodded, or shifted between two positions on the slit, in an ABBA pattern. The nod was $\sim 1''$ with AO, and $\sim 10''$ without AO. Nodding in this manner yielded consecutive observations with near-simultaneous measurements of the background and terrestrial emission features, and with the target spectral traces in non-overlapping positions. The background and terrestrial emission were thereby easily removed by differencing A and B exposures during the spectral extraction process. Sets of 10–20 flat and dark frames were generally observed. I combined these using pixel-by-pixel median filtering to provide master flat and dark frames for each night. Night sky OH emission lines, identified from the catalog of Rousselot et al. (2000), provided a simultaneous wavelength reference to determine the dispersion solution for all of the non-AO observations. With the AO-system, the 2-pixel wide slit was

¹<http://www2.keck.hawaii.edu/inst/nirspec/>

too small to properly expose the night sky lines; NIRSPEC's internal Ne, Ar, Xe, and Kr arc-lamps provided wavelength reference spectra for these observations, typically with four to ten strong lines per spectral order.

The NIRSPEC spectra were reduced in IDL using REDSPEC, the NIRSPEC facility software package. REDSPEC processes AB pairs of target observations by carrying out the background subtraction, flat-fielding, bad pixel removal, spatial and spectral rectification, and finally, extraction by summing over detector columns; each spectral order is processed individually. The spatial rectification removes the curvature introduced by the cross-disperser by least squares fitting the spectral traces with 2nd or 3rd order polynomials, depending on the spectral order, and resampling the spectra to lie along detector pixel rows. The spectral rectification fits the identified OH or arc-lamp lines with a Gaussian profile to measure the line centers, and uses a least-squares 3rd order polynomial fit to calculate the dispersion solution, or the translation between column pixel position and wavelength. Some NIRSPEC spectra, particularly those taken with AO, suffer from optical fringing. REDSPEC can remove most of this fringing using a Fourier domain filter with a Hanning window; this is not a perfect correction, typically some fringing remains at a level of $\sim 1\%$ or less that of the continuum.

2.2.2 CSHELL Spectroscopy

CSHELL is a high-resolution single-order echelle spectrograph operating at the 3 m NASA IRTF telescope (Greene et al., 1993). The detector is a Hughes SBRC 256×256 pixel InSb array, sensitive from 1.0 – 5.5 μm , and with a plate scale of

$0.''2 \text{ pixel}^{-1}$. Echelle orders are isolated with an order sorting circular variable filter (CVF). CSHELL operates under natural seeing at the IRTF.

M. Simon and I used CSHELL from 2003–2006 to observe the Hyades spectroscopic binaries discussed in Chapter 3. The observations were centered at $1.5548 \mu\text{m}$, with a grating angle of 62.61° . We used the $0.''5$ slit, which provided a spectral resolution of $\sim 30,000$. This is worse than the 2.5 pixel nominal resolution of $43,000$; the degradation is internal to CSHELL and has been present since 2000. We used a $\sim 10''$ nod to shift the targets on the slit in an ABBA manner, similar to the NIRSPEC observations (see 2.2.1). Sets of 12 flat and dark frames were obtained and pixel-by-pixel median filtered to create master flat and dark frames for each night. The wavelength calibration was determined by observing Ar and Kr arc-lamp spectra from CSHELL's internal lamps. The free-spectral range of the CSHELL spectra is only $\sim 40 \text{ \AA}$, and so multiple arc-lamp lines do not fall on the detector in a single configuration. By moving the CVF away from the optimal setting for the grating angle, we position lines from other spectral orders on the detector. The wavelengths of these lines, in the reference frame of the grating setting, are given by the grating equation. We used this procedure each night to observe 10 lamp lines, covering the entire spectral range of our target spectra.

I wrote the software package CSHELLEXT in the IDL programming language to reduce the CSHELL spectra. CSHELLEXT works on an AB pair of spectral images, and carries out flat-fielding, sky subtraction, and bad pixel removal similar to REDSPEC. Unlike REDSPEC, CSHELLEXT does not rely on spatial and spectral rectification, but instead uses an optimal extraction algorithm to map the spec-

tral traces in two dimensions. This is preferable to rectification because interpolating the spectra to pixel rows causes distortion and cyclical variation in the noise, and can decrease the signal-to-noise of the extracted spectrum (Piskunov & Valenti, 2002; Mukai, 1990). CSHELL does not use a cross-disperser, and the spectra do not suffer from significant spatial curvature; the spectral traces are, however, tilted relative to the detector pixel rows. CSHELLEXT builds a dispersion solution map, in both detector rows and columns, from the individual arc-lamp line observations. The target spectral traces are located by iteratively fitting, on a sub-pixel basis, Gaussian profiles tangentially to the traces, measuring the center position of these profiles at each column, and determining a least-squares solution to the centers. The dispersion solution map provides the wavelength at each column position along this fit. A weighting profile is calculated from the individual Gaussian profile widths, smoothed across the spectral dimension. The spectra are extracted by applying these weights at each column position to a sub-pixel vector tangential to the least-squares solution and summing. For most observations, this procedure yields spectra that are nearly identical to results obtained using REDSPEC. However, observations with low signal-to-noise in individual detector pixels (e.g. a faint target or poor seeing that distributes the light along the slit over many pixels) show a substantial improvement over REDSPEC in the signal-to-noise of the extracted spectra.

2.3 Spectral Type Templates

Using the cross-correlation technique to precisely measure the radial velocity of single stars or to detect a faint secondary in a binary system requires high quality template spectra that closely resemble the target spectra being analyzed. For this purpose, suites of high signal-to-noise template spectra covering a range of spectral types were observed with both NIRSPEC and CSHELL.

NIRSPEC was used in 2000 and 2001 to obtain templates from G0 to M9. I extracted these templates using REDSPEC, following the procedure described in Chapter 2.2.1. Strong terrestrial absorption features are present throughout NIRSPEC orders 45–53, and interfere with the cross-correlation technique used to analyze binary spectra. Only a subset of the observed spectral range is sufficiently free of these absorption features to be used in the analysis. Figure 2.2 shows the spectrum of the A0 star HD 13372, observed with NIRSPEC and covering the same spectral range used for all of the target and template observations. In this wavelength regime, the stellar spectrum contains only weak, broad lines of the hydrogen Brackett series; all other absorption shown in the figure is terrestrial. Order 49 and 2/3 of order 48 are nearly completely free of absorption. The remainder of order 48 and all of order 47 are contaminated by CO₂ absorption. Order 46 contains the P and Q branches of a CH₄ band. Orders 50–53 are strongly contaminated by a variety of terrestrial species. Order 45 is unusable because it falls off the detector array in one of the two telescope nod positions. As part of the ρ CrB analysis I removed terrestrial CO₂ and CH₄ absorption from orders 46, 47, and 48; Chapter 5.2 and Bender et al. (2005) describe this proce-

dure.

The template radial velocities were determined by fixing certain templates with early spectral types to published values, and using a cross-correlation analysis to bootstrap later spectral type templates to these values. The velocities originally were referenced to the measurement by Duquennoy & Mayor (1991) of HD4614 (Prato et al., 2002; Bender et al., 2005). More recently, Nidever et al. (2002) published very precise radial velocities of 844 F, G, K, and M stars, including twelve of the NIRSPEC templates, all earlier than M4. I used an iterative one dimensional cross-correlation analysis to correct the velocities of the entire template suite to the reference frame of Nidever et al. (2002). All of the revised values are consistent with those reported in Prato et al. (2002) to within 2.2 km s^{-1} , and most agree to a few tenths of a km s^{-1} (Simon et al., 2006). The estimated velocity precision for the templates is $\sim 1 \text{ km s}^{-1}$, with the earlier spectral types somewhat more precise than the later spectral types. Table 2.1 lists the NIRSPEC template suite with the revised radial velocities; Figures 2.3 through 2.6 show them in the lab velocity reference frame.

M. Simon and colleagues used CSHELL in 1997 and 1999 to observe a suite of templates ranging from G0 to M4, and covering the same spectral range of the observations described in Chapter 2.2.2 (Mazeh et al., 2002). I did not re-extract the CSHELL templates, but instead used the versions presented by Mazeh et al. (2002); they are not affected by terrestrial absorption features. These templates were taken prior to the degradation of the CSHELL resolution, and have a significantly higher spectral resolution than both the Hyades observations presented

in Chapter 3 and the NIRSPEC templates. However, they have a very small free spectral range, and hence few spectral lines. This limits the precision both of the measured template radial velocities and of the results of two-dimensional cross-correlation analyses using these templates. Because of this, target velocities measured using the CSHELL templates have similar precision to those measured with the NIRSPEC templates. I list the CSHELL templates in Table 2.2 and show them in the lab velocity reference frame in Figure 2.7.

The template suites are comprised of stars with small rotational velocities, but the Hyades binaries (Chapter 3) and the Gl569 system (Chapter 4) required template spectra covering a range of rotational broadening. I used the approach of Gray (1992), along with the non-linear limb darkening model of Claret (2000), and wrote a routine in IDL to calculate rotational broadening profiles and convolve them with the template spectra at specified rotational velocities. The limb darkening model requires values for the T_{eff} , $[M]/[M_{\odot}]$, and $\log g$ of the template stars. Where available, I obtained these values from the literature; where published values were not available, primarily for the late-type templates, I assumed solar metallicity and estimated T_{eff} and $\log g$ from Cox (2000, ch. 7) based on the stellar spectral type. For $T_{eff} \geq 3500$ K, the limb darkening model uses the ATLAS coefficients (in Milone, 1993, p. 93); for $T_{eff} < 3500$ K, the model uses the PHOENIX coefficients (Allard & Hauschildt, 1995). The PHOENIX coefficients are restricted to solar metallicity. In this manner, I generated sets of template spectra, for both NIRSPEC and CSHELL, with rotational broadening ranging from a few km s^{-1} to $\sim 100 \text{ km s}^{-1}$ or greater.

Bibliography

- Allard, F. & Hauschildt, P. H. 1995, ApJ, 445, 433
- Bender, C., Simon, M., Prato, L., Mazeh, T., & Zucker, S. 2005, AJ, 129, 402
- Claret, A. 2000, A&A, 363, 1081
- Cox, A. N. 2000, *Allen's Astrophysical Quantities* (4th ed. New York; Springer)
- Duquennoy, A. & Mayor, M. 1991, A&A, 248, 485
- Gray, D. F. 1992, *The Observation and Analysis of Stellar Photospheres* (2nd ed.; Cambridge, UK: Cambridge University Press, 1992.)
- Greene, T. P., Tokunaga, A. T., Toomey, D. W., & Carr, J. B. 1993, in Proc. SPIE, 1946, ed. A. M. Fowler, 313
- Guenther, E. W. & Wuchterl, G. 2003, A&A, 401, 677
- Latham, D. W., Stefanik, R. P., Torres, G., Davis, R. J., Mazeh, T., Carney, B. W., Laird, J. B., & Morse, J. A. 2002, AJ, 124, 1144
- Lejeune, T., Cuisinier, F., & Buser, R. 1997, A&AS, 125, 229
- Mazeh, T., Prato, L., Simon, M., Goldberg, E., Norman, D., & Zucker, S. 2002, ApJ, 564, 1007
- Mazeh, T., Simon, M., Prato, L., Markus, B., & Zucker, S. 2003, ApJ, 599, 1344
- McLean, I. S., Becklin, E. E., Bendiksen, O., Brims, G., Canfield, J., Figer, D. F., Graham, J. R., Hare, J., Lacayanga, F., Larkin, J. E., Larson, S. B., Levenson, N., Magnone, N., Teplitz, H., & Wong, W. 1998, in Proc. SPIE, 3354, ed. A. M. Fowler, 566
- McLean, I. S., Graham, J. R., Becklin, E. E., Figer, D. F., Larkin, J. E., Levenson, N. A., & Teplitz, H. I. 2000, in Proc. SPIE, 4008, ed. M. Iye & A. F. Moorwood, 1048

- Milone, E. F., ed. 1993, *Light Curve Modeling of Eclipsing Binary Stars* (Springer-Verlag; New York)
- Mukai, K. 1990, PASP, 102, 183
- Nidever, D. L., Marcy, G. W., Butler, R. P., Fischer, D. A., & Vogt, S. S. 2002, ApJS, 141, 503
- Piskunov, N. E. & Valenti, J. A. 2002, A&A, 385, 1095
- Prato, L., Simon, M., Mazeh, T., McLean, I. S., Norman, D., & Zucker, S. 2002, ApJ, 569, 863
- Rousselot, P., Lidman, C., Cuby, J.-G., Moreels, G., & Monnet, G. 2000, A&A, 354, 1134
- Simon, M., Bender, C., & Prato, L. 2006, ApJ, 644, 1183
- Wilson, O. C. 1941, ApJ, 93, 29
- Wizinowich, P. L., Acton, D. S., Lai, O., Gathright, J., Lupton, W., & Stomski, P. J. 2000, in Proc. SPIE, 4007, ed. P. L. Wizinowich, 2
- Zucker, S. & Mazeh, T. 1994, ApJ, 420, 806

Table 2.1. NIRSPEC Template Library

Star	Spectral Type	Observation Date	V_{rad} (km s^{-1})
HD196850	G0	2000 Jun 6	-21.04 ^a
HD4614.....	G0	2001 Jan 8	8.31 ^a
Gl160.....	G1	2001 Jan 8	24.03 ^a
HD1835.....	G3	2001 Jan 8	-2.40 ^a
BS5019.....	G6	2000 Jun 19	-7.85 ^a
BS7368.....	K0	2000 Jun 19	-21.51 ^a
Gl1094	K5	2001 Jan 8	-30.71
BS8086.....	K7	2000 Jun 11	-64.02 ^a
Gl34B	K7	2001 Jan 8	-11.29 ^a
Gl763.....	M0	2000 Jun 19	-59.20
Gl15A	M1.5	2000 Jun 10	11.81 ^a
Gl436.....	M2.5	2001 Jan 5	9.61 ^a
Gl752A.....	M3	2000 Jun 9	35.88 ^a
Gl213.....	M4	2000 Jan 8	105.96
Gl402.....	M4	2001 Jan 5	-1.04 ^a
Gl669B.....	M4.5	2000 Jun 10	-34.90
Gl406.....	M5.5	2001 Jan 5	18.61
LHS292 ^b	M6.5	2001 Jan 5	1.35
Gl644C.....	M7	2001 Feb 2	15.21
LHS2351	M7	2001 Feb 2	0.72
LHS2065 ^c	M9	2001 Feb 2	7.02

^aNidever et al. (2002)

^bReported to be a spectroscopic binary (Guenther & Wuchterl, 2003)

^cX-ray flare star (Guenther & Wuchterl, 2003)

Table 2.2. CSHELL Template Library

Star	Spectral Type	Observation Date	V_{rad} (km s^{-1})
Gl475.....	G0	1997 Dec 23	8.0
HR5072	G4	1999 May 02	1.3 ^a
HR3259	K0	1997 Dec 23	29.7
Gl483.....	K3	1999 Feb 19	9.0
BS8085	K5	1997 Dec 22	-64.0
BS8086	K7	1997 Dec 22	-64.0
Gl382.....	M1.5	1997 Dec 23	12.0
Gl447.....	M4	1999 Feb 18	-31.1

^aCorrected from the 3.2 km s^{-1} value reported by Mazeh et al. (2002)

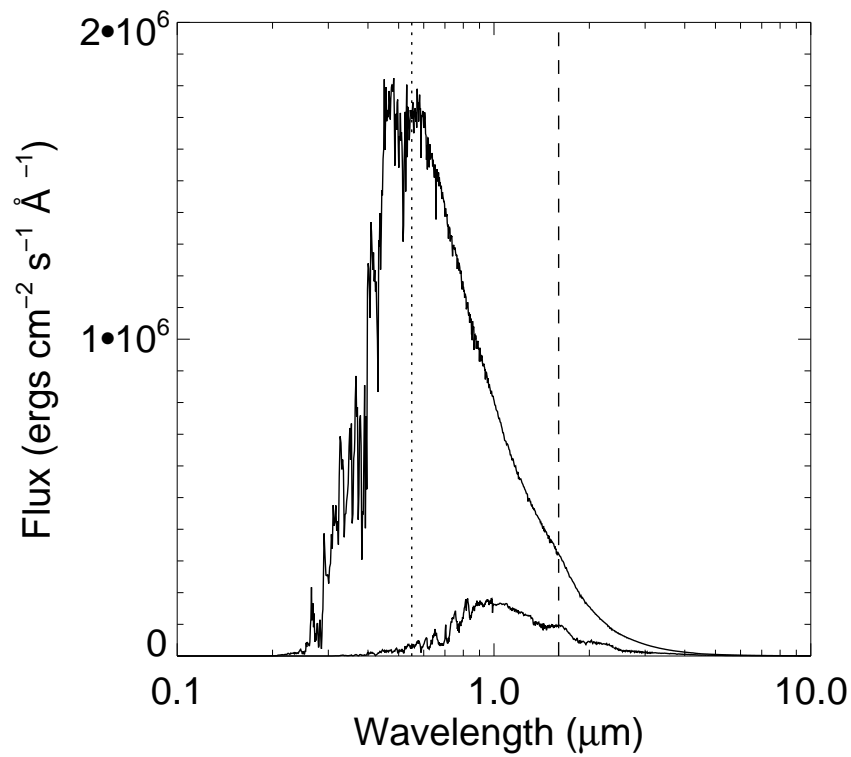


Figure 2.1 Synthetic spectra from the library of Lejeune et al. (1997) for stars of $1 M_{\odot}$ and $0.2 M_{\odot}$, with solar metallicity and an age of 1 Gyr. The flux ratio of a binary with such components is ~ 10 times larger in the H -band (*dashed line*) than in the V -band (*dotted line*).

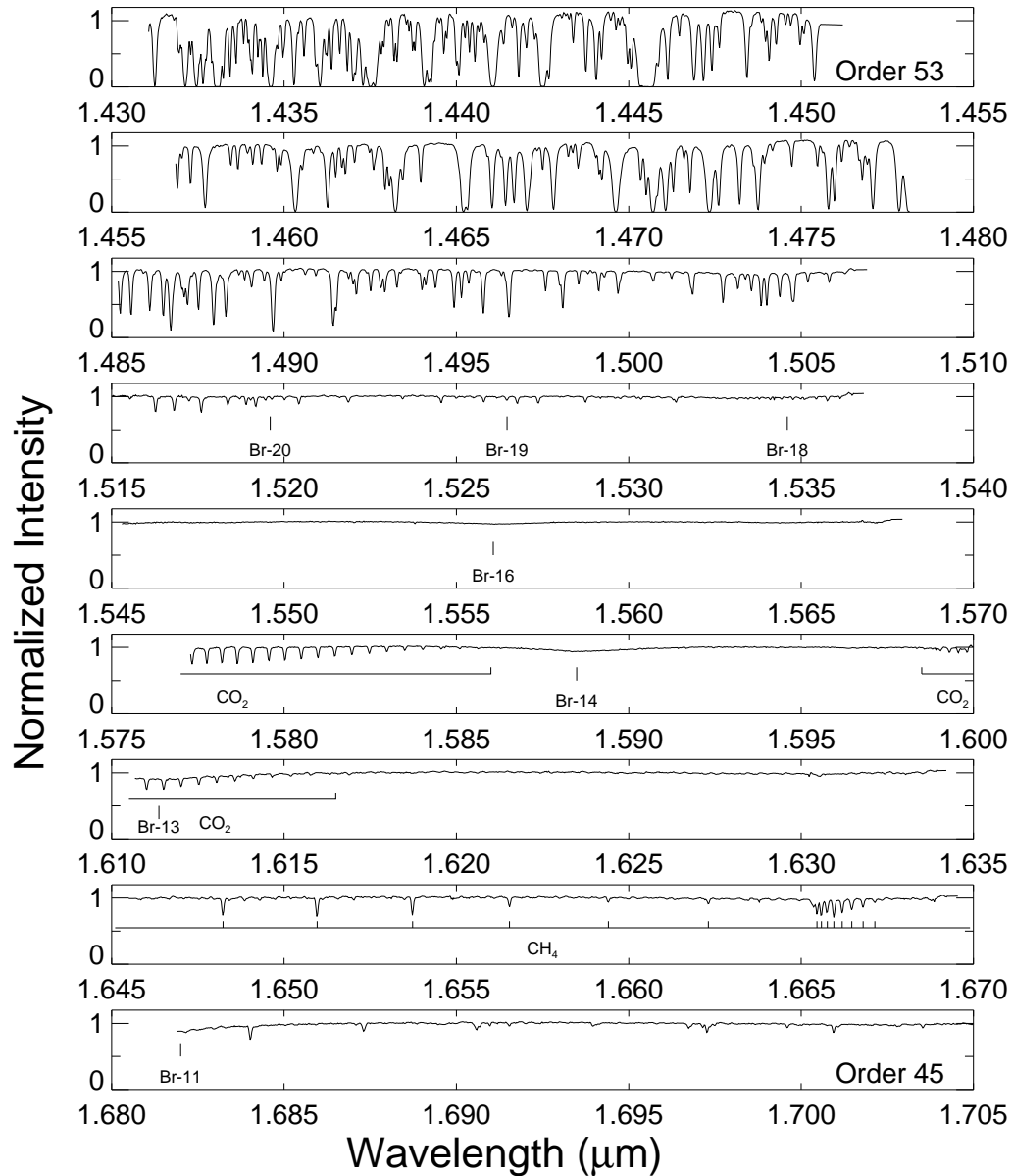


Figure 2.2 NIRSPEC spectrum of the A0 star HD133772 for orders 45–53. The spectra have been flattened and normalized to their continuum levels. The stellar spectra are nearly featureless except for the very broad hydrogen Brackett lines indicated. The remaining absorption lines are terrestrial. The location of a CH_4 band in order 46 and CO_2 bands in orders 47 and 48 are indicated.

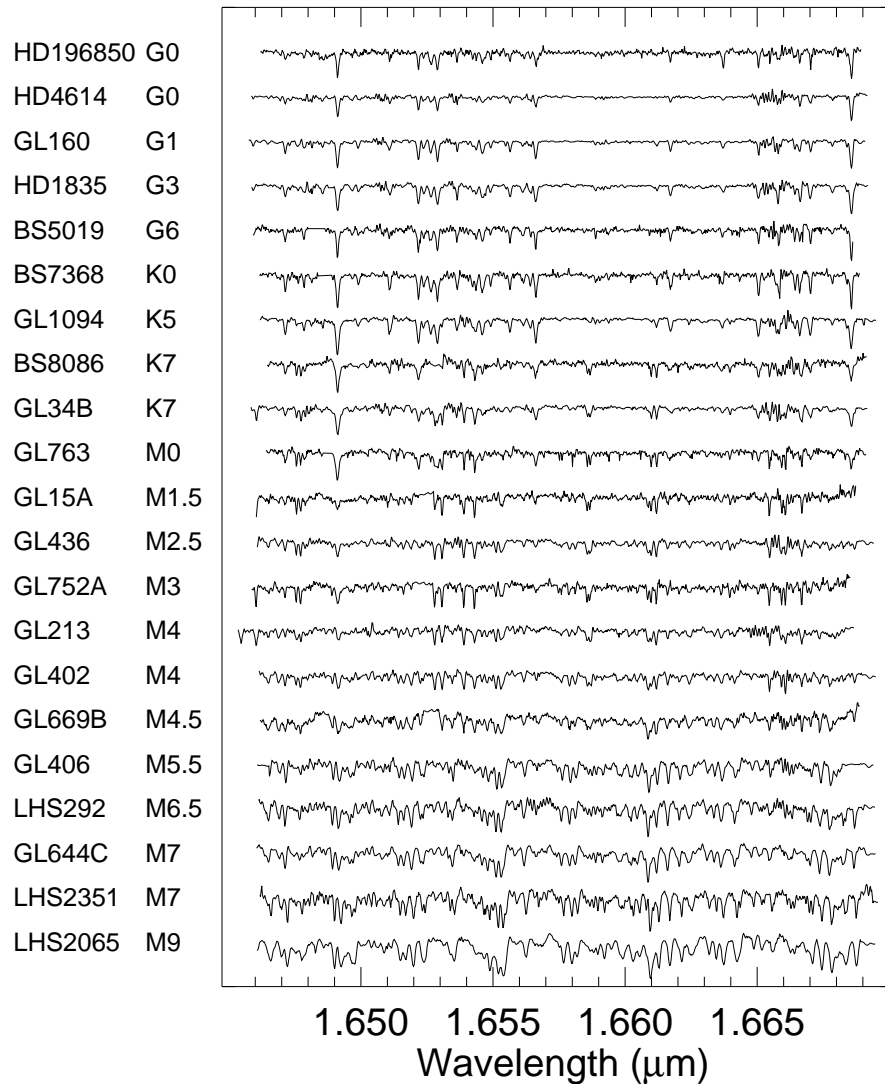


Figure 2.3 NIRSPEC order 46 templates in the lab reference frame. The spectra have been flattened, normalized to their continuum levels, and terrestrial absorption removed.

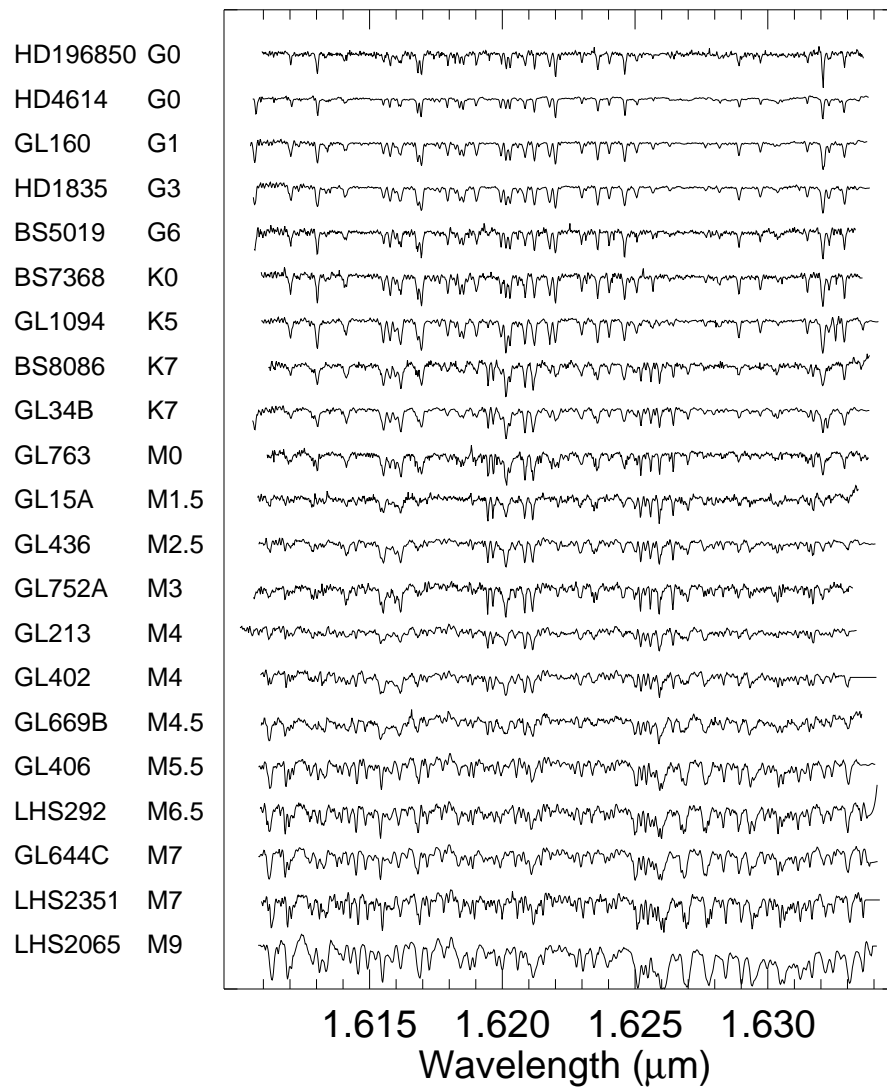


Figure 2.4 Same as Figure 2.3, but for NIRSPEC order 47.

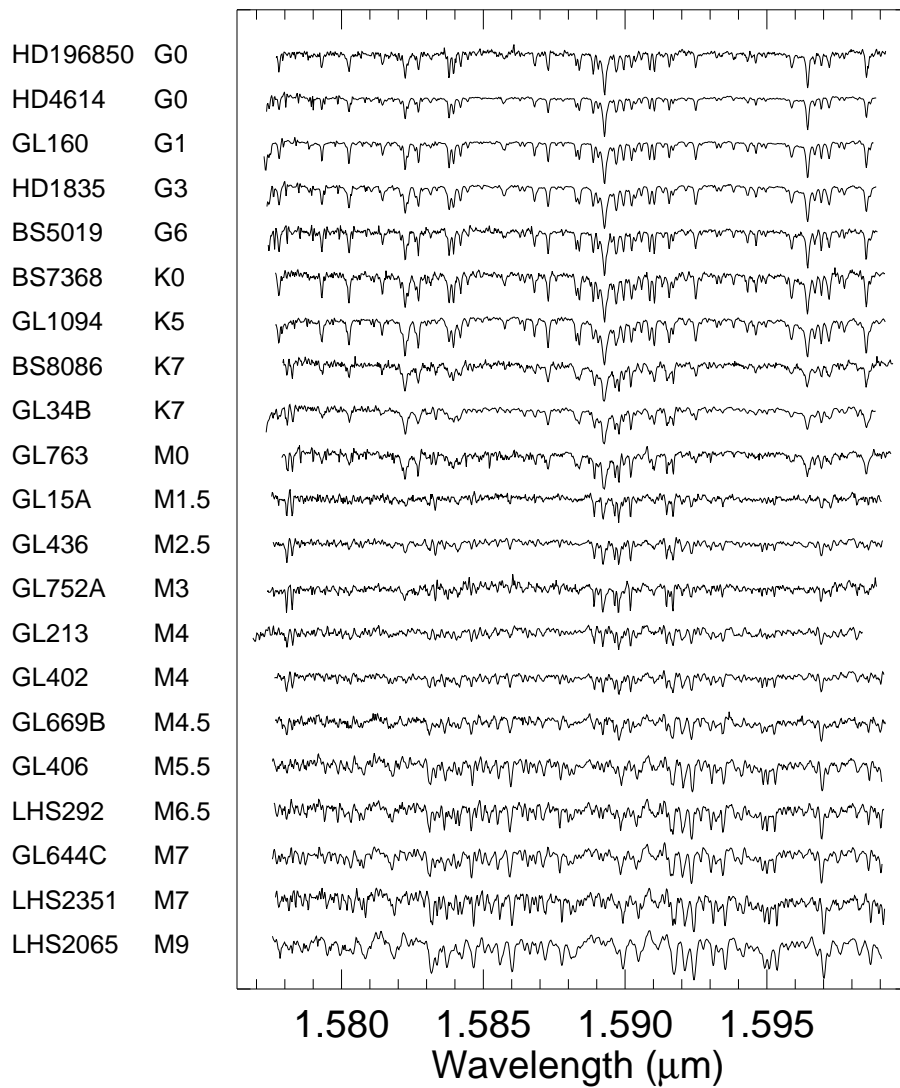


Figure 2.5 Same as Figure 2.3, but for NIRSPEC order 48.

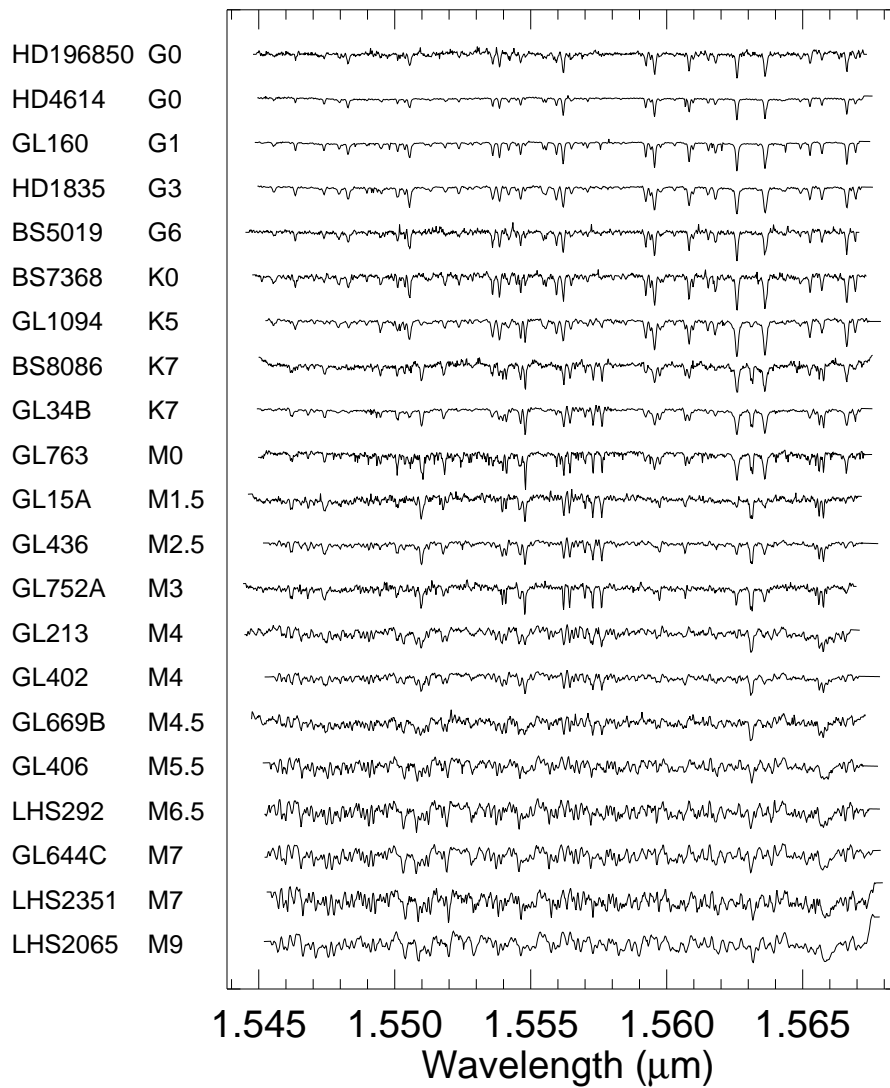


Figure 2.6 Same as Figure 2.3, but for NIRSPEC order 49.

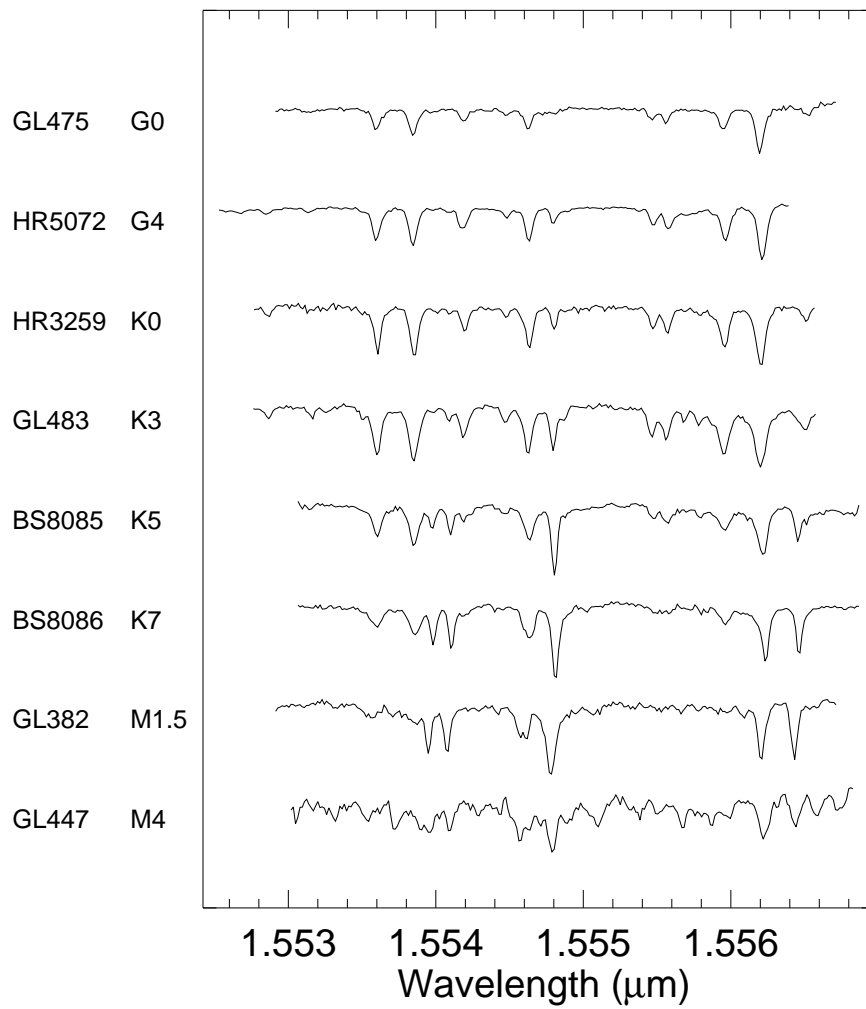


Figure 2.7 CSHELL templates in the lab reference frame. The spectra have been flattened and normalized to their continuum levels.

Chapter 3

Dynamical Mass Ratio Distribution of Spectroscopic Binaries in the Hyades Cluster

3.1 Introduction

The distribution of mass ratios in binary stars provides a diagnostic of the processes involved in their formation. (Bonnell et al., 2003; Tohline, 2002; Clarke, 2001). In simulations of isolated binary star formation from collapsing molecular cloud cores, Bate & Bonnell (1997) found that the mass ratio of the resulting binary depends on the angular momentum of material accreting from outside the collapsing core. If the infalling material has a small angular momentum then most accretes onto the primary, resulting in a binary with a small mass ratio. If the angular momentum of the accreting material is large, then a greater proportion of material accretes onto the secondary than onto the primary, and the mass ratio is closer to one. Infalling material has less angular momentum per unit mass in systems with large separations and long orbital periods, than in systems

with small separations and short orbital periods. This implies, therefore, that binaries with long periods should preferentially have small mass ratios, while binaries with short periods should have mass ratios close to one. Duquennoy & Mayor (1991) observed a large sample of nearby F- and G-type stars, and found that the mass ratio distribution for medium to long period binaries increases towards small mass ratios. More recently, Mazeh et al. (2003) measured the distribution of mass ratios for a well defined sample of low mass spectroscopic binaries from the Carney-Latham sample of nearby G- and K-dwarfs (Carney et al., 1994). They found a flat distribution over the range of $q \sim 0.3 - 1.0$. These samples, however, represent the average result of star formation in the solar neighborhood $\sim 5 - 10$ Gyr ago.

Because most star formation occurs in localized star forming regions and results in clusters (Clarke et al., 2000; Horton et al., 2001), studying the isolated formation of binaries does not provide a complete picture of the processes at work. Bate et al. (2002) simulated the collapse of an entire molecular cloud into a cluster and found that fragmentation is not necessary to produce binaries with separations less than about 10 AU. Instead, these close systems can form through the dynamical interactions of single stars and unstable multiple systems, preferentially creating binaries with large mass ratios. This has the additional result that the binary frequency is larger for more massive stars. Many of the close binaries formed in their simulation are members of hierarchical triple systems and have a wide companion. Observations of binaries in open clusters are necessary to test these results and probe localized star formation. Such observations have

additional advantages over observing binaries in the field. Namely, the cluster members formed together and so have similar age and metallicity. Very young stars in active star forming regions are difficult to measure spectroscopically because they tend to have high rotation velocities. Stars in older open clusters, however, still retain their cluster identity yet are rotationally spun down.

The Hyades is one such well studied, nearby open cluster: it presents an excellent laboratory for examining binary star formation. The cluster has an age of ~ 650 Myr (Lebreton et al., 2001), old enough that stars later than spectral type F3 have slowed to $v \sin i \leq 25 \text{ km s}^{-1}$ (Kraft, 1965), and G-type and later to $v \sin i \leq 10 \text{ km s}^{-1}$ (Stauffer et al., 1987). Most mid K-type and earlier cluster members have individual *Hipparcos* distances, and with a mean cluster distance of ~ 46 pc (Perryman et al., 1998) the known binaries are bright. Additionally, with metallicity $[\text{Fe}/\text{H}]=0.14$ (Lebreton et al., 2001) the spectral lines of Hyades members are deep and well suited to spectroscopic analysis. Finally, Patience et al. (1998) carried out a study of the Hyades “visual binaries” using speckle interferometry and determined that the mass ratio distribution for these wide systems increases towards smaller q . Beginning in 2003, I undertook a study using infrared spectroscopy to measure the dynamical mass ratio distribution for SBs in the Hyades. In this chapter I present the results of that study.

3.2 The Hyades Binary Sample

Accurately measuring the mass ratio of an SB with infrared spectroscopy is simplified if the single-lined binary (SB1) solution is already determined and is

well constrained (see Chapter 2). Therefore, to determine the Hyades binary mass ratio distribution I needed a large, complete sample of well studied SB1s that are confirmed cluster members. The Hyades nearby distance and old age means that its members are dispersed over a wide area of the sky, making membership determination difficult. Historically, many authors have evaluated candidate cluster members by measuring their proper motion, radial velocity, and position on a color-magnitude diagram (e.g. van Bueren, 1952; van Altena, 1969; Hanson, 1975; Griffin et al., 1988; Reid, 1992); these surveys contain numerous stars that are non-members or have uncertain membership status. More recently, Perryman et al. (1998) and de Bruijne et al. (2001) used *Hipparcos* parallax and proper motion results to further refine the membership.

D. Latham and colleagues have monitored candidate Hyades members with visible light spectroscopy for over two decades. They have observed many binaries and determined SB1, and in some cases SB2, solutions. They have also independently assessed the cluster membership of their SB1s by incorporating their measurements with previously published criteria. In 2004 they kindly provided me with their unpublished SB1 parameters, P , e , T_0 , ω , K_1 , γ , and the mass function, $f(M)$. From their sample, I selected 32 Hyades binaries that are confirmed cluster members and have measured SB1 parameters. I restricted my sample to binaries with primary spectral types of early F through early M, and with H magnitude brighter than ~ 9 . I included binaries with long periods if the SB1 solutions predicted a large primary and secondary velocity separation during the time of my observations. I excluded long period systems, typically

with $P \gtrsim 5000$ days, if the predicted velocity separation was only a few km s^{-1} or less. Table 3.1 lists the sample. Columns 1 and 2 list the name and HD number of the primary star. Columns 3 and 4 give the coordinates. Column 5 contains the primary spectral type, as listed in the Simbad database and confirmed with the cross-correlation analysis discussed in Chapter 3.4. Columns 6 and 7 give V magnitude (*Hipparcos* where available and Simbad otherwise) and H magnitude (2MASS), respectively. Column 8 lists the orbital period from the SB1 solution. Column 9 lists the minimum mass ratio, determined from the SB1 mass function and an estimate of the primary mass. The primary mass was initially estimated from the spectral type. Later, I revised the primary masses for systems with a *Hipparcos* distance and for which I measured q (see 3.4.4) using the mass-luminosity relationships of Baraffe et al. (1998); these systems are indicated. Figure 3.1 shows the distribution of H -magnitude, from 2MASS, for the sample in Table 3.1.

3.3 Observations and Data Reduction

The Hyades binaries in Table 3.1 were observed from October 2003 – February 2006, using the CSHELL spectrometer on the IRTF telescope. Chapter 2.2.2 provides details of the observing procedures; Table 3.2 provides a log of the observations. The October 2003 observations suffered from poor weather conditions and did not result in any usable target spectra. Instead, during this time I obtained very high signal-to-noise lamp calibrations, which were later used to precisely measure the CSHELL spectral profile across the detector and which aided the

fitting of lamp calibrations taken during the observations in 2004 – 2006.

I extracted the spectra with my IDL routine CSHELLEXT (see 2.2.2). I calculated the dispersion solution for each night's observations from observed lamp lines and applied it to the target spectra. During the Fall 2005 and Spring 2006 observations, the CSHELL detector experienced brief, uncontrolled warmups. A typical warmup event lasted for less than a minute, after which time the detector temperature quickly returned to the nominal value. This occurred several times per hour over the course of a night and affected $\sim 20\%$ of the observations. Integrations in progress when a warmup event occurred suffered from an increase in the background from a normal level of a few tens of ADUs to $\sim 10^3$ ADU. This increased the noise level of the observations and made AB nod subtraction difficult. I adapted the extraction procedure to remove a constant background, equal to the median background value, from the affected observations, which allowed them to be extracted in the usual manner. However, the resulting spectra have a much lower signal-to-noise level than those obtained without any warmup events.

On 2005 February 22, L. Prato kindly observed three of the Hyades binaries, H69, vB 43, and vB 142, with the NIRSPEC spectrometer on the Keck II telescope, without the AO system. H69 and vB 43 are both faint, and difficult to observe with CSHELL; vB 142 has a very low mass companion, and a NIRSPEC observation was necessary to confirm an earlier CSHELL detection. Details of the observing procedures are provided in Chapter 2.2.1. The observations are included in Table 3.2; NIRSPEC and CSHELL observations are differentiated in the instru-

ment column with an N or C, respectively. The NIRSPEC spectra were extracted using the REDSPEC software, and the dispersion solution was calculated from night sky OH lines (see Chapter 2.2.1). Only the order 49 spectra were used in the cross-correlation analysis described in Chapter 3.4.

3.4 Results

Most of the Hyades binaries in my sample have primary stars with a small projected rotational velocity, $v_{\text{rot}} \sin i$; vB 8, vB 30, vB 68, vB 77, and BD+02 1102 have rapidly rotating F-type primaries with spectral lines broadened by as much as 100 km s^{-1} . Chapter 3.4.1 describes the analysis to measure the component radial velocities of the slow rotators. Those with rapidly rotating primary stars required a modified analysis and are discussed in Chapter 3.4.2.

3.4.1 Velocity Measurements: Slow Rotators

Each of the binaries with a slowly rotating primary was analyzed in the following manner. I used the Latham SB1 parameters to calculate the orbital phase and predict the radial velocity of the primary component for each observation. I confirmed these velocities by carrying out a one-dimensional cross-correlation between the target and the NIRSPEC order 49 template suite (see 2.6), using the cross-correlation routine SBCCORR (see 2.1). The template providing the greatest correlation indicated the spectral type and rotational velocity of the primary. Figure 3.2 shows the distribution of the difference between the predicted velocities and the measured velocities. The mean of the distribution is $\sim 0.3 \text{ km s}^{-1}$

and a Gaussian fit to it has a width of $\sim 0.9 \text{ km s}^{-1}$, demonstrating that the two velocity reference frames are in good agreement.

I then used SBCCORR to carry out a two-dimensional cross-correlation analysis to solve for the velocity of the secondary component and the secondary-to-primary flux ratio. I only used the best two or three NIRSPEC primary templates, determined from the one-dimensional analysis, and the CSHELL templates of corresponding spectral type and rotational velocity. The q_{min} , estimated from the SB1 mass function and mass of the primary (see 3.2), constrained the range of both the velocity and spectral type of the secondary. I chose $\sim 6 - 10$ possible secondary templates, and restricted the secondary velocity search range accordingly. The flux ratio was typically left unconstrained. I compared the correlation surfaces that SBCCORR returned for each pair of templates to measure the velocity of the secondary and the flux ratio. To obtain the final secondary velocity, I averaged the measured values from multiple template pairs. This procedure successfully identified the secondary component in 23 of the observed binaries; the measured velocities are listed in Table 3.2.

The uncertainty of a measured velocity has two components: the velocity uncertainty of the templates, and the uncertainty in measuring the center of the correlation peak due to noise in the target spectrum. I estimated the contribution from the templates as equal to the variance of the measured velocities from different pairs of templates. To determine the contribution from the target spectrum noise, I created a model binary spectrum from a pair of templates used in the SBCCORR analysis of the target spectrum, and with the same velocity separa-

ration and flux ratio as measured in the target spectrum. I added random noise to the model binary and analyzed it with SBCCORR using the same pair of templates. I optimized the amplitude of the noise such that the peak correlation from the analysis of the model spectrum equaled the peak correlation from the analysis of the target spectrum. I then generated 100 copies of the model binary and added noise at the determined amplitude to each. I measured the set of model binaries with SBCCORR to obtain a distribution of V_1 and of V_2 . I fit each distribution with Gaussian, and took the widths to be the uncertainty contributed by noise. For each target spectrum, I repeated this analysis on 4–6 template pairs. I considered the average of the measured uncertainties to be the uncertainty contribution from noise in the target spectrum. I combined this in quadrature with the uncertainty from the templates to determine the uncertainty on the measured secondary velocity, listed in Table 3.2

The flux ratio measured for the three target spectra obtained with NIRSPEC was insensitive to the particular template pair used for the analysis. With the CSHELL spectra, the flux ratio varied by a factor of two or more, depending on the template pair. The CSHELL spectra cover $\sim 1/6$ of the spectral range of NIRSPEC order 49, and thus have many fewer spectral lines than the NIRSPEC spectra with which to measure the flux ratio. I averaged the flux ratios measured with multiple template pairs to determine the flux ratio for each observed spectrum. I then estimated the corresponding uncertainty by following the same procedure used to estimate uncertainties on the velocity measurements.

3.4.2 Velocity Measurements: Rapid Rotators

The target binaries vB 8, vB 30, vB 68, vB 77, and BD+02 1102 have F-type primary stars that are rapidly rotating. The spectral lines of these stars are strongly rotationally broadened, and so measuring the primary velocities is difficult; I was only able to measure the primary velocity for vB 8 and vB 77, and in those cases the uncertainties are large. I suspected, however, that companions of a later spectral type might have much smaller rotational velocities. To solve these systems as SB2s, I considered the primary contribution to be featureless. I used q_{\min} to predict the radial velocity and spectral type of the secondary, as described for the slowly rotating systems. I then carried out a one-dimensional SBCCORR analysis to search for the secondary, using a range of plausible secondary templates, and did not attempt to measure the flux ratio. The technique was successful on all of the systems except for vB 30, and demonstrates that the cross-correlation is a powerful tool for making a low signal-to-noise detections.

3.4.3 Non-detections

I expected that the mass ratio, and hence flux ratio, of a binary would be the dominant factor over whether or not I detected the secondary: higher contrast systems should be more difficult than lower contrast ones. Figure 3.3 shows the distribution of q_{\min} for the 27 binaries detected as SB2s and also for the five systems where the companion was not detected. The q_{\min} for binaries not detected as SB2s is not concentrated at small q_{\min} , as would be expected if the mass ratio dominated the likelihood of detection. Instead, the distributions of detections

and non-detections are qualitatively similar and alternative explanations for the non-detections must be sought. Two of the non-detections, vB 30 and vB 114, are straight forward to understand. vB 30 is a rapid rotator which I observed twice. The binary has a small q_{\min} , 0.19, and the primary star is a bright F0-type star. The flux ratio may be very small, or the companion may also be a rapid rotator. I observed vB 114 on only one occasion, when the predicted velocity separation was less than 3 km s^{-1} . The period is ~ 5083 days; observations in 6–7 years when the velocity separation is larger should detect the secondary. A variety of factors combined to result in the other three non-detections. vB 39 has a long period, and the predicted velocity separation during both of my observations is very small; new observations, obtained in a few years when the velocity separation is larger, have a better chance of detecting the companion. H411 and L90 are both faint targets for CSHELL, and my observations of these binaries have a low signal-to-noise; new CSHELL, or better yet NIRSPEC, observations with a greater signal-to-noise are likely to detect the companions in both systems.

3.4.4 Double Lined Spectroscopic Binary Solutions

I observed no binary in my sample on more than four occasions, and most only once or twice, so my measurements of V_1 did not significantly improve upon Latham’s SB1 parameters. To derive the SB2 orbits, I fixed the parameters P , e , T_0 , ω , K_1 , and γ to their SB1 values. I then carried out a χ^2 minimization on my V_2 measurements to solve for K_2 . I used K_2 to calculate the mass ratio for each system, $q = K_1/K_2$. Table 3.3 lists the number of times each binary was observed,

the number of observations where the secondary was detected, the derived K_2 , and the calculated value of q . I also list the weighted mean of the α 's derived from each observation. Figures 3.4 – 3.6 show the SB2 solutions for each of the 27 binaries that I solved. Latham's SB1 solutions are included without modification. I also plot my measured values of V_1 to demonstrate agreement with Latham; I was unable to measure the rapidly rotating primary components of vB 68 and BD+02 1102, so V_1 is not plotted for those systems.

Five of the SB2s depend on a single measurement of the secondary velocity, and another ten on only two measurements. Consequently, many of the measured K_2 's, and the resulting q 's, have large uncertainties. Figure 3.7 plots q_{\min} against the measured q 's to demonstrate that the measured values are plausible. As expected, q is greater than or within 1σ of q_{\min} for all of the binaries, except vB 8 and L77. The rapidly rotating primary in vB 8 may have interfered with my measurement of the secondary, and I only observed L77 on one occasion. The measured values of K_2 and q in both of these systems should be viewed cautiously until additional observations can clarify the situation.

Figure 3.8 plots the measured flux ratio's against the measured q 's, along with theoretical H -band flux ratios from Baraffe et al. (1998) for a range of primary masses. The measured values have a large scatter around the theoretical curves that is attributable to the difficulty of measuring accurate flux ratios with the limited spectral range of CSHELL. Additionally, the model values represent the integrated flux over the entire H -band, of which the CSHELL spectra sample only $\sim 1.5\%$. Three of the binaries, vB 8, vB 142, and L79, do not agree with the theo-

retical curves. Measuring α in vB 8 is difficult because of the nearly featureless, rapidly rotating primary; as previously stated, q for this system is also suspect. L79 was observed only once, with a low signal-to-noise, and at a poor phase. Both q and α have large uncertainties for this system. The q measured for vB 142 is very small, and accurately measuring α at this level is difficult.

3.5 Mass Ratio Distribution

Figure 3.9 shows the distribution of mass ratios for all of the SB2s that I measured in the infrared (Table 3.3), combined with the SB2s that Latham and colleagues have measured in the visible. The distribution is qualitatively inconsistent with the flat distribution that Mazeh et al. (2003) measured for SB2s in the field. Statistical tests can quantify this inconsistency, however they suffer because of the small number of SB2s in my sample. A Kolmogorov-Smirnov (K-S) test gives only a 0.054 probability that the combined distribution of q 's is consistent with a flat distribution; a χ^2 test gives a probability of 0.20 that the distribution, as binned in Figure 3.9, is flat. The two tests return probabilities that differ by a factor of four, but generally confirm that the distribution is not flat. Considering the distribution of q_{\min} for the sample binaries that were not detected (Figure 3.3), I do not believe that my mass ratio distribution is missing a large number of systems with small q . My binary sample itself may be incomplete at small q because the underlying SB1 sample is incomplete. Systems with long periods or small secondary masses are difficult to detect as SB1s because the primary velocity amplitude is small at all orbital phases; systems with large

eccentricity can be detected if they are observed during the brief period when the primary velocity is large. Additionally, the SB1 survey includes few binaries with M spectral type primaries, so the distribution of q for systems with $M_1 \lesssim 0.5 M_\odot$ is relatively unsampled.

The magnitude of the mass ratio uncertainties reported in Table 3.3 varies widely depending on the number and quality of the secondary velocity measurements for each binary. I incorporated these uncertainties in the mass ratio distribution in the following manner. For each binary, I distributed the measured mass ratio as a Gaussian, centered at the measured value and with width equal to the measurement uncertainty. I clipped each Gaussian at $q = q_{min} - 2 \times \sigma_{q_{min}}$, where $\sigma_{q_{min}}$ is the estimated uncertainty on the minimum mass ratio, and at $q = 1$, and renormalized appropriately. Figure 3.10 shows the resulting mass ratio distribution, binned identically to Figure 3.9. Smoothing the measured q 's in this manner has little effect on the distribution of SB2s measured in the visible because these systems are generally well determined. The contribution from infrared SB2s with $q \gtrsim 0.2$ is also unaffected, although many of the q 's in this regime are poorly determined. The most significant change occurs for $q \lesssim 0.2$ where my measurements of q are not secure.

3.6 Discussion

3.6.1 Component Masses

My initial estimates of the primary masses of the sample binaries were based on their reported spectral types. Most of the binaries in the sample have known *Hipparcos* distances, and so photometry of the blended light from the binary can be directly compared with theoretical mass-luminosity relationships. I combined the models of Baraffe et al. (1998), *JHK* photometry from 2MASS, and my measured mass ratios, to improve my estimates of the primary masses. I believe the uncertainties on the new estimates are $\sim \pm 0.1 M_{\odot}$. Table 3.4 lists the estimated primary masses for all of the binaries where I detect the secondary; I indicate those with improved primary mass estimates. Figure 3.11 shows the distribution of primary masses for the SB2s in my sample and in Latham's sample. Both distributions are centered roughly at $1.0 M_{\odot}$; the primary masses of my infrared SB2s are more concentrated among G- and K-stars than those for the visible light SB2s.

I used the estimated primary masses and the measured q 's to calculate the secondary masses; these values are reported in Table 3.4. Figure 3.12 shows the distributions of secondary masses, similar to Figure 3.11. The distribution of secondary masses for SB2s measured in visible light is very similar to the corresponding distribution of primary masses. Conversely, the distribution of secondary masses for my sample of infrared SB2s is strongly shifted from the primary mass distribution towards lower masses: all but one of my estimated sec-

ondary masses is less than $0.8 M_{\odot}$. This is the expected result, and clearly demonstrates the usefulness of infrared spectroscopy for detecting faint companions. Figure 3.13 shows the initial mass function (IMF) measured for the Hyades SB2 secondaries. For comparison, the IMF measured by Hillenbrand (1997) for the Orion Nebula Cluster (ONC), age ~ 1 Myr, is also shown. There may be a real deficit of low mass companions in the Hyades when compared with the ONC single stars; this is consistent with the results of Bate et al. (2002) that close binaries preferentially form with large mass ratios (see 3.1). A perceived deficit of massive Hyades members compared with the ONC comes from not including the Hyades SB2 primaries, which are potentially biased from the SB1 sample selection, and because at the current age of Hyades the most massive stars no longer exist.

Three of my SB2s have companion masses near that of a brown dwarf: vB 8, L79, and vB 142. The SB2 solution for vB 8 is suspect (see 3.4.4). L79 depends on only a single measurement of the companion, so the uncertainty on q is large. I measured vB 142 on four occasions and the companion does have a very small mass, $0.06 \pm 0.04 M_{\odot}$. The uncertainty is, however, large and additional observations are necessary to positively confirm the companion as a brown dwarf.

3.6.2 Angular Momentum of Spectroscopic Binaries

The process of star formation within a rotating molecular cloud is poorly understood. Conceptually, stars form within turbulent cores distributed throughout the cloud. Typical cores have an angular momentum per unit mass (J/M), or specific angular momentum, of $\sim 10^{21} \text{ cm}^2 \text{ s}^{-1}$ (Bodenheimer, 1995). If a core

collapses into a single star, and angular momentum is conserved, then the newly formed star will rotate at a significant fraction of the speed of light (Spitzer, 1998, ch. 13), much faster than is observed in young stars. A typical Hyades A-type star with $v_{\text{rot}} \sim 100 \text{ km s}^{-1}$ has $J/M \sim 10^{17} \text{ cm}^2 \text{ s}^{-1}$; this is insufficient to account for the J/M from a turbulent core. Binary stars have a much larger J/M than single stars. Fisher (2004) modeled the formation of isolated binary stars from a turbulent molecular cloud core by assuming that the angular momentum contained in the binary stars was directly related to the angular momentum contained in the core. They found that a significant loss of angular momentum is necessary to obtain the observed properties of binary stars.

I estimated the distribution of specific angular momentum for my sample of SB2s. Adapted from Fisher (2004), equation A2,

$$J/M = \sqrt{a_1 \frac{1+q}{q}} \sqrt{1-e^2} \sqrt{\frac{G(M_1 M_2)^2}{(M_1 + M_2)^3}}, \quad (3.1)$$

where $M = M_1 + M_2$. Following Heintz (1978), a_1 is given by,

$$a_1 = \frac{13751}{\sin i} K_1 P \sqrt{1-e^2}, \quad (3.2)$$

with K_1 in km s^{-1} and P in days giving a_1 in km. I estimated $\sin i$ from the mass function as,

$$\sin^3 i = \frac{f(M)}{M_1} \frac{(1+q)^2}{q^3}. \quad (3.3)$$

Figure 3.14 shows my derived distribution of J/M for the visible and infrared SB2 binaries. The two distributions cover a similar range of J/M , $\sim 10^{19} \text{ cm}^2 \text{ s}^{-1}$, much

less than a typical molecular cloud core.

3.6.3 Comparison with Wide Binary Population

The mass ratio distribution presented in Chapter 3.5 includes binaries with semi-major axis as large as ~ 3 AU. Measuring SBs with larger separations requires long term observations. Furthermore, the component velocities in wide binaries are small and so very precise velocity measurements would be necessary to detect the systems as SB2s. Patience et al. (1998) used speckle imaging at $2.2 \mu\text{m}$ to detect 33 Hyades binaries with semi-major axis from ~ 2.5 AU – 50 AU. They measured the K -band magnitude difference between the primary and secondary components of each binary, and used an empirical mass – M_K relation to estimate the mass ratio and component masses. Three of their speckle binaries are included in my SB sample, vB 96, L33, and vB 113. The mass ratios that they estimate, 0.78, 0.95, and 0.37, respectively, are consistent with my measured values, except for L33 which is more than 2σ different. The Patience survey also detects the wide binary component of eight hierarchical triple systems. Latham has solved the inner binary for four of these systems, L83, vB 185, vB 124, and BD+22 669; I have added the remaining four, L20, vB 102, vB 151, and vB 40, with my infrared survey.

The Patience et al. (1998) survey was complete for binaries with separations of $\sim 5 - 50$ AU, and $q \gtrsim 0.3$. They derive a mass ratio distribution for the 22 binaries in this regime that is strongly increasing towards lower q . This result, however, depends almost entirely on a paucity of systems with $q \gtrsim 0.8$. Figure 3.15

shows a mass ratio distribution for the combined sample of SB2s and speckle binaries. vB 113 belongs to both the infrared SB2 sample and the speckle sample; I include it with the SB2s in Figure 3.15. Excluding the binaries with $q < 0.3$, where the speckle sample is incomplete, the combined distribution is consistent with a flat distribution with a probability of 87% using a χ^2 test and 74% using a K-S test.

I calculated J/M for the speckle binaries to examine whether they represent a different population from the SB2s. I assumed that the orbits are circular and have a random distribution of inclinations, and restricted the sample to binaries with separations from 5–50 AU. Figure 3.16 shows the resulting distribution. As expected for binaries with wider separation, the typical J/M for the speckle binaries is larger than for the SB2s in Figure 3.14. Figure 3.17 shows a composite distribution of J/M for the SB2s and the speckle binaries. I separated out the eight triples that have measurements for both the inner and outer binaries, and determined the total J/M for these systems. The triples are grouped on the right side of the J/M distribution, demonstrating that complicated multiple systems can contain a large J . The composite distribution shows that while J/M for the speckle binaries is generally larger than for the SB2s, the two samples do overlap. I also indicate the J/M for Jupiter to suggest where potential planets might lie on the diagram.

3.7 Summary and Suggestions for Future Work

I successfully detect the faint secondaries in Hyades SBs with mass ratios as low as ~ 0.1 and demonstrate that combining infrared spectroscopy with a cross-correlation analysis can turn many visible light SB1s into SB2s. I measure a mass ratio distribution for Hyades SB2s, detected in the infrared and the visible, that decreases towards small q . The distribution of minimum mass ratios for binaries where I do not detect the secondary is not concentrated at small values of q . Therefore, my measured distribution is not missing a large number of binaries with small q . The SB1 survey that formed my sample may be missing binaries with small q because they are difficult to detect as SB1s. That survey is also incomplete for systems with primary masses later than mid to late K spectral type because those targets are faint. As expected, the specific angular momentum derived for the speckle binary sample is larger than that for the SB2 sample because the separation of the components in the speckle binaries is larger. However, the two populations are not distinct in J/M , but instead overlap.

The mass ratio distribution that I measure for short period binaries is quantitatively different from the distributions derived by Duquennoy & Mayor (1991) and Patience et al. (1998) for medium to long period binaries. Their distributions increase towards small mass ratios, while mine increases towards large mass ratios. This is generally consistent with the predictions of Bate & Bonnell (1997) based on the specific angular momentum of material accreting onto the binary from outside the molecular cloud core (see 3.1). My distribution is also different from the flat distribution that Mazeh et al. (2002) measured for short period

binaries in the solar neighborhood. The numerical simulation of cluster formation carried out by Bate et al. (2002) formed a very small cluster: only 50 stars, including seven short period binaries. This is too small of a sample to derive an expected mass ratio distribution for for these binaries. Future simulations producing larger clusters are needed to provide detailed numerical investigations of these distributions.

Many of the binaries in my sample would benefit from additional observations, which could significantly decrease the uncertainty of the measured q 's. Future observations of the long period systems should be postponed several years, until the orbital phase has changed significantly. At that time, additional long period systems, which were excluded from the original sample because their current orbital phase predicted a small velocity separation, could also be observed. An infrared spectrometer with higher resolution than CSHELL or NIRSPEC might allow these systems to be observed now and with increased precision. Such an instrument, however, does not currently exist.

Extending the the sample to binaries with smaller q is difficult. Low mass companions do not induce large velocities on their primary stars, so identifying these systems as SB1s is challenging. Even if they are detected as SB1s, the flux ratios are very small, and so the companions are difficult to detect spectroscopically. Guenther et al. (2005) are searching for very low mass companions in the Hyades by combining the long term radial velocity monitoring of candidate host stars with AO-imaging; they have detected very few companions with substellar mass, and estimate that the fraction of brown dwarf companions with

semi-major axis within 8 AU of the parent star is $\lesssim 2\%$. The companion to vB 142 may indeed be a brown dwarf, however additional measurements of the system are necessary to reduce the large uncertainty on q .

Latham and colleagues are currently expanding their SB1 sample to binaries with lower mass primaries. These systems are faint and so observing them requires a significant amount of time on a large telescope. Most SB1s that might be discovered in this regime would be out of reach of CSHELL, and would instead require NIRSPEC observations to detect the secondary. The simulations by Bate and colleagues suggest that short period binaries form with low mass primaries at a lower frequency than with more massive primaries because fewer dynamical interactions occur among low mass stars. If true, this population of SB2s may have little effect on the overall mass ratio distribution for the cluster.

The Hyades is a relatively small cluster. Investigations similar to the one presented here should be carried out in larger clusters to provide better statistics and perhaps clarify the role that the local environment plays on star formation. Currently, these studies are hampered because detailed surveys for SB1s are not yet complete (e.g. Kenyon et al., 2005; González & Levato, 2006; Stassun & Mathieu, 2006). Over the next decade, potentially large samples of binaries suitable for measurement with infrared spectroscopy will become available and should illuminate many currently unresolved questions.

Bibliography

- Baraffe, I., Chabrier, G., Allard, F., & Hauschildt, P. H. 1998, *A&A*, 337, 403
- Bate, M. R. & Bonnell, I. A. 1997, *MNRAS*, 285, 33
- Bate, M. R., Bonnell, I. A., & Bromm, V. 2002, *MNRAS*, 336, 705
- Bodenheimer, P. 1995, *ARA&A*, 33, 199
- Bonnell, I. A., Bate, M. R., & Vine, S. G. 2003, *MNRAS*, 343, 413
- Carney, B. W., Latham, D. W., Laird, J. B., & Aguilar, L. A. 1994, *AJ*, 107, 2240
- Clarke, C. J. 2001, in *IAU Symposium 200*, ed. H. Zinnecker & R. Mathieu, 346
- Clarke, C. J., Bonnell, I. A., & Hillenbrand, L. A. 2000, in *Protostars and Planets IV*, ed. A. Mannings, V. Boss & S. S. Russell, 151
- Cox, A. N. 2000, *Allen's Astrophysical Quantities* (4th ed. New York; Springer)
- de Bruijne, J. H. J., Hoogerwerf, R., & de Zeeuw, P. T. 2001, *A&A*, 367, 111
- Duquennoy, A. & Mayor, M. 1991, *A&A*, 248, 485
- Fisher, R. T. 2004, *ApJ*, 600, 769
- González, J. F. & Levato, H. 2006, in *Revista Mexicana de Astronomía y Astrofísica Conference Series*, 171
- Griffin, R. F., Griffin, R. E. M., Gunn, J. E., & Zimmerman, B. A. 1988, *AJ*, 96, 172
- Guenther, E. W., Paulson, D. B., Cochran, W. D., Patience, J., Hatzes, A. P., & Macintosh, B. 2005, *A&A*, 442, 1031
- Hanson, R. B. 1975, *AJ*, 80, 379
- Heintz, W. D. 1978, *Double Stars* (Revised ed. Dordrecht; Reidel)

- Hillenbrand, L. A. 1997, *AJ*, 113, 1733
- Horton, A. J., Bate, M. R., & Bonnell, I. A. 2001, *MNRAS*, 321, 585
- Kenyon, M. J., Jeffries, R. D., Naylor, T., Oliveira, J. M., & Maxted, P. F. L. 2005, *MNRAS*, 356, 89
- Kraft, R. P. 1965, *ApJ*, 142, 681
- Lebreton, Y., Fernandes, J., & Lejeune, T. 2001, *A&A*, 374, 540
- Mazeh, T., Prato, L., Simon, M., Goldberg, E., Norman, D., & Zucker, S. 2002, *ApJ*, 564, 1007
- Mazeh, T., Simon, M., Prato, L., Markus, B., & Zucker, S. 2003, *ApJ*, 599, 1344
- Patience, J., Ghez, A. M., Reid, I. N., Weinberger, A. J., & Matthews, K. 1998, *AJ*, 115, 1972
- Perryman, M. A. C., Brown, A. G. A., Lebreton, Y., Gomez, A., Turon, C., de Strobel, G. C., Mermilliod, J. C., Robichon, N., Kovalevsky, J., & Crifo, F. 1998, *A&A*, 331, 81
- Reid, N. 1992, *MNRAS*, 257, 257
- Spitzer, L. 1998, *Physical Processes in the Interstellar Medium* (New York; Wiley)
- Stassun, K. & Mathieu, R. 2006, in American Astronomical Society Meeting Abstracts
- Stauffer, J. R., Hartmann, L. W., & Latham, D. W. 1987, *ApJ*, 320, L51
- Tohline, J. E. 2002, *ARA&A*, 40, 349
- van Altena, W. F. 1969, *AJ*, 74, 2
- van Bueren, H. G. 1952, *Bull. Astron. Inst. Netherlands*, 11, 385

Table 3.1. Hyades SB1 Sample

Target	HD	R.A. (J2000)	Dec. (J2000)	Sp. Type	V	H	Period (days)	q_{\min}
vB 8.....	25102	03 59 40.49	+10 19 49.4	F5	6.4	5.4	854	0.15 ± 0.02
vB 9.....	...	04 00 39.54	+20 22 49.5	G4	8.7	7.0	5074	0.24 ± 0.03
L20.....	284163	04 11 56.22	+23 38 10.8	K0	9.4	6.6	2.4	0.59 ± 0.04
H69.....	...	04 12 21.44	+16 15 03.5	M1	14.0	9.1	128	0.57 ± 0.09
vB 30.....	27397	04 19 57.70	+14 02 06.7	F0	5.6	5.0	2.5	0.19 ± 0.01
L33.....	286770	04 22 25.69	+11 18 20.6	K8	9.8	7.1	1045	0.32 ± 0.03
vB 40.....	27691	04 22 44.17	+15 03 21.9	G0	7.0	5.6	4.0	0.32 ± 0.01
vB 39.....	27685	04 22 44.78	+16 47 27.7	G4	7.8	6.3	4578	0.44 ± 0.07
vB 43.....	284414	04 23 22.85	+19 39 31.2	K2	9.4	7.3	590	0.37 ± 0.02
vB 59.....	28034	04 26 05.86	+15 31 27.6	G8	7.5	6.2	5724	0.35 ± 0.06
vB 62.....	28033	04 26 18.50	+21 28 13.6	F8	7.4	6.1	8.6	0.16 ± 0.01
H382.....	28068	04 26 24.61	+16 51 12.0	G1	8.0	6.6	2657	0.47 ± 0.05
H411.....	285828	04 27 25.34	+14 15 38.5	K2	10.3	7.8	460	0.18 ± 0.02
L57.....	285766	04 27 58.96	+18 30 00.9	K2	10.2	7.7	1911	0.49 ± 0.04
vB 68.....	28294	04 28 23.40	+14 44 27.5	F0	5.9	5.1	332	0.37 ± 0.03
vB 69.....	28291	04 28 37.21	+19 44 26.5	G5	8.6	7.0	42	0.09 ± 0.01
H441.....	285806	04 28 50.81	+16 17 20.3	K7	10.7	7.6	7494	0.51 ± 0.06
vB 77.....	28394	04 29 20.55	+17 32 41.8	F7	7.0	5.8	239	0.19 ± 0.02

Table 3.1—Continued

Target	HD	R.A. (J2000)	Dec. (J2000)	Sp. Type	<i>V</i>	<i>H</i>	Period (days)	q_{\min}
H509	28634	04 31 37.10	+17 42 35.2	K2	9.5	7.3	850	0.36 ± 0.03
H532	286839	04 32 25.65	+13 06 47.6	K0	11.0	7.8	1.5	0.54 ± 0.03
vB 96	285931	04 33 58.54	+15 09 49.0	K0	8.5	6.6	5144	0.35 ± 0.03
L79	04 34 10.73	+11 33 29.6	K7	11.7	8.3	3688	0.28 ± 0.03
L77	04 34 49.76	+20 23 41.6	K7	11.1	8.0	2031	0.61 ± 0.07
vB 102	29310	04 37 31.98	+15 08 47.2	G1	7.5	6.1	735	0.15 ± 0.01
L90	29896	04 43 15.70	+17 04 08.8	K0	9.9	7.5	4010	0.32 ± 0.04
vB 142	30246	04 46 30.39	+15 28 19.4	G5	8.3	6.8	976	0.04 ± 0.01
vB 113	30311	04 46 45.58	+09 01 02.7	F5	7.2	5.9	2429	0.22 ± 0.02
vB 114	30355	04 47 37.57	+18 15 31.4	G0	8.5	6.9	5083	0.29 ± 0.03
vB 115	284787	04 48 42.12	+21 06 03.6	G5	9.1	7.2	1208	0.30 ± 0.02
vB 121	30738	04 50 48.54	+16 12 37.6	F8	7.3	6.2	5.8	0.16 ± 0.01
vB 151	240692	05 05 40.38	+06 27 54.6	K2	9.9	7.6	629	0.23 ± 0.02
BD+02 1102	40512	05 59 29.92	+02 28 34.2	F5	7.8	6.7	32	0.33 ± 0.02

Table 3.2. Log of Hyades Observations

Target	UT Date	JD-2400000	Instrument	V_2 (km s^{-1})
vB 8.....	2004 Oct 4	53282.97	C	58.5 ± 1.5
	2005 Sep 30	53643.98	C	-4.0 ± 2.0
vB 9.....	2004 Oct 2	53280.98	C	31.8 ± 2.1
	2004 Oct 4	53282.99	C	32.9 ± 1.8
L20	2004 Oct 1	53279.96	C	153.9 ± 12.1
	2004 Oct 2	53280.95	C	-57.0 ± 6.7
	2004 Oct 3	53282.15	C	137.2 ± 5.7
	2005 Oct 3	53647.11	C	-6.3 ± 6.0
H69.....	2004 Oct 3	53282.00	C	60.4 ± 2.6
	2005 Feb 22	53423.71	N	53.9 ± 4.3
	2006 Feb 3	53769.73	C	45.7 ± 6.8
vB 30	2004 Oct 3	53282.03	C	...
	2004 Oct 4	53283.03	C	...
L33	2004 Oct 3	53281.96	C	32.1 ± 1.3
	2005 Oct 2	53646.02	C	42.5 ± 2.6
	2005 Nov 26	53700.82	C	44.5 ± 2.2
vB 40	2004 Oct 1	53280.01	C	-45.5 ± 1.9
	2004 Oct 3	53282.12	C	132.9 ± 3.0
	2005 Oct 2	53645.96	C	117.7 ± 5.8
	2005 Oct 3	53647.02	C	52.9 ± 4.6
vB 39	2006 Feb 2	53768.73	C	...
	2006 Nov 26	53700.87	C	...
vB 43	2004 Oct 3	53282.05	C	42.2 ± 2.5
	2005 Feb 22	53423.75	N	48.0 ± 2.0
	2005 Sep 30	53644.01	C	...
	2005 Nov 27	53701.75	C	35.0 ± 2.2
vB 59	2005 Nov 27	53701.81	C	34.2 ± 4.4
	2006 Feb 2	53768.81	C	36.9 ± 2.9

Table 3.2—Continued

Target	UT Date	JD-2400000	Instrument	V_2 (km s^{-1})
vB 62	2004 Oct 1	53280.05	C	85.1 ± 4.6
	2005 Nov 25	53699.78	C	89.6 ± 10.9
	2005 Nov 28	53702.76	C	-21.4 ± 3.2
H382.....	2005 Nov 28	53702.80	C	53.2 ± 4.0
	2006 Feb 2	53768.75	C	50.9 ± 1.2
H411.....	2004 Oct 3	53282.08	C	...
	2005 Oct 2	53646.06	C	...
L57	2004 Oct 3	53282.10	C	46.7 ± 2.0
	2005 Nov 25	53699.83	C	...
	2006 Feb 2	53768.89	C	...
vB 68	2005 Oct 3	53657.07	C	22.8 ± 1.1
vB 69	2004 Oct 1	53280.08	C	-4.1 ± 2.0
	2005 Sep 30	53644.04	C	48.1 ± 3.1
	2005 Nov 27	53701.79	C	17.7 ± 5.2
H441.....	2005 Nov 28	53702.95	C	31.7 ± 3.9
	2006 Feb 2	53768.84	C	32.7 ± 2.6
vB 77	2004 Oct 1	53280.10	C	22.7 ± 4.9
	2005 Nov 30	53644.12	C	45.2 ± 1.9
H509.....	2004 Oct 2	53281.12	C	51.5 ± 2.8
	2005 Oct 2	53646.10	C	...
	2006 Feb 2	53768.79	C	27.0 ± 2.0
H532.....	2004 Oct 2	53281.01	C	-61.9 ± 5.3
	2004 Oct 4	53283.06	C	67.5 ± 7.5
	2005 Nov 26	53700.92	C	24.9 ± 10.2
vB 96	2006 Feb 3	53769.92	C	44.6 ± 1.6
L79	2006 Feb 3	53769.79	C	45.9 ± 2.8
L77	2006 Feb 3	53769.84	C	27.1 ± 2.7

Table 3.2—Continued

Target	UT Date	JD-2400000	Instrument	V_2 (km s^{-1})
vB 102	2004 Oct 2	53281.04	C	45.0 ± 2.1
	2005 Sep 30	53644.07	C	25.0 ± 1.9
	2006 Feb 2	53768.92	C	4.0 ± 3.2
L90	2005 Nov 25	53699.88	C	...
	2006 Feb 3	53769.89	C	...
vB 142	2004 Oct 1	53280.12	C	54.2 ± 2.1
	2005 Feb 22	53423.86	N	17.2 ± 6.4
	2005 Oct 1	53645.10	C	29.0 ± 3.5
	2005 Nov 28	53702.91	C	20.2 ± 1.8
vB 113	2004 Oct 2	53281.07	C	51.3 ± 1.7
	2005 Oct 1	53645.06	C	52.7 ± 2.7
vB 114	2005 Nov 27	53701.93	C	...
vB 115	2004 Oct 4	53283.08	C	51.0 ± 1.8
	2005 Nov 27	53701.89	C	34.3 ± 1.8
vB 121	2004 Oct 1	53280.14	C	-52.2 ± 3.0
	2004 Oct 3	53282.13	C	84.3 ± 4.1
	2005 Nov 28	53702.94	C	70.6 ± 7.0
vB 151	2004 Oct 4	53283.11	C	28.7 ± 3.3
	2005 Oct 2	53646.13	C	51.9 ± 1.9
	2005 Nov 25	53699.93	C	54.9 ± 3.5
BD+02 1102	2004 Oct 4	53283.14	C	24.5 ± 4.8
	2005 Oct 1	53645.13	C	32.3 ± 6.2

Table 3.3. Measured Mass Ratios for IR SB2s

Target	N_{obs}	N_{det}	K_2 (km s $^{-1}$)	q	α
vB 8	2	2	55.6 \pm 6.5	0.06 \pm 0.02	0.17 \pm 0.08
vB 9	2	2	7.5 \pm 0.9	0.36 \pm 0.05	0.11 \pm 0.02
L20	4	4	111.3 \pm 7.1	0.60 \pm 0.04	0.11 \pm 0.03
H69	3	3	23.9 \pm 1.8	0.58 \pm 0.04	0.23 \pm 0.07
vB 30	2	0
L33	3	3	8.2 \pm 0.6	0.69 \pm 0.05	0.70 \pm 0.10
vB 40	4	4	87.5 \pm 2.7	0.46 \pm 0.01	0.11 \pm 0.02
vB 39	2	0
vB 43	4	3	14.5 \pm 1.2	0.66 \pm 0.05	0.27 \pm 0.04
vB 59	2	2	83.5 \pm 28.1	0.18 \pm 0.06	0.03 \pm 0.02
vB 62	3	3	72.6 \pm 8.8	0.23 \pm 0.03	0.07 \pm 0.01
H382	3	2	21.1 \pm 2.4	0.37 \pm 0.05	0.06 \pm 0.01
H411	3	0
L57	3	1	7.7 \pm 2.1	0.86 \pm 0.23	0.12 \pm 0.05
vB 68	1	1	16.1 \pm 2.4	0.70 \pm 0.11	...
vB 69	3	3	44.0 \pm 5.9	0.16 \pm 0.02	0.08 \pm 0.02
H441	2	2	8.0 \pm 0.3	0.45 \pm 0.03	0.52 \pm 0.11
vB 77	2	2	20.0 \pm 1.8	0.33 \pm 0.03	0.09 \pm 0.04
H509	3	2	13.7 \pm 4.0	0.46 \pm 0.14	0.18 \pm 0.05
H532	3	3	93.9 \pm 14.8	0.73 \pm 0.17	0.24 \pm 0.05
vB 96	1	1	9.6 \pm 3.5	0.50 \pm 0.18	0.46 \pm 0.29
L79	1	1	27.2 \pm 18.9	0.16 \pm 0.11	0.41 \pm 0.26
L77	1	1	24.2 \pm 4.9	0.30 \pm 0.06	0.25 \pm 0.10
vB 102	3	3	33.8 \pm 9.8	0.12 \pm 0.03	0.08 \pm 0.01
L90	2	0
vB 142	4	4	21.2 \pm 14.0	0.06 \pm 0.04	0.05 \pm 0.01

Table 3.3—Continued

Target	N_{obs}	N_{det}	K_2 (kms $^{-1}$)	q	α
vB 113.....	2	2	12.6 \pm 4.8	0.27 \pm 0.10	0.06 \pm 0.01
vB 114.....	1	0
vB 115.....	2	2	10.9 \pm 3.7	0.52 \pm 0.18	0.07 \pm 0.02
vB 121.....	3	3	100.9 \pm 17.5	0.20 \pm 0.03	0.05 \pm 0.03
vB 151.....	3	3	9.8 \pm 2.2	0.53 \pm 0.12	0.11 \pm 0.03
BD+02 1102.....	2	2	53.3 \pm 20.5	0.40 \pm 0.15	...

Table 3.4. Derived Component Masses for IR SB2s

Target	M_1 (M_\odot)	M_2 (M_\odot)
vB 8	1.38 ¹	0.08
vB 9	1.13 ¹	0.41
L20	0.88 ¹	0.53
H69	0.46	0.27
vB 30
L33	0.90 ¹	0.62
vB 40	1.35 ¹	0.62
vB 39
vB 43	0.99 ¹	0.65
vB 59	0.96 ¹	0.17
vB 62	1.23 ¹	0.28
H382	1.08 ¹	0.40
H411
L57	0.74	0.64
vB 68	1.60 ¹	1.12
vB 69	1.01 ¹	0.16
H441	0.61	0.27
vB 77	1.27 ¹	0.42
H509	0.82 ¹	0.38
H532	0.76 ¹	0.55
vB 96	0.97 ¹	0.48
L79	0.61	0.10
L77	0.61	0.18
vB 102	1.17 ¹	0.14
L90
vB 142	1.09 ¹	0.06

Table 3.4—Continued

Target	M_1 (M_\odot)	M_2 (M_\odot)
vB 113.....	1.16 ¹	0.31
vB 114.....
vB 115.....	0.96 ¹	0.50
vB 121.....	1.30 ¹	0.26
vB 151.....	0.99 ¹	0.53
BD+02 1102.....	1.30 ¹	0.52

¹Primary mass estimate revised from initial estimate (see 3.6.1)

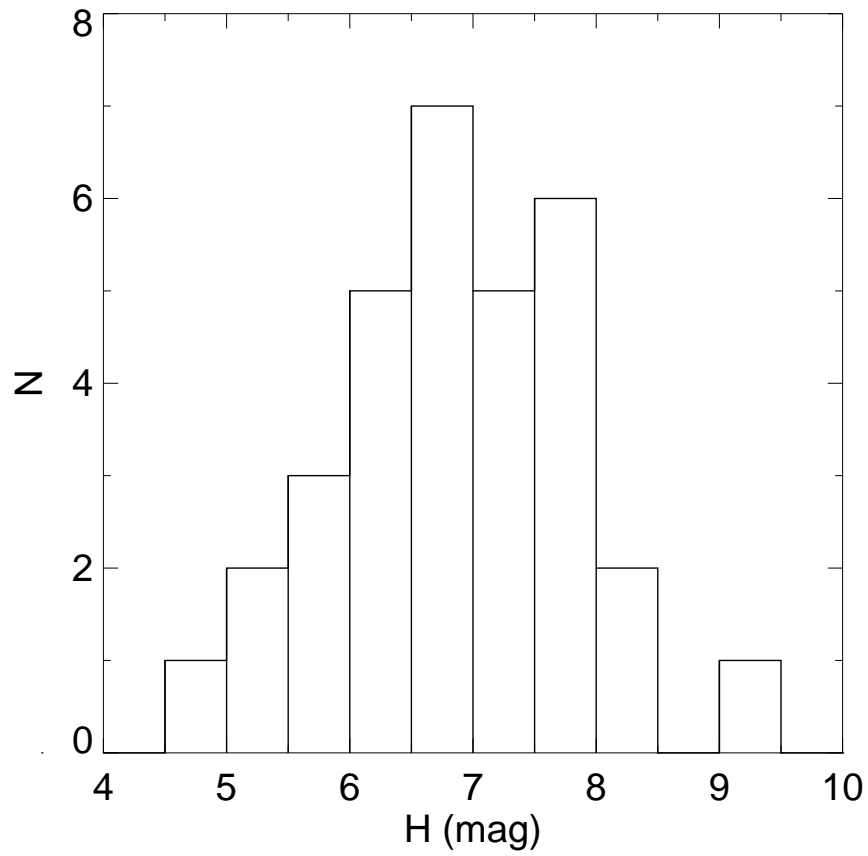


Figure 3.1 The distribution of H -magnitudes for the Hyades SB1 sample listed in Table 3.1, determined from 2MASS.

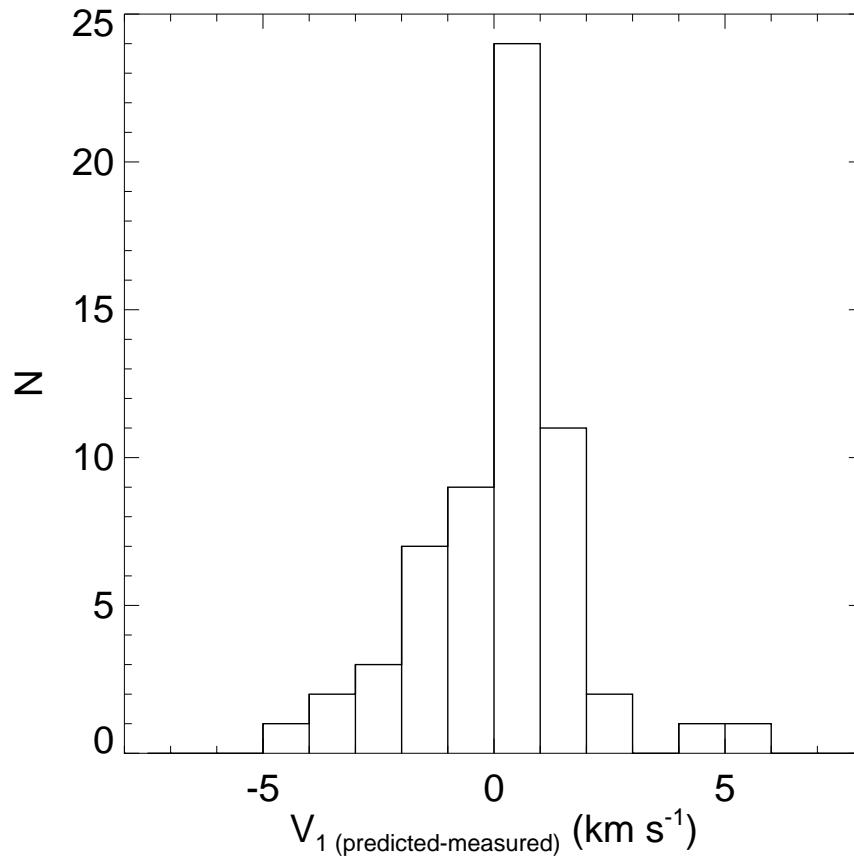


Figure 3.2 The distribution of the difference between the binary primary velocity predicted from the Latham SB1 solutions and the velocity measured in the infrared spectra. The outlying measurements with large velocity difference are attributable to spectra with a low signal-to-noise. The distribution has a mean value of $\sim 0.3 \text{ km s}^{-1}$, and a Gaussian fit to the distribution has width $\sim 0.9 \text{ km s}^{-1}$, indicating that Latham’s velocity reference frame and the infrared template velocity frame (see 2.3) agree to better than the measurement uncertainties.

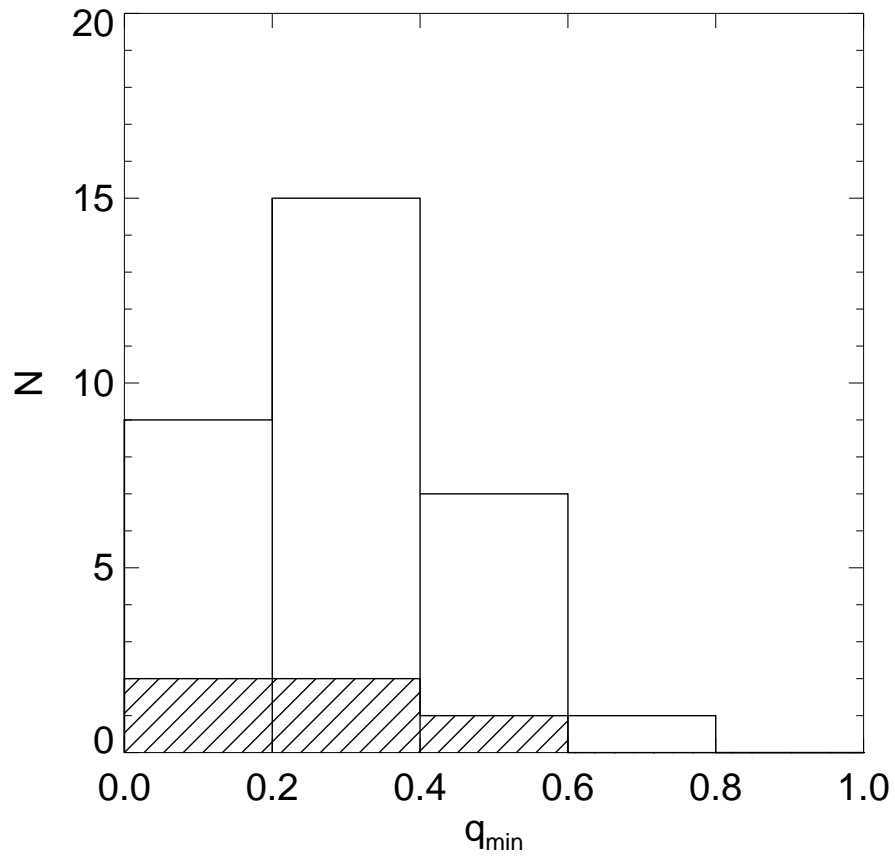


Figure 3.3 The distribution of q_{\min} for the systems detected (*open*) and not detected (*hashed*) as SB2s in the infrared. The distribution of q_{\min} for non-detections is similar to the distribution for detections.

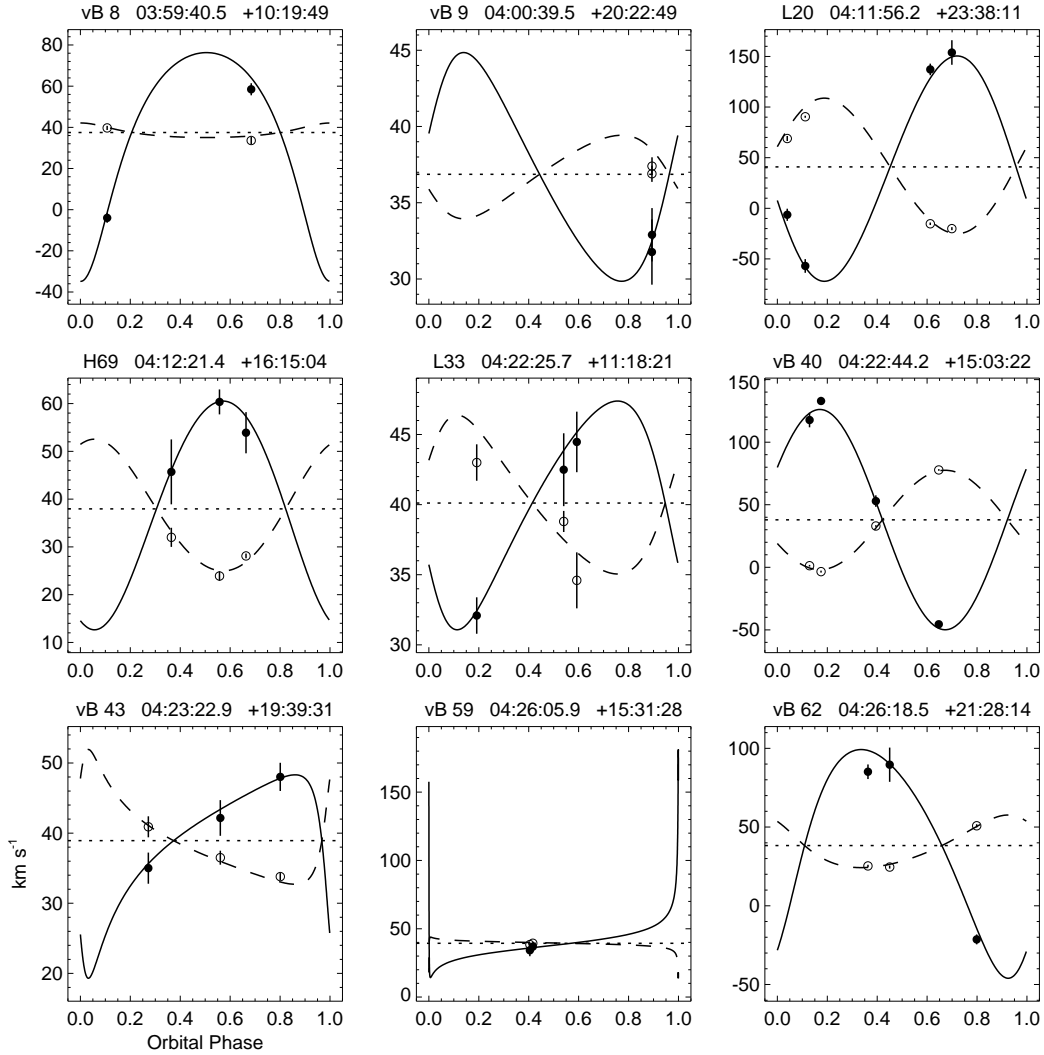


Figure 3.4 Velocity versus phase curves for Hyades binaries with secondaries detected in the infrared, from R.A. 3^h59^m to 4^h26^m . The dashed curve represents the visible light single-line solution of Latham and colleagues. The open circles are my measured infrared velocities for the primary components; these are shown only to demonstrate the level of agreement with Latham's solutions, and are not used in any orbit fitting. The filled circles are my measured velocities for the secondaries. The solid curve is the least squares solution to my secondary velocities, with P , e , T_0 , ω , and γ fixed from the single-lined solution. The dotted line indicates the center-of-mass velocity of the system.

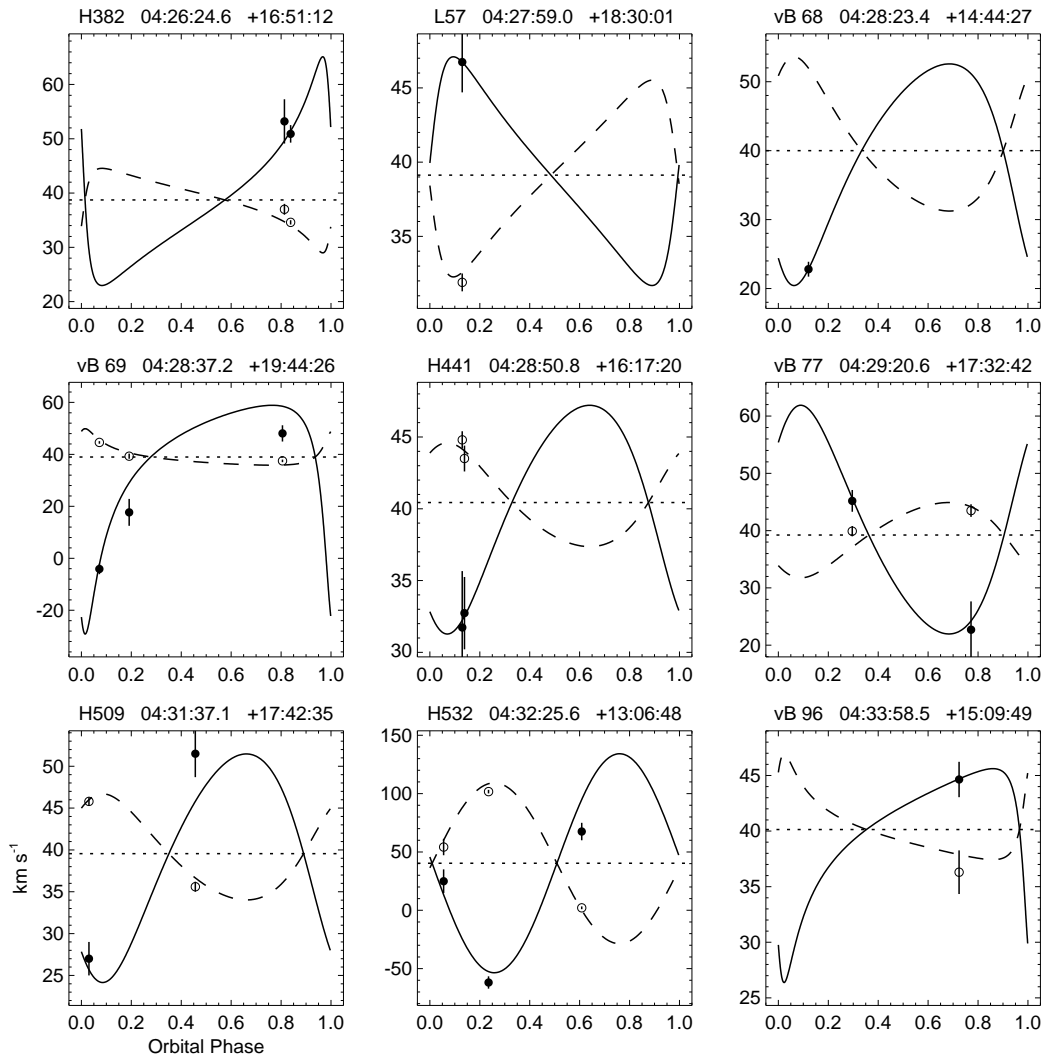


Figure 3.5 Same as Figure 3.4, from R.A. $4^h 26^m$ to $4^h 33^m$.

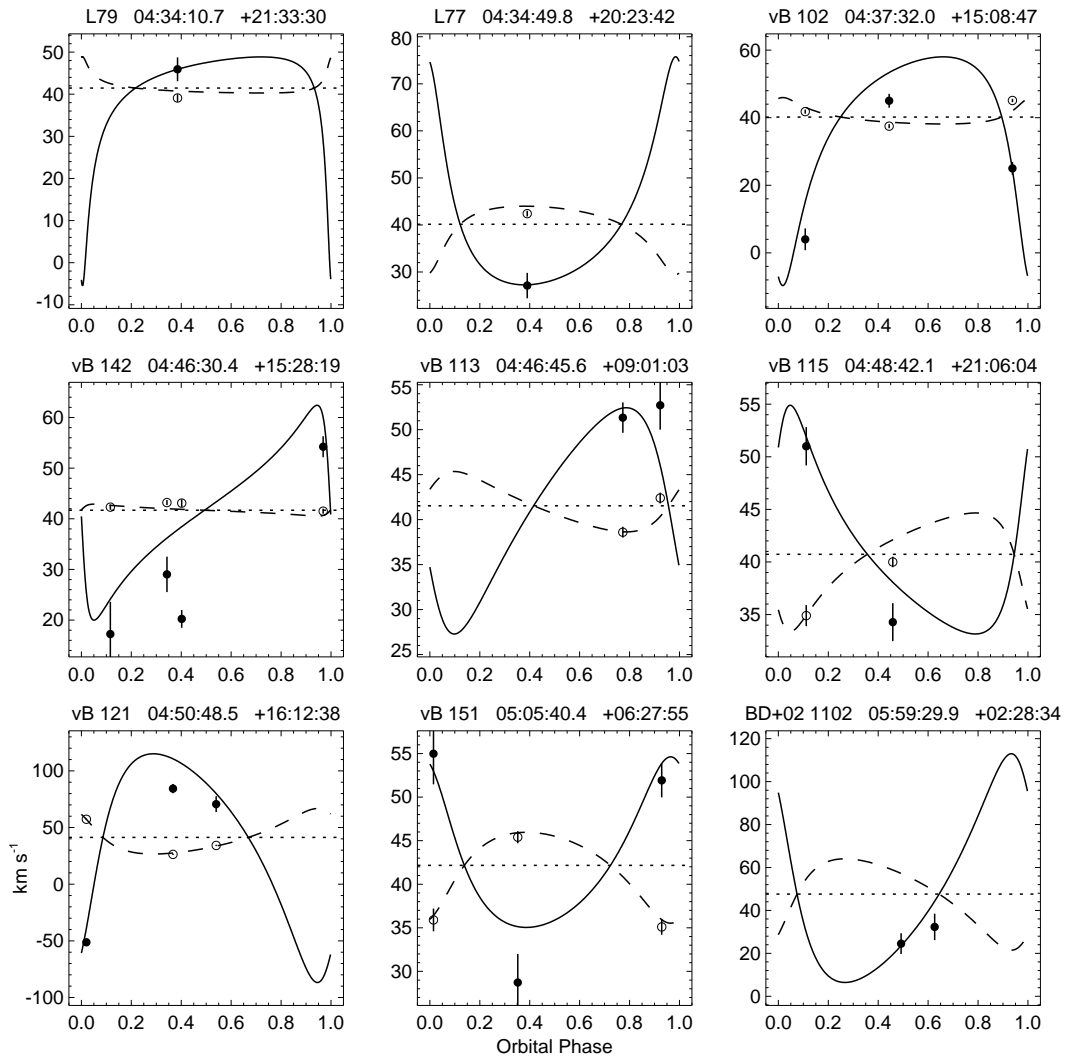


Figure 3.6 Same as Figure 3.4, from R.A. $4^{\text{h}}34^{\text{m}}$ to $5^{\text{h}}59^{\text{m}}$.

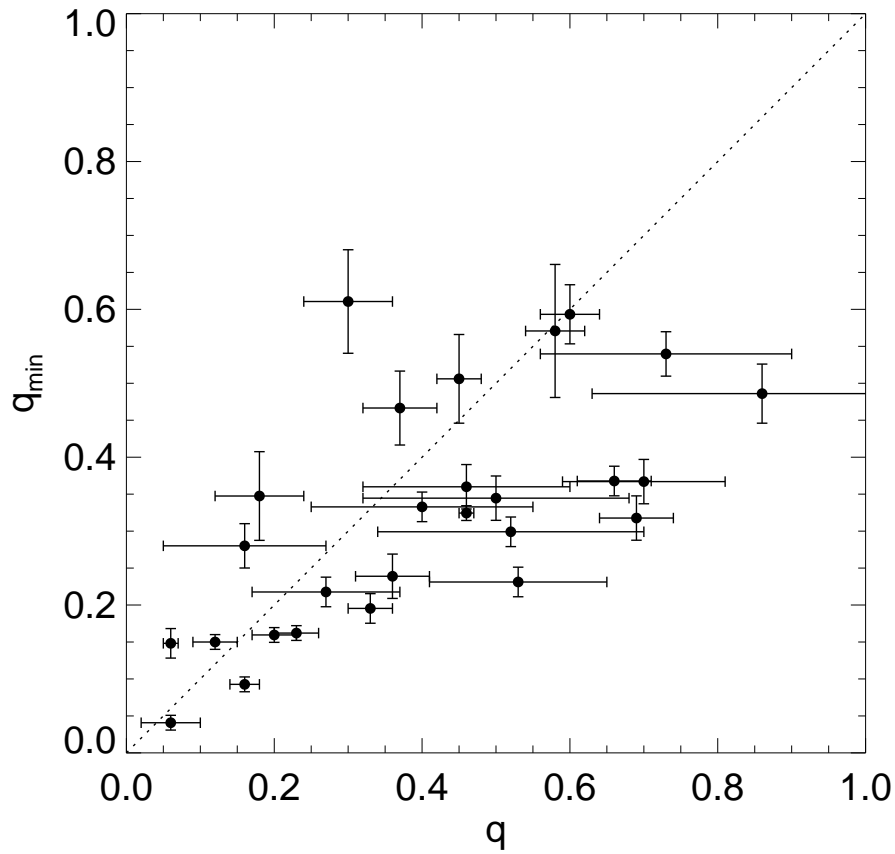


Figure 3.7 The minimum mass ratio, determined from the binary mass function, plotted against the measured mass ratio. The dotted line indicates $q_{\min} = q$. The measured mass ratio is greater than or within 1σ of q_{\min} for all binaries except vB 8 ($q = 0.06 \pm 0.01$) and L77 ($q = 0.30 \pm 0.06$).

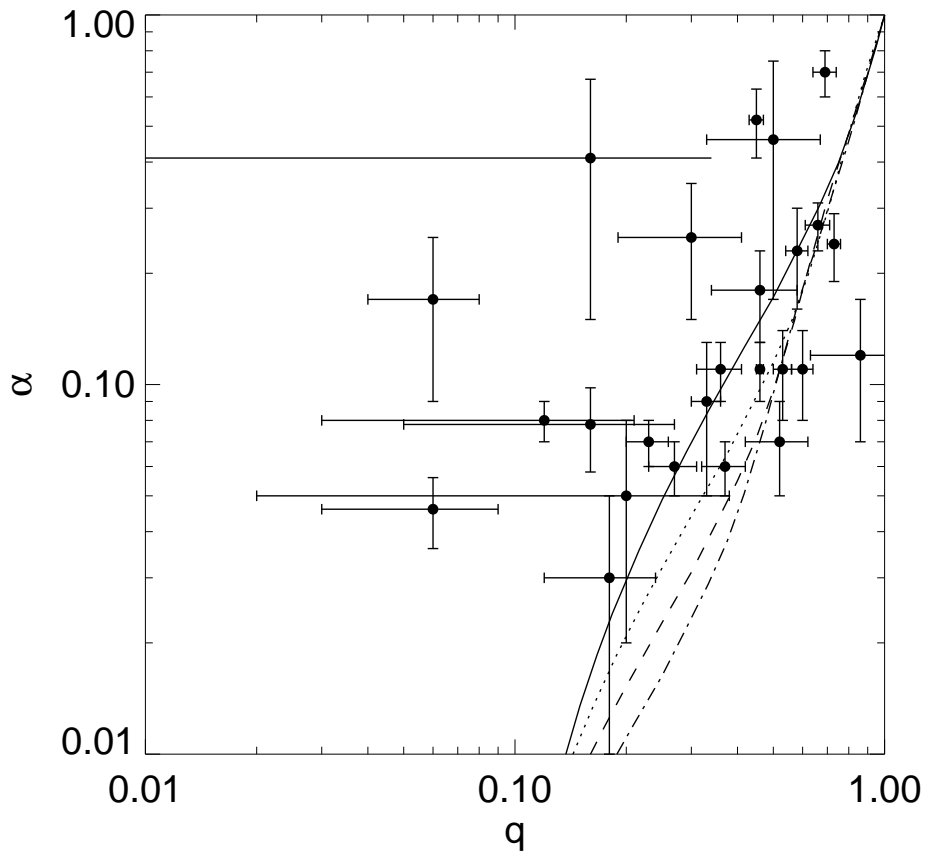


Figure 3.8 The measured flux ratio plotted against the measured mass ratio. The curves show the theoretical H -band flux ratios from Baraffe et al. (1998) for 650 Myr old binaries with primary masses of $0.6 M_{\odot}$ (*solid*), $0.8 M_{\odot}$ (*dotted*), $1.0 M_{\odot}$ (*dashed*), and $1.2 M_{\odot}$ (*dot-dashed*).

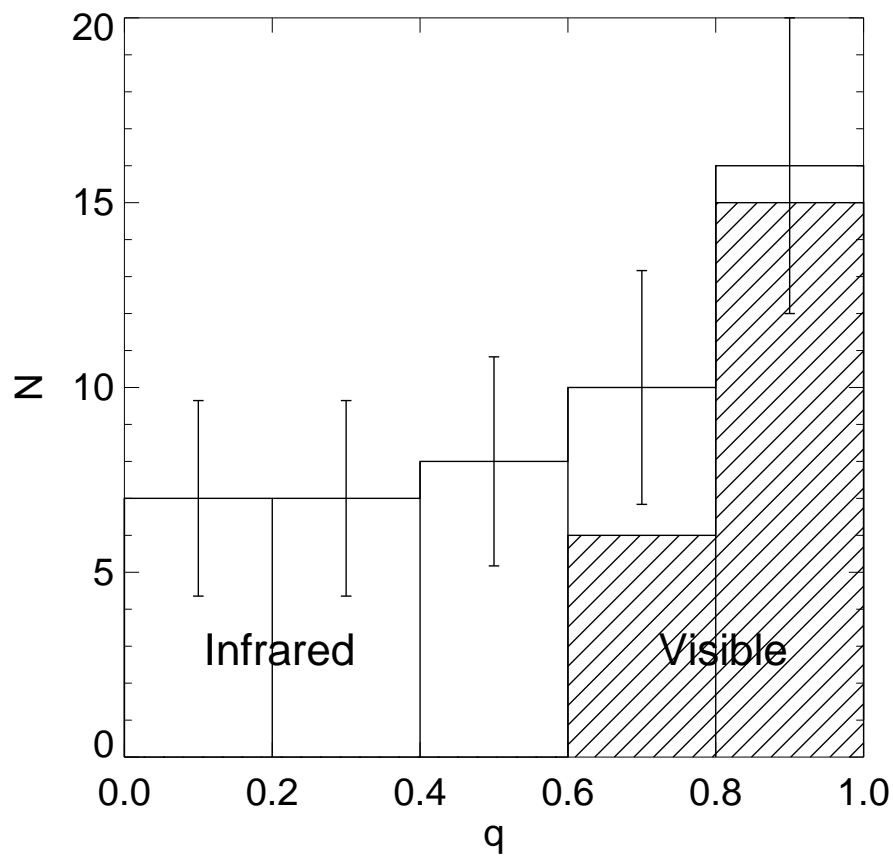


Figure 3.9 The measured mass ratio distribution for Hyades spectroscopic binaries, including those I measured in the infrared and those D. Latham and colleagues measured in the visible.

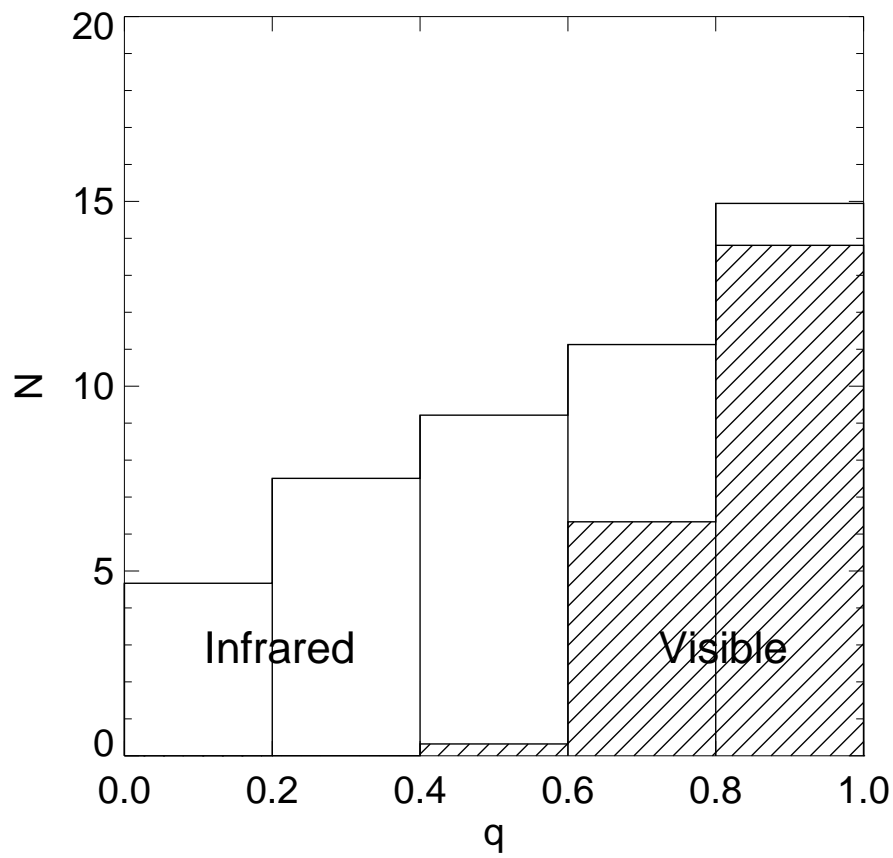


Figure 3.10 Same as Figure 3.9, but with the mass ratios distributed over Gaussians with widths equal to the 1σ measurement uncertainty. The Gaussians are clipped at $q = q_{min} - 2 \times \sigma_{q_{min}}$ and $q = 1$, and renormalized.

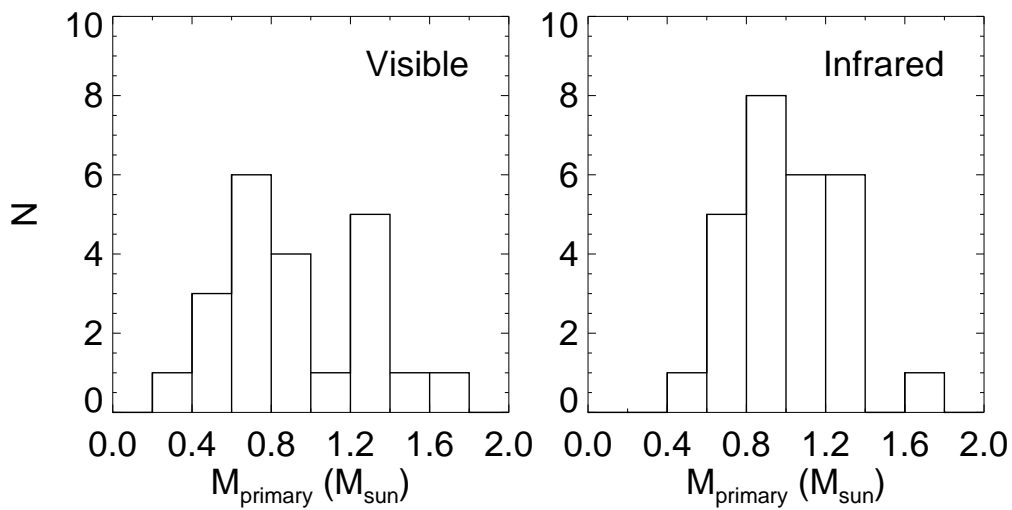


Figure 3.11 The distribution of primary masses for the Hyades SB2s. The sample includes the binaries observed as SB2s in the visible (*left*) and infrared (*right*), shown in Figures 3.9 and 3.10. I estimated the masses of stars with *Hipparcos* distances by combining their 2MASS photometry and measured q with the models of Baraffe et al. (1998); this corresponds roughly to stars of spectral type K5 and earlier. The masses of later type stars without *Hipparcos* distances were estimated from their spectral types (Cox, 2000, ch. 7). All primary mass estimates have an uncertainty of $\sim \pm 0.1 M_{\odot}$.

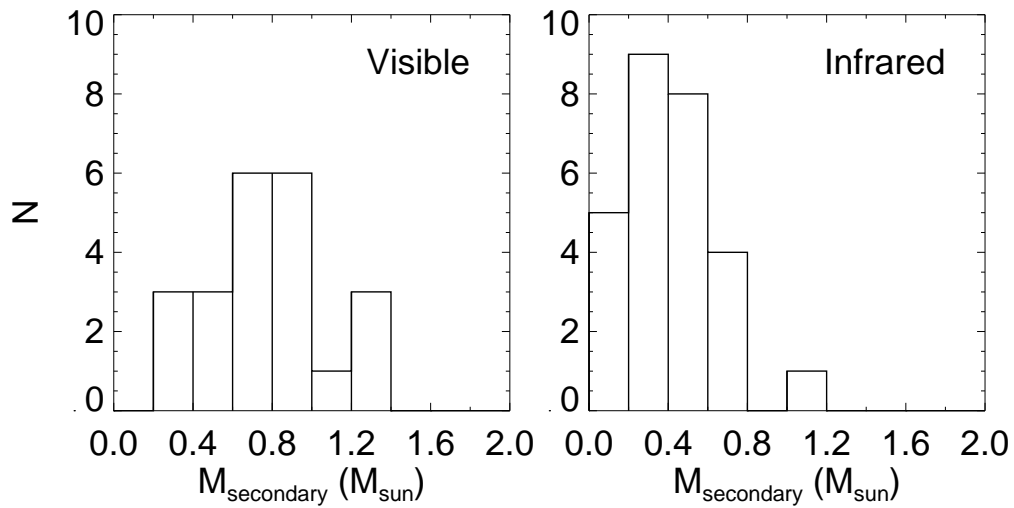


Figure 3.12 The distribution of the secondary masses of the visible (*left*) and infrared (*right*) Hyades SB2s, calculated from the primary mass estimates (Figure 3.11) and the measured mass ratios (Figure 3.9).

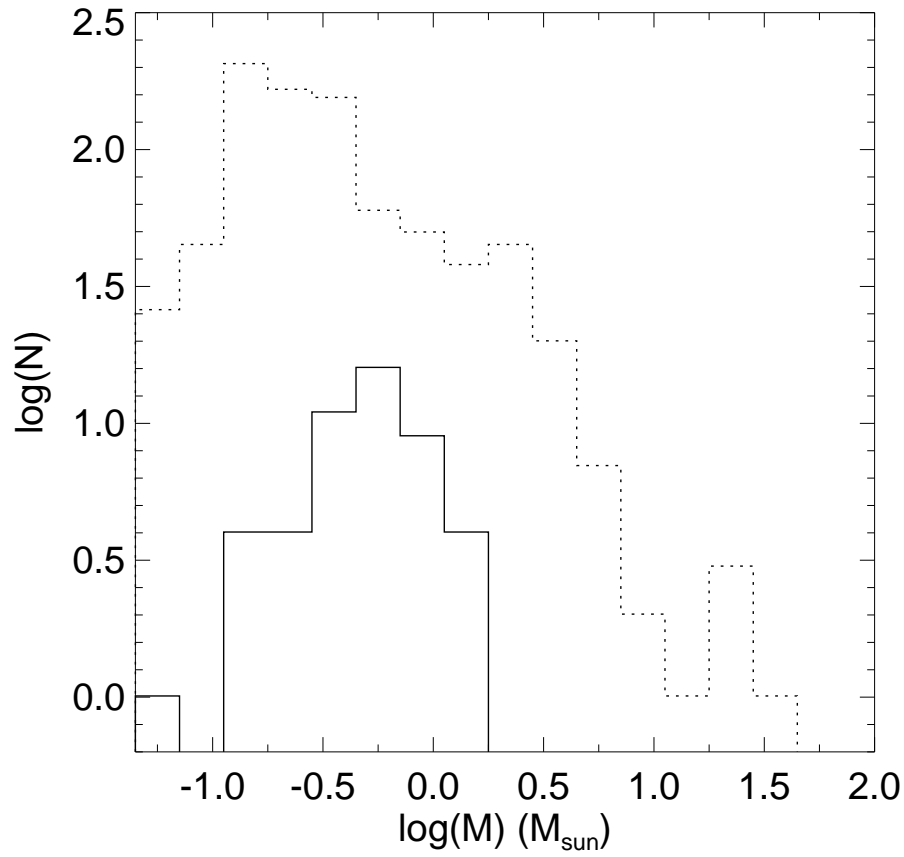


Figure 3.13 The measured IMF for the visible and infrared Hyades SB2 secondary masses (*solid*) compared with the IMF found by Hillenbrand (1997) for the 1 Myr old Orion Nebula Cluster (*dotted*). The distributions are offset in $\log(N)$ because the Hillenbrand survey includes a much larger sample than that of my Hyades SB2s.

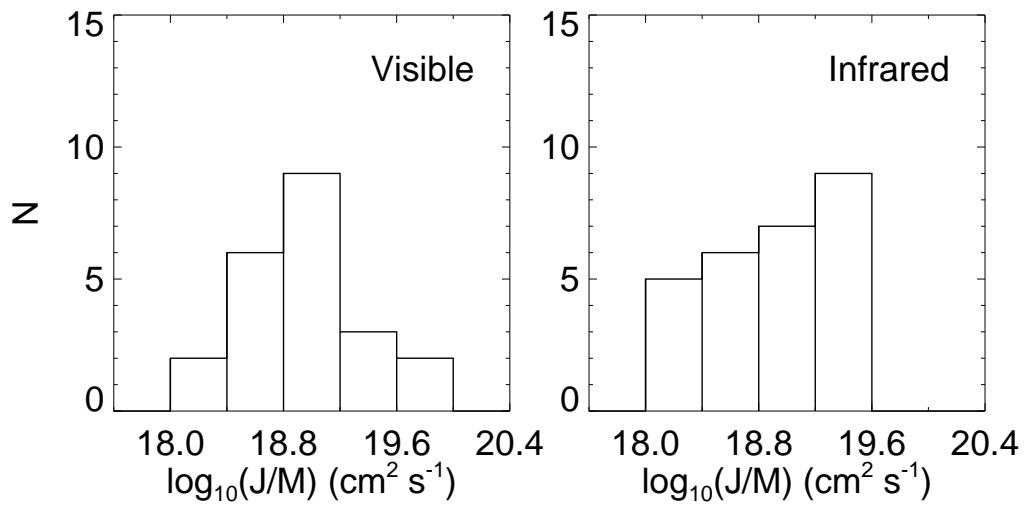


Figure 3.14 The distribution of J/M for the visible (*left*) and infrared (*right*) SB2s, calculated using the component masses in Figures 3.11 and 3.12, and the measured orbital parameters, a' , P , and e .

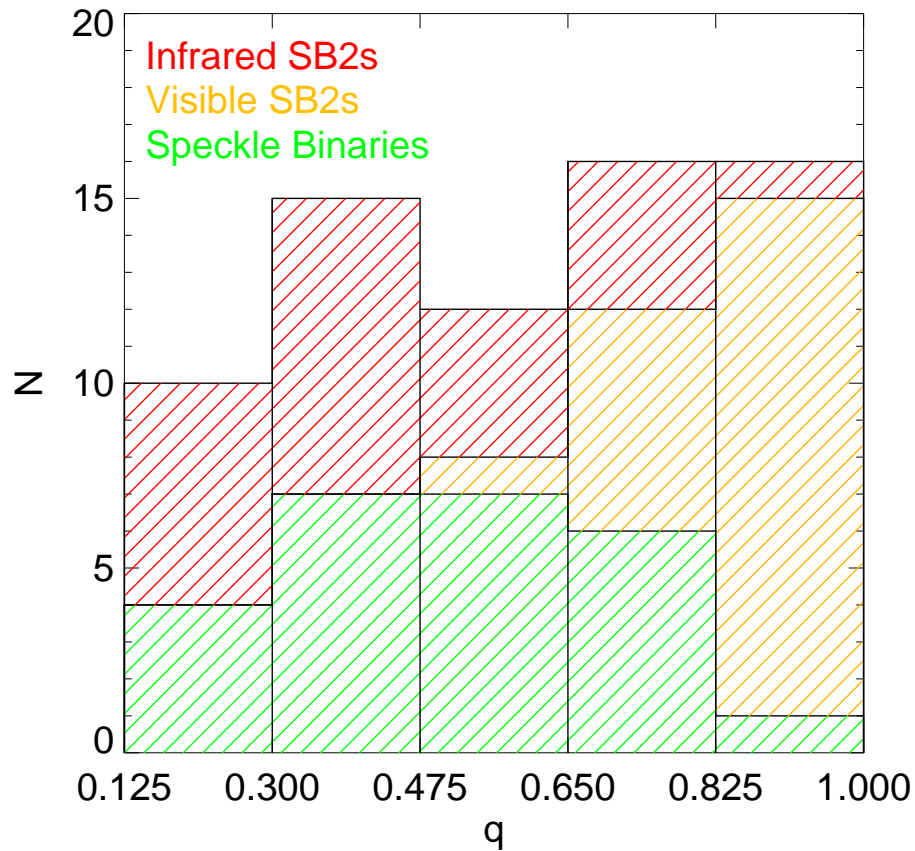


Figure 3.15 The combined mass ratio distribution for Hyades binaries. Visible and infrared SB2s, from Figure 3.9 are shown in orange and red, respectively. The wide speckle binaries from Patience et al. (1998, Fig. 6) are shown in green. The binning reflects that chosen by Patience et al. (1998); the speckle binaries are incomplete for $q < 0.30$. vB 113 is a member of the speckle sample and the infrared SB2 sample; it is shown here with the SB2s.

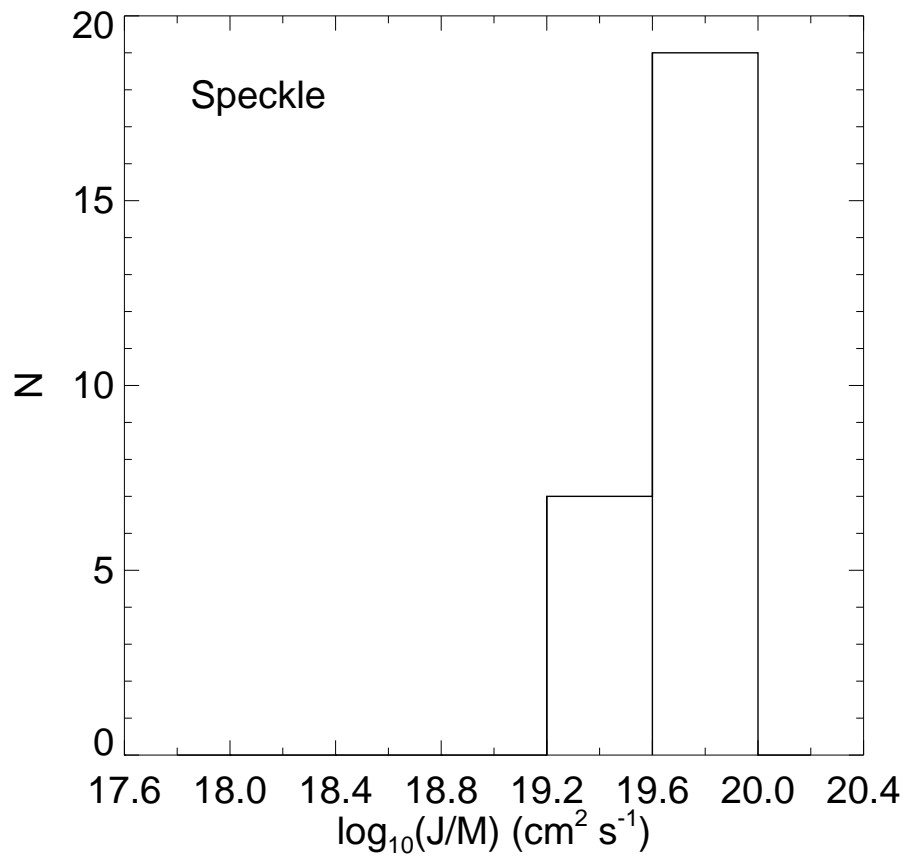


Figure 3.16 The distribution of J/M for the Patience et al. (1998) speckle binary sample, with semi-major axis from 5–50 AU. I assumed circular orbits and an average inclination for a randomly oriented sample of binaries.

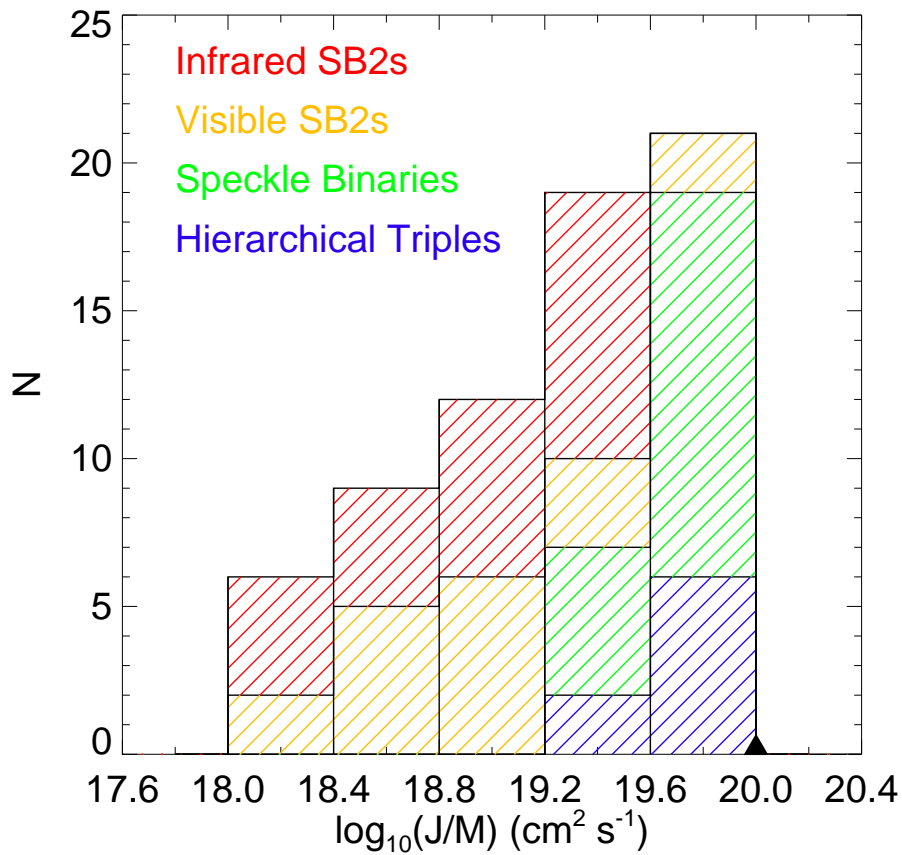


Figure 3.17 The combined distribution of J/M for infrared SB2s (*red*, Fig. 3.14 *right*), visible SB2s (*orange*, Fig. 3.14 *left*), and Patience et al. (1998) speckle binaries (*green*, Fig. 3.16). The infrared and visible SB2 samples each include four inner binaries of hierarchical triple systems for which Patience et al. (1998) observed the outer binary. The total J/M for these triple system is shown in *blue*; their binary contributions are excluded from the other distributions. The upward pointing arrowhead at $\log J/M \sim 20.0$ indicates where planets similar to Jupiter would lie.

Chapter 4

The Gl569 Multiple System

4.1 Introduction

Gl569 is a multiple system comprised of Gl569A, an M2.5 V star (Henry & Kirkpatrick, 1990) of mass $M = 0.35 \pm 0.03 M_{\odot}$ (Gorlova et al., 2003) and Gl569B, thought to be a brown dwarf binary with period of ~ 876 days (Zapatero Osorio et al., 2004). *Hipparcos* determined a distance to Gl569A of 9.81 ± 0.16 pc. The angular separation between A and B is $\sim 5''$. In 2002, M. Simon (MS), L. Prato (LP), and I began a study of Gl569B because the system is well suited to combining astrometric and spectroscopic techniques to measure dynamical masses: the Ba and Bb components are bright enough to be observed at high spectral resolution in the near-infrared, and the Ba–Bb astrometric orbit is well determined (e.g. Kenworthy et al., 2001; Lane et al., 2001; Zapatero Osorio et al., 2004). I present the results of our study in this chapter; they also appear in Simon et al. (2006).

4.2 Observations and Processing

4.2.1 NIRSPEC Spectroscopy

MS, LP, and I used NIRSPEC in its high-resolution mode on the 10 m Keck II telescope, with and without the AO system, to observe the Gl569 system from 2002 to 2005; Table 4.1 provides a log of the observations. Details of the observation and reduction procedures are given in Section 2.2.1. Strong terrestrial absorption features are present throughout NIRSPEC orders 45–53, and interfere with the cross-correlation technique used to analyze binary spectra. Order 49 and 2/3 of order 48 are nearly completely free of terrestrial absorption (e.g., Figure 2.2), and are the only orders used in the GL 569 analysis.

4.2.2 NIRC2 Imaging

NIRC2 is a high-resolution near-infrared imager used with the AO system on the Keck II telescope. The detector is a 1024×1024 pixel Alladin III InSb array. We imaged Gl569 with the NIRC2 narrow field camera, which has a plate scale of $0.''00942 \text{ pixel}^{-1}$ and an orientation angle of $0.^{\circ}7 \pm 0.^{\circ}2$ ¹. This provided a $9.''6$ field of view, sufficient to include both Gl569A and Gl569B simultaneously. We took data in the *H*- and *K*-bands, in sets of 10 images, using a five-point dither pattern with an offset of $2.''$. The integration times for each frame were 1.00 s on 2004 December 24 and 0.18 s on 2005 February 25. I flat-fielded the images with a dark-subtracted flat, and expanded the pixel scale by a factor of 10 to improve the

¹<http://www2.keck.hawaii.edu/inst/nirc2/>

measurement precision of the relative positions and photometry of Gl569A, Ba, and Bb. For the 2005 February 25 data, I used Gl569A to centroid the images for shifting and co-adding multiple exposures and to create an instrumental point-spread function (PSF) in the *H*- and *K*-bands. Gl569A was saturated in the 2004 December 24 data, so these images were co-added by cross-correlating and shifting for the greatest correlation, and were only useful for relative astrometry and photometry of Ba and Bb.

4.3 Results: GL 569A

The proper motion of Gl569A is $\mu_\alpha = 275.95$ and $\mu_\delta = -122.12 \text{ mas yr}^{-1}$ (*Hipparcos*). Thus, in the ~ 20 years since the discovery of Gl569B by Forrest et al. (1988), the A component has moved $\sim 6''$ on the sky. Astrometry from the February 2005 NIRC2 *H*- and *K*-band images showed the photocenter of Gl569B $4''.18 \pm 0''.21$ North, and $2''.72 \pm 0''.14$ East with respect to Gl569A (Table 4.2). This offset of B with respect to A lies $\sim 1''$ from that measured by Forrest et al. (1988) and confirms their finding that A and B form a common proper motion system. Figure 4.1 shows these measurements, together with the positions measured by Martín et al. (2000) and Lane et al. (2001), and clearly indicates the orbital motion of Gl569B with respect to A. The measurements to date are insufficient to determine the astrometric orbital parameters of the Gl569AB system, however if the orbit is face on it has a period of ~ 500 years.

Henry & Kirkpatrick (1990) used spectroscopy in visible light to show that the spectral type of Gl569A is M2.5 V. To measure the radial velocity of Gl569A and,

in the process, to estimate its spectral type, I analyzed the order 49 spectra obtained on 2003 April 20, 2003 June 14, and 2004 May 25 with a one-dimensional cross-correlation algorithm. The spectrum of the template star Gl436, spectral type M2.5 V (Prato et al., 2002), produced the highest correlation with the Gl569A spectrum, in agreement with Henry & Kirkpatrick’s result; the measured velocities are listed in Table 4.3. The difference between the average radial velocity measurement, $-7.7 \pm 0.6 \text{ km s}^{-1}$, and the center-of-mass velocity of the Ba–Bb pair (see 4.4.3) is $0.8 \pm 0.9 \text{ km s}^{-1}$. The velocity difference arising in the orbital motion of B with respect to A is expected to be small (see 4.5.1) and to lie below the significance limit of the measurements.

The apparent magnitudes of Gl569A at V and H are $10.200 \pm 0.004 \text{ mag}$ and $5.99 \pm 0.02 \text{ mag}$, respectively (*Hipparcos*, 2MASS). These correspond to absolute magnitudes $M_V = 10.24 \text{ mag}$ and $M_H = 6.3 \text{ mag}$ at a distance of 9.81 pc. Gorlova et al. (2003) used near-infrared surface gravity indicators and model stellar spectra to estimate that the mass of Gl569A is $0.35 \pm 0.03 M_\odot$. Figure 4.2 shows M_V and M_H versus mass using these values. Surprisingly, these mass-luminosity diagrams indicate an age of 20–40 Myr for Gl569A, much younger than the several hundred Myr age previously estimated for the Ba and Bb brown dwarfs (Lane et al., 2001; Zapatero Osorio et al., 2004). It is possible, however, that the theoretical isochrones underestimate the age of a star in this range of mass and age (I. Baraffe, private communication). An independent estimate of the age can be obtained by placing Gl569A on an empirically determined color-magnitude diagram. Figure 4.3 shows $V-K$ vs. M_K for the Pleiades cluster (Luhman et al.,

2005, Figure 1), thought to be 100–125 Myr old (Meynet et al., 1993; Stauffer et al., 1998). The scatter in M_K is due to undetected binary systems in the cluster; the main-sequence lies along the bottom of this scatter. Gl569A, shown as a filled circle, falls on the Pleiades main-sequence, indicating that it has similar age. Gl569A could be older than it appears in Figures 4.2 or 4.3 if it is fainter and its measured apparent magnitude represents that of two stars in a binary. However, its spectrum in both the visible and the infrared is that of an M2.5 V, with no evidence of a companion. Additionally, the measured radial velocities in Table 4.3 show no variability to the limit of the measurement uncertainty. The H - and K -band images from February 2005 also show no evidence of a companion. These measurements, therefore, strongly suggest that Gl569A is a single star with an age ~ 100 Myr, younger than the age previously estimated for its brown dwarf companions.

4.4 Results: Gl569B

4.4.1 Photometry, Astrometry, and Orbital Parameters of

Gl569B as a Visual Binary

Figure 4.4 shows the H - and K -band composite images of Gl569Ba and Bb from the 2005 February 25 NIRC2 observations. I modeled the brown dwarf binary as the sum of two scaled PSFs; the single star PSF was provided by the simultaneously obtained image of Gl569A, which had FWHM = 41 mas at H and 52 mas at K . The AO correction achieved a Strehl ratio of ~ 0.3 at H and ~ 0.4 at K .

I used least squares fitting to determine the positions and amplitudes of Ba and Bb relative to each other and to Gl569A. The 2MASS magnitudes of Gl569A at H and K , 5.99 ± 0.02 mag and 5.77 ± 0.02 mag, respectively, were used to determine the magnitudes of Ba and Bb. The astrometric and photometric results are given in Table 4.4. Because Gl569A was not usable as a PSF in the 2004 December 24 data (see 4.2.2), I measured the position of Bb relative to Ba by modeling the PSF as an elliptical Gaussian and fitting to the composite image; the astrometric results and Bb/Ba flux ratios are included in Table 4.4. Ba is 0.53 ± 0.08 magnitudes brighter than Bb at K , consistent with the measurement of Lane et al. (2001), and 0.61 ± 0.07 magnitudes brighter at H .

Observations of a visual binary yield P , a'' , e , i , T_0 , ω , and Ω : the orbital period, semi-major axis in arcseconds, eccentricity, inclination, time of periastron passage, longitude of periastron, and longitude of the ascending node, respectively.² When the distance to the binary is known, as it is with Gl569, the semi-major axis, in physical units, and period determine the total mass of the binary via Kepler's Third Law (see Chapter 1). Figure 4.5 shows the apparent orbit derived from the astrometry reported by Lane et al. (2001), Zapatero Osorio et al. (2004), and Table 4.4. The orbital parameters were calculated using procedures written by Schaefer (2004) and described in Schaefer et al. (2003). Table 4.5 contains the updated orbital elements; they are in excellent agreement with those published by Zapatero Osorio et al. (2004). The measurements in Table 4.4 extend the time over which the orbital motion of the Gl569B binary has

² ω and Ω determined for a visual binary are degenerate by 180° ; the ambiguity is removed by observing the system as a spectroscopic binary.

been monitored from 0.85 to 2.3 orbital periods; as expected, their main effect is to improve the precision of P and T_0 . The total mass of the Ba–Bb system that follows from these values is $M_{\text{tot}} = 0.125 \pm 0.007 M_{\odot}$. This value is consistent with that determined by Zapatero Osorio et al. (2004) but the uncertainty is larger because it includes the uncertainty of the *Hipparcos* distance measurement while theirs does not.

4.4.2 Velocities of the Gl569B Spectroscopic Binary

Non-AO NIRSPEC spectra of Gl569B do not angularly resolve Ba and Bb. A TODCOR analysis (see 2.1) of blended spectra of Gl569B using the suite of templates in Table 2.1 and Figures 2.5 and 2.6, showed that the template spectrum of Gl644C (M7) provided a high correlation. The analysis also showed that precise measurement of the component velocities would be difficult because the radial velocity difference between Ba and Bb was only a few km s^{-1} , the spectra of the components were similar and complex, and the spectral lines of Ba appeared to be significantly broadened. Under these conditions, the template spectra in Table 2.1 were inadequate for solving the two-dimensional cross-correlation. To obtain a higher velocity precision I needed to remove any mismatch between the target and template spectra; this required using the angularly resolved spectra of Ba and Bb themselves as templates. To this end, we used NIRSPEC with AO to obtain angularly resolved spectra of Ba and Bb on 2003 April 20 and 2004 May 24. The small angular separation between the components necessitated care in the extraction of their spectra to minimize the contamination of Ba by Bb and

visa versa. Figure 4.6 illustrates the procedure. The lower panel shows a sample profile of the two-dimensional spectrum in the cross-dispersion direction from 2004 May 24, obtained by median filtering a REDSPEC rectified image along the dispersion direction; the AO plate scale is $0''.0182 \text{ pixel}^{-1}$. There is significant blending in the region between Ba and Bb. I modeled the profile as the sum of two Gaussians of equal width with separation fixed to that of Ba and Bb at the time of the observation. The upper panel of Figure 4.6 shows the extraction widths, denoted by the vertical lines and hashed regions, chosen to avoid the central region where the profiles are blended. The FWHM of the Gaussians in Figure 4.6 is about twice the diffraction limit at $1.6 \mu\text{m}$. The quality of the seeing and the AO correction varied throughout the observations; the PSF in the profile shown was especially broad. I varied the extraction widths to suit each integration. Figure 4.6 shows that even in this case the selected regions suffer little contamination and I believe, therefore, that this approach produced individual target spectra with very little cross-contamination, and hence templates useful for analysis of the blended spectra.

To determine the radial velocity of Ba in orders 48 and 49 on 2003 April 20 and 2004 May 24, I cross-correlated spectra of Ba with the Gl644C template, and found the highest correlation for $\nu_{\text{rot}} \sin i = 25 \text{ km s}^{-1}$, if I interpret the line broadening as attributable to rotation. For Bb, again using the Gl644C template, the highest correlation was obtained with $\nu_{\text{rot}} \sin i = 10 \text{ km s}^{-1}$. The measured radial velocities of Ba and Bb in the two orders on the two dates differed by the measurement error. To use the individual Ba and Bb spectra as templates to analyze

the blended, non-AO Gl569B component spectra, I averaged the measured velocities in orders 48 and 49; these values appear in the top section of Table 4.6.

Figure 4.7 shows, in the heliocentric reference frame, the 2003 April 20 and 2004 May 24 AO resolved spectra of Gl569Ba and Bb in orders 48 and 49 and, for comparison, a non-AO spectrum of Gl569B measured on 2005 February 22. The spectral range displayed for order 48 is less than that for order 49 because I did not analyze the $\sim 0.007 \mu\text{m}$ wide section shortward of $1.585 \mu\text{m}$ that suffers from terrestrial CO_2 absorption (see 4.2.1). It is evident that the lines in the spectrum of Ba are more broadened than those of Bb. Except for the effects of broadening, the spectral features in Ba and Bb appear identical suggesting that the spectral types must be very similar. These results are consistent with the finding of Zapatero Osorio et al. (2004) that, in their high-resolution, angularly resolved *J*-band spectra, also obtained using NIRSPEC, Ba and Bb appeared as spectral type M8.5 and M9, with significant broadening characterized by $v_{\text{rot}} \sin i \sim 37 \text{ km s}^{-1}$ and 30 km s^{-1} , respectively.

I analyzed the non-AO spectra with TODCOR twice using the two different AO-resolved templates for Ba and Bb from the two different NIRSPEC with AO runs. The measured radial velocities are in Table 4.6. The night sky OH emission lines in order 48 are weaker than those in order 49. On 2002 December 22 and 2003 June 14, the integration times were not long enough to expose the OH lines sufficiently to determine a reliable order 48 dispersion solution and so I do not list order 48 velocities for those dates. The difference in velocities derived on a given date using the two sets of AO-resolved templates is an empirical measure

of the uncertainty. Thus, for each order, I considered the differences

$$\Delta_{\text{Ba},i} = V_{\text{Ba},i}(\text{03 Apr}) - V_{\text{Ba},i}(\text{04 May})$$

in which the $V_{\text{Ba},i}$ terms are the radial velocities of Ba measured on the i th occasion using the AO templates obtained in 2003 April and 2004 May (Table 4.6). The same procedure was applied to the velocities of Bb. The distribution of the 28 differences is centered at $0.1 \pm 1.7 \text{ km s}^{-1}$, indicating that there is no systematic velocity offset in either set of templates. The standard deviations for the $\Delta_{\text{Ba},i}$ and $\Delta_{\text{Bb},i}$ are 1.8 and 1.4 km s^{-1} , respectively; these values are listed in Table 4.6 as the velocity uncertainties of the Ba and Bb components. I attribute the larger uncertainty associated with the measurements for Ba to the greater velocity width of its spectral lines.

4.4.3 Dynamical Masses of the Components

Velocity measurements of a double-lined spectroscopic binary yield P , e , T_0 , ω , $a \sin i$, in physical units, and the velocity semi-amplitudes of the primary and secondary, K_{Ba} and K_{Bb} . These are related to the mass ratio, $q = M_{\text{Bb}}/M_{\text{Ba}}$, a , and a_{Ba} and a_{Bb} , the semi-major axes of the primary and secondary by $q = K_{\text{Ba}}/K_{\text{Bb}}$ and $a \sin i = (a_{\text{Ba}} + a_{\text{Bb}}) \sin i$. Here $a_{\text{Ba,Bb}} \sin i$ is given by

$$a_{\text{Ba,Bb}} \sin i = 0.01375 K_{\text{Ba,Bb}} P (1 - e^2)^{1/2}$$

where a is in gigameters, K in km s^{-1} , and P in days (Heintz, 1978).

Here, P , e , i , a'' and T_0 are already known to high precision from the astrometric observations of Gl569B (Table 4.5). In combination with the *Hipparcos*

distance of Gl569A, a is known in physical units. Gl569B was solved as an spectroscopic binary using a χ^2 analysis for possible velocity solutions to the measurements in Table 4.6. The parameters from the astrometric orbit were fixed at their known values. In this manner, I derived K_{Ba} , K_{Bb} , and γ , the center-of-mass velocity, for the minimum value of χ^2 . I did this twice, treating separately the velocities measured with each set of AO templates. The minimum reduced χ^2 is ~ 1.1 for both solutions. The results for the velocity semi-amplitude of Bb and the center-of-mass velocity are in excellent agreement with each other, but the results for the velocity semi-amplitude of Ba are not. Using the 2003 April 20 templates,

$$K_{Ba} = 2.90 \pm 0.50 \text{ km s}^{-1}$$

$$K_{Bb} = 5.34 \pm 0.50 \text{ km s}^{-1}$$

$$\gamma = -8.47 \pm 0.30 \text{ km s}^{-1}$$

and using the 2004 May 24 templates,

$$K_{Ba} = 4.30 \pm 0.70 \text{ km s}^{-1}$$

$$K_{Bb} = 5.30 \pm 0.50 \text{ km s}^{-1}$$

$$\gamma = -8.50 \pm 0.30 \text{ km s}^{-1}.$$

I attribute the large difference of the two K_{Ba} values to the large velocity width of the Ba spectrum, as also manifested (see 4.4.2) in the scatter of the $\Delta_{Ba,i}$, larger than that of the $\Delta_{Bb,i}$. Because $K_{Bb} = 5.3 \pm 0.5 \text{ km s}^{-1}$ is well-determined, I analyzed Gl569B as a single-lined system on the basis of the Bb data. Figure 4.8 shows the velocity versus phase data for the 2003 April 20 and 2004 May 24 templates. The velocities of the secondary are fitted with K_{Bb} and γ as given above. The mass function, $f(M)$, of the secondary is,

$$f(M) = \frac{(M_{\text{Ba}} \sin i)^3}{(M_{\text{Ba}} + M_{\text{Bb}})^2} \quad (4.1)$$

$$= 1.036 \times 10^{-7} K_{\text{Bb}}^3 P(1 - e^2)^{3/2} M_{\odot} \quad (4.2)$$

with K_{Bb} in km s^{-1} and P in days (adapted from Heintz, 1978). Using values for P , e , i , and $M_{\text{Ba}} + M_{\text{Bb}} = M_{\text{tot}}$ from Table 4.5, and $K_{\text{Bb}} = 5.3 \pm 0.5 \text{ km s}^{-1}$, I derive that $M_{\text{Ba}} = 0.105 \pm 0.011 M_{\odot}$ and, by subtracting from the total mass, $M_{\text{Bb}} = 0.020 \pm 0.013 M_{\odot}$.

The value of M_{Ba} cannot be taken at face value given the similarity of the Ba and Bb spectra (Figure 4.7) and their flux ratio ~ 0.6 (Table 4.4). A promising explanation is that Ba itself is a close, angularly unresolved binary, and that Gl569B consists of three brown dwarfs, two at Ba and one at Bb as previously suggested by Martín et al. (2000) and Kenworthy et al. (2001). The masses of the Ba brown dwarfs are probably $\sim 0.045 - 0.050 M_{\odot}$ each, and that of Bb, $\sim 0.020 - 0.040 M_{\odot}$. This explanation would account for the observed facts: that Ba is about twice as bright as Bb at H , that the total mass is $\sim 0.12 M_{\odot}$, and that the spectra of Ba and Bb appear identical except for the greater line width of Ba. The greater line width of Ba could be attributable either to rotational broadening, which could disguise the presence of an additional component, or some combination of line broadening and Ba orbital motion. If the candidate binary possesses an orbital inclination distinct from and larger than that of the Ba – Bb system, the confusion between broadened lines and velocity shifts would be accentuated, particularly for objects of the similar spectral type. More AO-resolved, high resolution spectra of Ba are required to distinguish among these possibilities.

Figure 4.9 shows Gl569Bb on a mass-luminosity (at H -band) diagram; if its mass is at the 1σ upper bound, $0.033 M_{\odot}$, the isochrones indicate a ~ 100 Myr age, consistent with that of Gl569A. The individual H magnitudes and masses of the brown dwarfs proposed to comprise GL 569Ba remain unknown. If the masses are $\sim 0.045 M_{\odot}$, with M_H a few tenths brighter than 11 mag, the isochrones indicate an age $\gtrsim 100$ Myr. The uncertainties are sufficiently large that it is unclear whether these mass estimates are in conflict.

The derived center-of-mass velocity of Ba – Bb, $\gamma = -8.50 \pm 0.3 \text{ km s}^{-1}$, is well determined. It differs, however, by 3 km s^{-1} from the value reported by Zapatero Osorio et al. (2004), $-11.5 \pm 0.5 \text{ km s}^{-1}$. They measured the Doppler shift of the pressure broadened, nearly saturated K I doublet in their J -band spectra using the observed and laboratory wavelengths, while I referenced to the stellar radial velocities of the spectral type templates. I believe that my value is representative of the actual value because it relies on all of the lines in the observed spectra and avoids the complications of the K I lines. Moreover, for M spectral types, contamination by Mg I at $1.24369 \mu\text{m}$ and particularly by Cr I at $1.25253 \mu\text{m}$ for later types can shift the line centers of the K I doublet at $1.24356 \mu\text{m}$ and $1.25255 \mu\text{m}$. That my measured center-of-mass velocity differs from the radial velocity of Gl569A by only $0.8 \pm 0.9 \text{ km s}^{-1}$ also suggests that it is close to the actual value. The $\sim 3 \text{ km s}^{-1}$ difference between this value and that of Zapatero Osorio et al. (2004) affects only their absolute radial velocities. The differences in the radial velocities of Ba and Bb that they measured (their Table 4 and Figure 8) agree well with the differences derived from the values in Table 4.6 and shown in Figure 4.10.

4.5 Discussion

4.5.1 The Gl569 Quadruple?

This work suggests that Gl569 may be a quadruple consisting of an M2.5 V star (Gl569A) accompanied by three nearly equal mass brown dwarfs and distributed as follows:

1. The wide binary, Gl569A – Gl569B, at separation $\sim 5''$ (~ 50 AU) with total mass $(0.35 \pm 0.03) + (0.125 \pm 0.007) = 0.48 \pm 0.03 M_{\odot}$. If oriented face-on, its orbital period is ~ 500 yrs.

2. The binary Gl569Ba – Gl569Bb which has semimajor axis 90 mas (0.89 AU), period 864 days, and total mass $0.125 \pm 0.007 M_{\odot}$. Bb is a single brown dwarf with mass $0.020 \pm 0.013 M_{\odot}$.

3. Ba is an unresolved candidate brown dwarf binary with a total mass of $0.105 \pm 0.011 M_{\odot}$.

I designate the two components of Ba, the inner binary, as Baa and Bab, and consider the limits that can be placed on their orbit empirically by the spectroscopic and imaging observations, and theoretically by the requirement that Ba and Bb form a stable triple. I used the AO resolved order 49 Gl569Bb spectra from 2003 April 20 and 2004 May 24 to model Gl569Ba as two equal brightness brown dwarfs of late M spectral type, rotationally broadened to 10 km s^{-1} , and with known velocity separation. Analysis with TODCOR, using the templates Gl644C and Gl406, showed that I could reliably recover the individual brown

dwarf spectra in the models with a velocity separation of 5 km s^{-1} or larger. I measured no significant velocity separation when carrying out the same analysis on the actual G1569Ba spectra, and conclude that if the Baa and Bab components are rotationally broadened to $\sim 10 \text{ km s}^{-1}$ then their velocity separation was $\leq 5 \text{ km s}^{-1}$ at the times of the observations. With $M_{\text{tot}} = 0.105 M_{\odot}$, this implies that the semimajor axis of the inner binary satisfies $a_{\text{inner}} \gtrsim 3.8 \sin^2 i_{\text{inner}} \text{ AU}$, where i_{inner} is the inclination of the inner binary.

The FWHM of the H -band PSF was 41 mas in the NIRC2 images obtained on 2005 February 25. I analyzed images of model binaries with equal brightness components convolved with the PSF and with the same signal-to-noise as the H -band image in Figure 4.4, and was able to identify the presence of two components at separations as small as ~ 10 mas. The actual situation is complicated by contamination from the third component, Bb, at apparent separation ~ 85 mas (Table 4.4), $2 \times$ FWHM of the PSF. It is apparent in Figure 4.4 that the broad wings of the PSF extend from Bb to Ba. I estimate that Baa and Bab would have to lie at apparent separation $\gtrsim 20$ mas to be recognizable with NIRC2. This limit, combined with that from the spectroscopic observations, restricts i_{inner} to the range $\pm 13.6^\circ$.

Theoretical study of the stability of triples has an extensive literature and continues to be an interesting area of research as new environments are identified (e.g., the formation of planets in stellar binaries; Holman & Wiegert 1999) and the meaning of “stability” is sharpened (e.g., Ford et al. 2000). Eggleton & Kiseleva (1995) present an empirical stability criterion in terms of Y^{min} , the ratio of

the periastron distance of the outer binary to the apastron distance of the inner binary,

$$Y^{\min} = \frac{a_{\text{outer}}(1 - e_{\text{outer}})}{a_{\text{inner}}(1 + e_{\text{inner}})}$$

When values of Y^{\min} larger than a critical value, Y_0^{\min} , are realized, the triple is stable. This criterion is applicable to triples with various inclinations, eccentricities, and relative phases of the inner and outer binaries. For a triple with equal mass components, $Y_0^{\min} \sim 5$ (see Eggleton & Kiseleva, 1995, eq. 2). With $a_{\text{outer}} = 0.90$ AU and $e_{\text{outer}} = 0.31$ (Table 4.5), $a_{\text{inner}}(1 + e_{\text{inner}}) = 0.13$ AU; $a_{\text{inner}} = 0.13$ AU if $e_{\text{inner}} = 0$, and 0.07 AU if $e_{\text{inner}} = 0.9$. In the latter case, the apastron of the inner binary is 0.13 AU. I conclude that the largest value of a_{inner} for stability, 0.13 AU, is consistent with the observational limits if i_{inner} lies in the range $\pm 11^\circ$.

4.5.2 The Lithium Test

The Li spectral line at 6708 Å is a sensitive mass and age indicator because brown dwarfs with mass $> 0.06 M_\odot$ destroy their Li within a few hundred Myr (Magazzu et al., 1993; Chabrier & Baraffe, 2000). The masses estimated for Baa, Bab, and Bb are near this boundary. In spectroscopic observations that did not angularly resolve the Gl569B system, Magazzu et al. (1993) did not detect the Li line, suggesting that the brown dwarf masses are greater than the values inferred here. However, detecting Li in Gl569B may be complicated by the large line widths (see 4.4.2) and by the possible triple nature of the system.

4.6 Summary and Suggestions for Future Work

The previous suggestions that Ba could be a binary brown dwarf were based on the fact that Ba is ~ 1.6 times brighter than Bb in the near infrared and that the colors of the two are similar (Martín et al., 2000; Kenworthy et al., 2001). The work presented here confirms these observations and strengthens the case for the binary nature of Ba in three respects: (a) the dynamical mass of Ba is $0.105 \pm 0.011 M_{\odot}$, and Ba cannot be a single star of this mass; (b) Ba and Bb have similar spectral features, indicating that Ba and Bb contain similar brown dwarfs; and (c) the line width of Ba, $\sim 25 \text{ km s}^{-1}$, significantly larger than that of Bb, $\sim 10 \text{ km s}^{-1}$, has a natural explanation if Ba harbors two brown dwarfs. These arguments and the total mass of the Gl569B system, $M_{\text{tot}} = 0.125 \pm 0.007 M_{\odot}$, also suggest that the masses of the Baa, Bab, and Bb components are approximately equal and in the range $0.04 - 0.05 M_{\odot}$.

The location of Gl569A with respect to theoretical isochrones and in the Pleiades color-magnitude diagram is consistent with an age of ~ 100 Myr. Previous estimates, using photometry of Gl569Ba and Gl569Bb, suggested the age was ~ 300 Myr (Lane et al., 2001; Zapatero Osorio et al., 2004). If, however, Ba is a binary then the location of Bb with respect to theoretical isochrones (and also of Baa and Bab if they have approximately equal mass) is consistent with an age of ~ 100 Myr.

The Gl569 quadruple is well suited to improve our understanding of objects at the low mass end of the IMF. The following observations could confirm and advance beyond the results presented here:

1. Detection of the Li line in the spectra of both Ba and Bb would confirm the mass of Bb and indicate that Ba must be composed of two brown dwarfs. The spectroscopic measurement should angularly resolve Ba and Bb to avoid the complications of interpreting the complex blended spectrum of three brown dwarfs. This would require AO-assisted spectroscopic observations in the visible, a capability not yet available.

2. Additional high angular resolution infrared spectroscopy of Bb can improve the precision of the velocity semiamplitude K_{Bb} , and hence of M_{Ba} and M_{Bb} .

3. High angular resolution infrared spectroscopy of Ba may distinguish the two brown dwarfs Baa and Bab, and hence determine their orbital parameters as a double-lined spectroscopic binary.

4. At separation ~ 7 mas, the inner binary is resolvable by the present generation of infrared interferometers and is not far below their present sensitivity limits. The visual binary parameters of the inner binary, combined with (3) would determine the individual masses M_{Ba} and M_{Bb} , and reveal whether the orbits in the hierarchical triple are coplanar.

Of the observations suggested, 2 and 3 can be carried out with current facilities. Technological advances are necessary before 1 and 4 are possible.

Bibliography

- Baraffe, I., Chabrier, G., Allard, F., & Hauschildt, P. H. 1998, *A&A*, 337, 403
- Baraffe, I., Chabrier, G., Barman, T. S., Allard, F., & Hauschildt, P. H. 2003, *A&A*, 402, 701
- Chabrier, G. & Baraffe, I. 2000, *ARA&A*, 38, 337
- Eggleton, P. & Kiseleva, L. 1995, *ApJ*, 455, 640
- Ford, E. B., Kozinsky, B., & Rasio, F. A. 2000, *ApJ*, 535, 385
- Forrest, W. J., Shure, M., & Skrutskie, M. F. 1988, *ApJ*, 330, L119
- Gorlova, N. I., Meyer, M. R., Rieke, G. H., & Liebert, J. 2003, *ApJ*, 593, 1074
- Heintz, W. D. 1978, *Double Stars* (Revised ed. Dordrecht; Reidel)
- Henry, T. J. & Kirkpatrick, J. D. 1990, *ApJ*, 354, L29
- Holman, M. J. & Wiegert, P. A. 1999, *AJ*, 117, 621
- Kenworthy, M., Hofmann, K.-H., Close, L., Hinz, P., Mamajek, E., Schertl, D., Weigelt, G., Angel, R., Balega, Y. Y., Hinz, J., & Rieke, G. 2001, *ApJ*, 554, L67
- Lane, B. F., Zapatero Osorio, M. R., Britton, M. C., Martín, E. L., & Kulkarni, S. R. 2001, *ApJ*, 560, 390
- Luhman, K. L., Stauffer, J. R., & Mamajek, E. E. 2005, *ApJ*, 628, L69
- Magazzu, A., Martin, E. L., & Rebolo, R. 1993, *ApJ*, 404, L17
- Martín, E. L., Koresko, C. D., Kulkarni, S. R., Lane, B. F., & Wizinowich, P. L. 2000, *ApJ*, 529, L37
- Meynet, G., Mermilliod, J.-C., & Maeder, A. 1993, *A&AS*, 98, 477

Prato, L., Simon, M., Mazeh, T., McLean, I. S., Norman, D., & Zucker, S. 2002, ApJ, 569, 863

Schaefer, G. H. 2004, Ph.D. Thesis

Schaefer, G. H., Simon, M., Nelan, E., & Holfeltz, S. T. 2003, AJ, 126, 1971

Simon, M., Bender, C., & Prato, L. 2006, ApJ, 644, 1183

Stauffer, J. R., Schultz, G., & Kirkpatrick, J. D. 1998, ApJ, 499, L199

Zapatero Osorio, M. R., Lane, B. F., Pavlenko, Y., Martín, E. L., Britton, M., & Kulkarni, S. R. 2004, ApJ, 615, 958

Table 4.1. Log of G1569 Observations

UT Date	MJD	Instrument	Mode	Targets
2002 Jul 18	52473.3	NIRSPEC	non-AO	GL569B
2002 Dec 22.....	52630.7	NIRSPEC	non-AO	GL569B
2003 Mar 25	52723.5	NIRSPEC	non-AO	GL569B
2003 Apr 20	52749.4	NIRSPEC	AO	GL569A,GL569Bab
2003 Jun 14	52804.2	NIRSPEC	non-AO	GL569A,GL569B
2004 Jan 26	53030.6	NIRSPEC	non-AO	GL569B
2004 Apr 29	53124.4	NIRSPEC	non-AO	GL569B
2004 May 24	53149.3	NIRSPEC	AO	GL569Bab
2004 May 25	53150.3	NIRSPEC	AO	GL569A
2004 Dec 24.....	53363.7	NIRC2	AO	GL569Bab
2004 Dec 26.....	53365.7	NIRSPEC	non-AO	GL569B
2005 Feb 22.....	53423.5	NIRSPEC	non-AO	GL569B
2005 Feb 25.....	53426.5	NIRC2	AO	GL569A,GL569Bab

Table 4.2. Astrometry of G1569AB

Date	R.A. \times cos (Decl.) (arcsec)	Decl. (arcsec)	Reference
1985.6.....	1.52 ± 0.15	4.84 ± 0.15	Forrest et al. (1988)
1999.7.....	2.11 ± 0.08	4.53 ± 0.04	Martín et al. (2000)
2001.1.....	2.45 ± 0.22	4.23 ± 0.13	Lane et al. (2001)
2005.2.....	2.72 ± 0.14	4.18 ± 0.21	This work

Table 4.3. Radial Velocity Measurements of Gl569A

MJD	V_{rad} (km s^{-1})
52749.4	-7.1 ± 1.0
52804.3	-8.1 ± 1.0
53150.3	-7.8 ± 1.0
Average	-7.7 ± 0.6

Table 4.4. Photometry and Astrometry of Gl569B

MJD	Exp. (s)	H_{Ba}	H_{Bb}	K_{Ba}	K_{Bb}	H_{Bb}/H_{Ba}	K_{Bb}/K_{Ba}	Sep. (")	P. A. (°)
53363.7...	100	0.61 ± 0.03	...	0.0885 ± 0.0048	111.3 ± 1.2
53426.5...	22	10.43 ± 0.04	11.04 ± 0.05	9.86 ± 0.05	10.39 ± 0.06	0.57 ± 0.04	0.61 ± 0.04	0.0798 ± 0.0029	133.7 ± 0.7

Table 4.5. Orbital Parameters of Gl569Bab

Parameter	Visual Binary Orbit	
	Zapatero Osorio et al. (2004)	This Work
P (days)	876 ± 9	863.7 ± 4.2
T_0 (MJD, days)	$51,822 \pm 3$	$51,820.9 \pm 2.6$
e	0.32 ± 0.01	0.312 ± 0.007
a (mas)		90.4 ± 0.7
a (AU)	0.90 ± 0.01^a	0.89 ± 0.02^b
i (deg)	34 ± 2	32.4 ± 1.3
ω (deg)	257 ± 2	256.7 ± 1.7
Ω (deg)	321.5 ± 2.0	321.3 ± 2.2
$M_{\text{tot}} (M_{\odot})$	0.125 ± 0.005^a	0.125 ± 0.007^b

^aDoes not include 1.6% parallax uncertainty

^bDoes include 1.6% parallax uncertainty

Table 4.6. Radial Velocity Measurements of Gl569Bab

MJD	Phase	$V_{\text{rad}}(\text{km s}^{-1})$			
		Gl569Ba		Gl569Bb	
		Order 49	Order 48	Order 49	Order 48
Gl644C Templates					
52749.4.....	0.072	-7.92±0.90		-9.98±0.90	
53149.3.....	0.535	-8.50±0.90		-8.38±0.90	
April 20, 2003 Templates					
52473.3.....	0.753	-10.89±1.80	-11.60±1.80	-4.71±1.40	-3.19±1.40
52630.7.....	0.935	-11.60±1.80	...	-3.65±1.40	...
52723.5.....	0.042	-9.46±1.80	-7.12±1.80	-8.07±1.40	-7.74±1.40
52804.2.....	0.136	-7.21±1.80	...	-14.15±1.40	...
53030.6.....	0.397	-7.52±1.80	-4.92±1.80	-12.72±1.40	-11.74±1.40
53124.4.....	0.506	-9.07±1.80	-8.54±1.80	-9.56±1.40	-7.29±1.40
53365.7.....	0.785	-10.62±1.80	-12.31±1.80	-4.98±1.40	-3.09±1.40
53423.5.....	0.852	-10.75±1.80	-11.71±1.80	-3.99±1.40	-1.98±1.40
May 24, 2004 Templates					
52473.3.....	0.753	-12.30±1.80	-10.93±1.80	-4.57±1.40	-3.38±1.40
52630.7.....	0.935	-12.12±1.80	...	-3.96±1.40	...
52723.5.....	0.042	-6.92±1.80	-4.54±1.80	-10.28±1.40	-9.98±1.40
52804.2.....	0.136	-6.29±1.80	...	-13.21±1.40	...
53030.6.....	0.397	-5.42±1.80	-4.49±1.80	-13.03±1.40	-11.28±1.40
53124.4.....	0.506	-6.96±1.80	-5.34±1.80	-11.64±1.40	-11.14±1.40
53365.7.....	0.785	-12.90±1.80	-12.66±1.80	-4.40±1.40	-3.75±1.40
53423.5.....	0.852	-12.76±1.80	-11.82±1.80	-3.41±1.40	-2.70±1.40

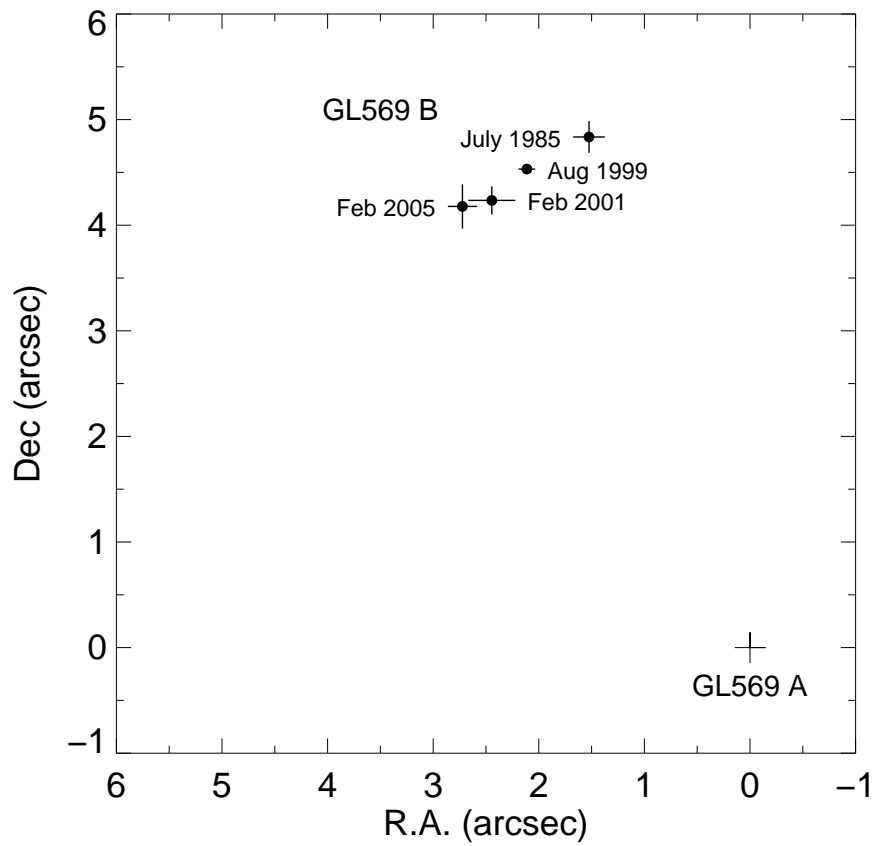


Figure 4.1 The position of GL569B with respect to A using the 2005 February 25 NIRC2 measurement and the earlier measurements listed in Table 4.2. A and B form a common proper motion system (see 4.3); the figure shows orbital motion of B with respect to A. North is up and east is to the left.

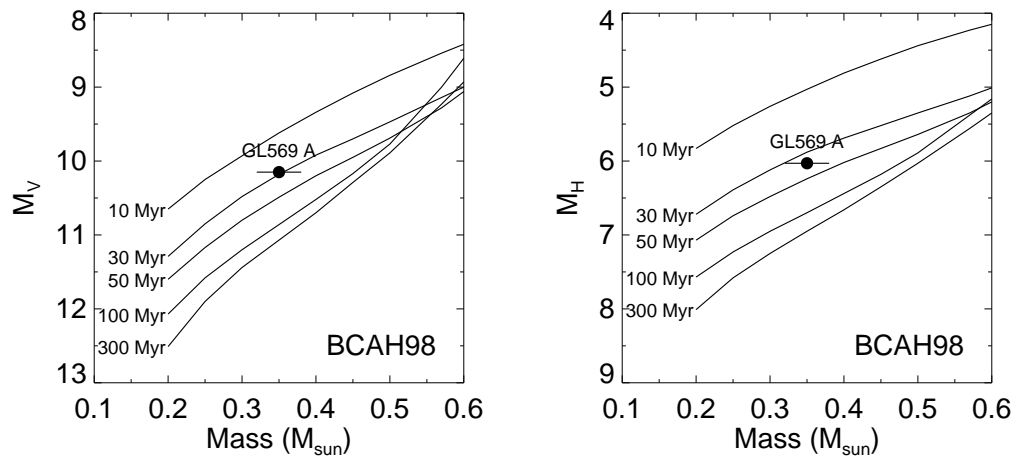


Figure 4.2 Absolute V and H magnitudes and mass of GL569A compared to theoretical isochrones calculated by Baraffe et al. (1998).

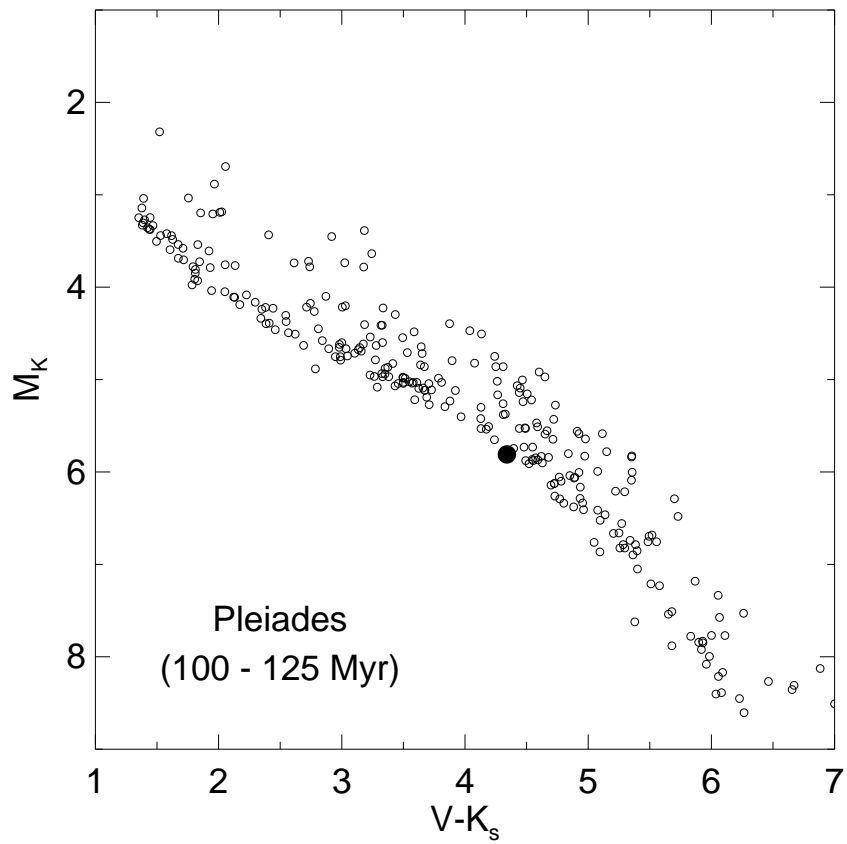


Figure 4.3 Absolute K mag and $V-K$ color of Gl569A (filled circle) on a color-magnitude diagram of the Pleiades. The Pleiades data is the same as in Luhman et al. (2005), Figure 1, and is for an adopted extinction $A_V = 0.12$ mag and distance 133 pc for the Pleiades.

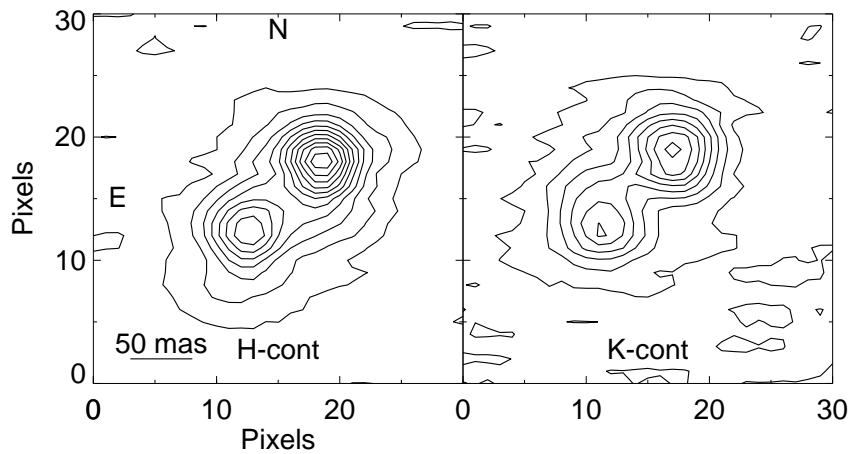


Figure 4.4 NIRC2 adaptive optics images of Gl569Ba and Bb at H and K obtained on 2005 February 25. North is up and east is to the left. The images show a subsection of the frame; Gl569A was imaged in the same field, but is not shown. The first contour represents 1000 counts, $\sim 5\sigma$ over the background noise, and each subsequent contour is an additional 1000 counts. Ba is located northwest of Bb and is clearly the brighter component; the Bb/Ba flux ratios are 0.57 ± 0.04 and 0.61 ± 0.04 in H and K respectively.

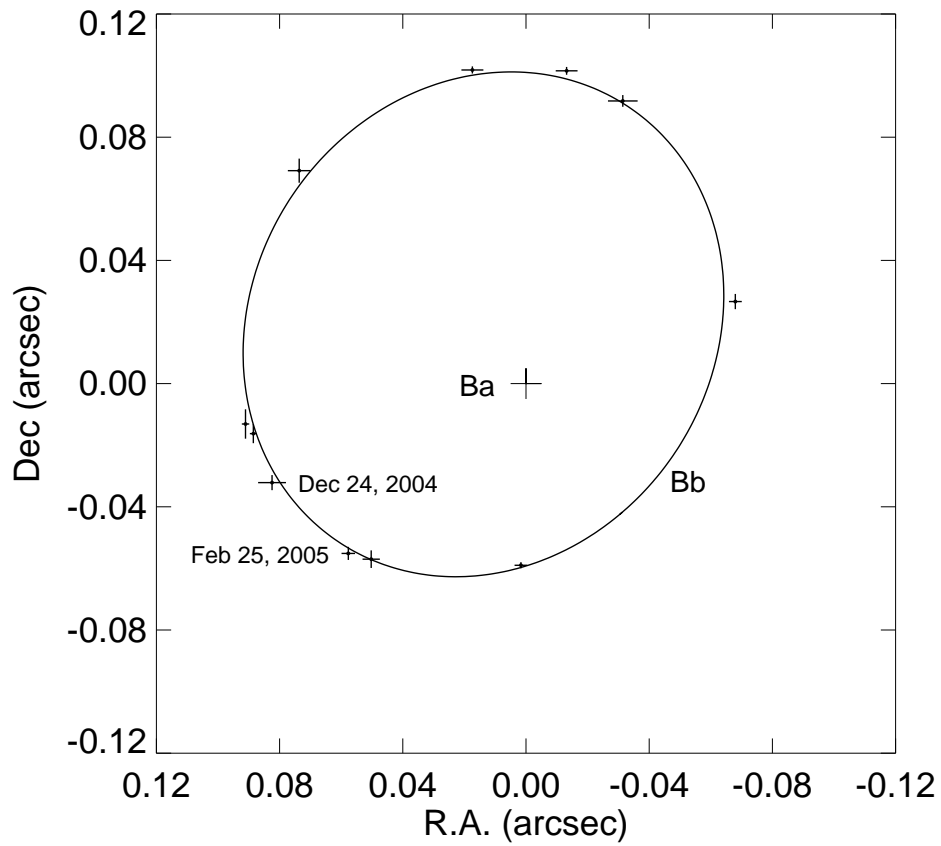


Figure 4.5 The astrometric orbit of Gl569Bb with respect to Ba at the coordinate origin, using the measurements from 2004 December 24 and 2005 February 25 together with the earlier measurements given in Zapatero Osorio et al. (2004). The best fit orbit corresponds to the updated parameters in Table 4.5.

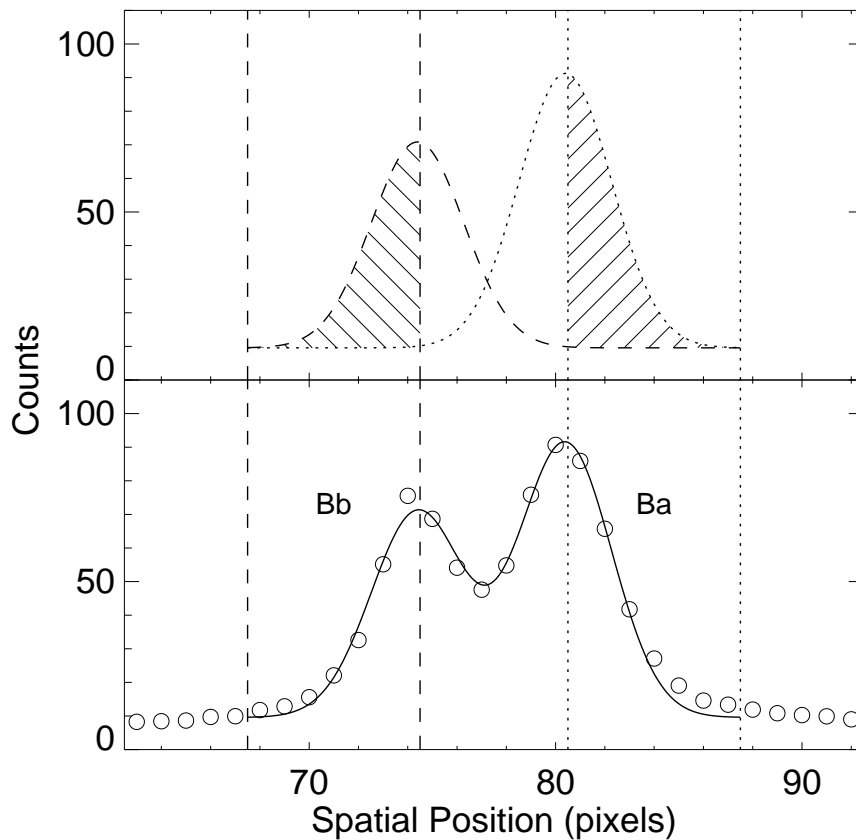


Figure 4.6 A sample profile in the cross-dispersion direction of the AO angularly resolved order 49 G1569Ba and Bb two-dimensional spectrum from 2004 May 24. The open circles (bottom panel) show the measured spatial profile of the resolved spectra; the solid line is a least squares fit of two Gaussians with equal widths (see text). The dotted and dashed curves (top panel) are the individual Gaussian profiles. The vertical lines and hashed areas indicate the spatial regions used to extract each spectrum.

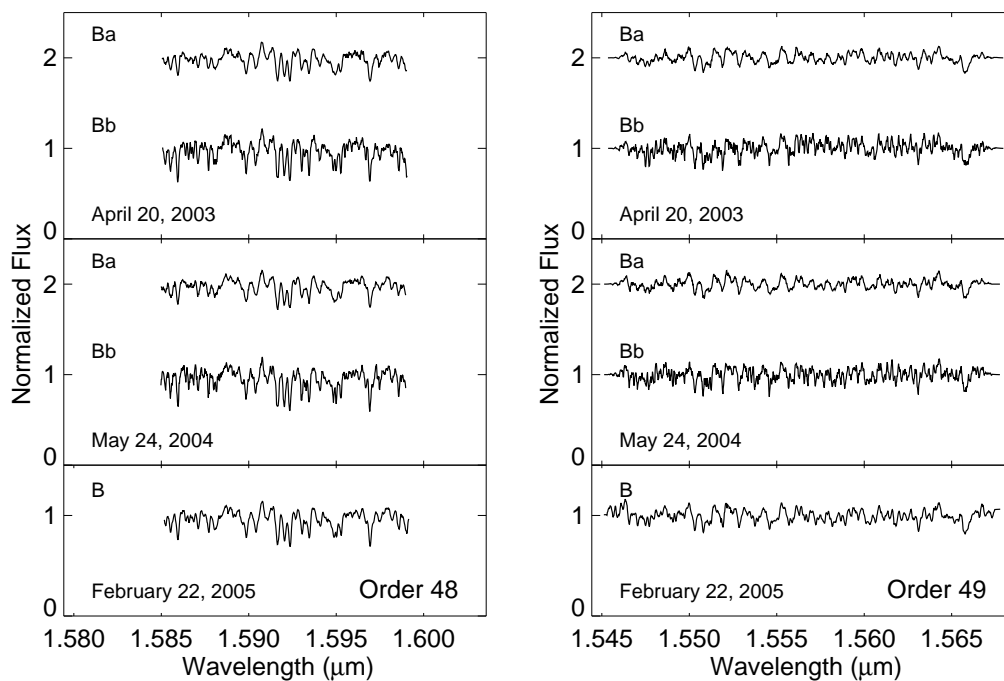


Figure 4.7 Angularly resolved spectra of Gl569Ba and Bb measured on 2003 April 23 and 2004 May 24, compared with a spectrum measured on 2005 February 22 in which Ba and Bb are unresolved. NIRSPEC spectral orders 48 (left) and 49 (right) are shown. The wavelength span of the order 48 spectra is about 2/3 that of the order 49 spectra because the $\sim 0.007 \mu\text{m}$ wide section shortward of $1.585 \mu\text{m}$ is contaminated by a terrestrial CO_2 band and not shown. The spectra are normalized to 1 in the continuum and are plotted on a 0 to 1 flux scale with the Ba spectra in the top two panels offset by +1 in flux.

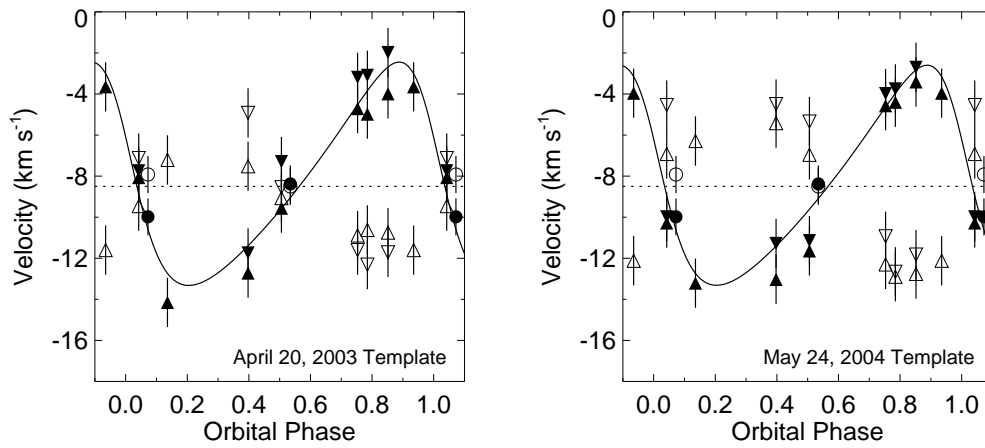


Figure 4.8 Velocity versus orbital phase measurements for Gl569Ba (*open triangles*) and Bb (*filled triangles*) using the 2003 April 20 templates (*left*) and 2004 May 24 templates (*right*). Order 48 and 49 data are plotted as downward and upward pointing triangles, respectively. The measurements obtained with AO, averaged over orders 48 and 49, are indicated with open (Ba) and filled (Bb) circles. The dashed line is the fitted center-of-mass velocity, -8.5 km s^{-1} , and the solid line is the model fit with $K_{\text{Bb}} = 5.3 \text{ km s}^{-1}$ and P , e , i , and ω given in Table 4.5.

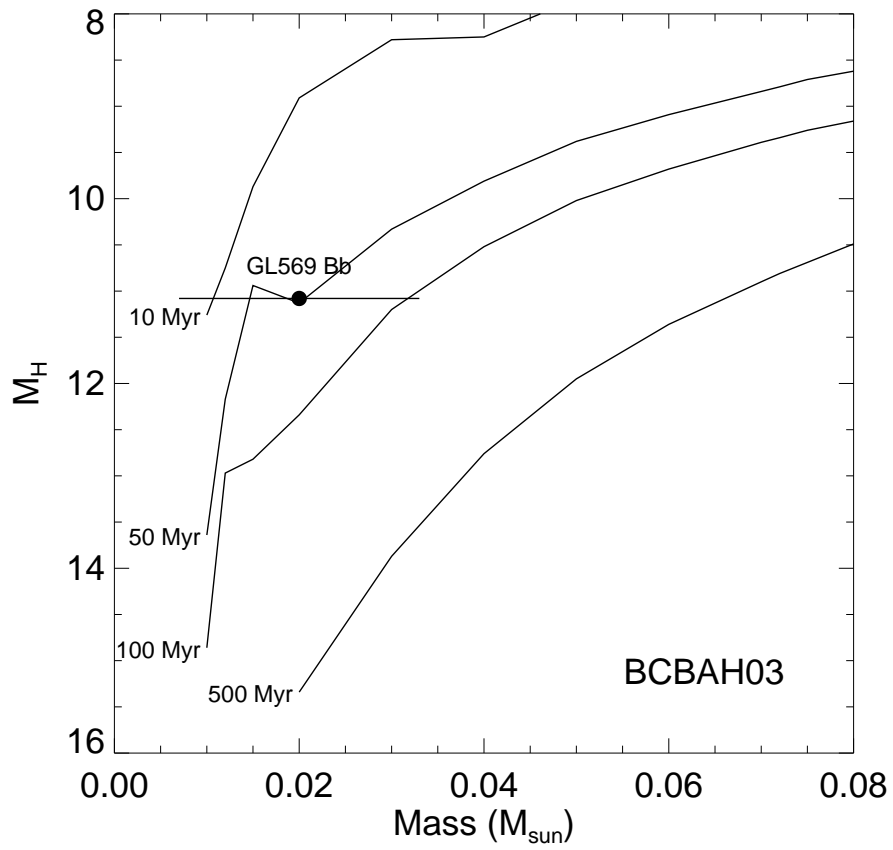


Figure 4.9 GL569Bb with $M_H = 11.08 \pm 0.05$ mag and mass $0.020 \pm 0.013 M_\odot$ compared with theoretical isochrones calculated by Baraffe et al. (2003). The age of Bb is within 1σ of ~ 100 Myr.

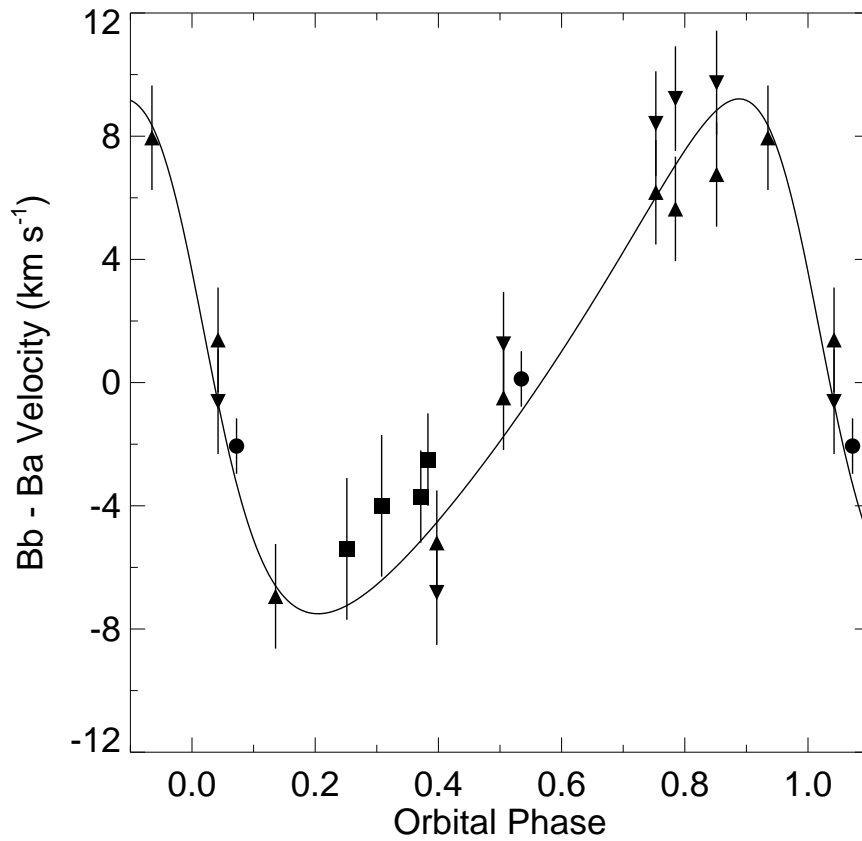


Figure 4.10 The G1569Ba and Bb velocity difference plotted against orbital phase using the measurements in Table 4.6 with the 2003 April 20 templates for order 48 (*downward triangles*), order 49 (*upward triangles*), and AO (*circles*). Our data are consistent with the values (*squares*) reported by Zapatero Osorio et al. (2004).

Chapter 5

An Upper Bound on the 1.6 μm Flux Ratio to the Companion of ρ Coronae Borealis

5.1 Introduction

ρ Coronae Borealis (ρ CrB, HIP 78459), a well-studied G0V star with an estimated mass of $1.0 M_{\odot}$ and an age of 10 Gyr, was among the first stars identified with an extra-solar planet (ESP) candidate (Noyes et al., 1997). If the mass of the companion, M , is small relative to ρ CrB, the system's mass function indicates that $M \sin i = 1.1 M_{\text{Jupiter}}$, where i is the orbital inclination. For a random distribution of orbital plane inclinations, the expectation value of M is $(4/\pi) \times 1.1 M_{\text{Jupiter}}$, justifying the interpretation that ρ CrB's companion is an ESP.

Gatewood et al. (2001) used data from *Hipparcos* and the ground-based Multichannel Astrometric Photometer (Gatewood, 1987) to measure the astrometric signature of the reflex motion of ρ CrB. They derived an astrometric orbit with a semi-major axis of 1.65 ± 0.33 mas and an inclination of $i \sim 0.5^{\circ}$, indicating that

the companion is a late type M dwarf star with mass $0.14 \pm 0.05 M_{\odot}$. In a large sample of ESP candidates, only a few systems seen at low inclinations are expected. It was therefore surprising that, in a companion paper, Han et al. (2001, hereafter HBG) found, by combining *Hipparcos* data with the spectroscopic orbital elements of 30 ESP candidates, that a significant fraction may have small inclinations. The semi-major axes of the orbits that they derived are, however, at the limits of the precision of *Hipparcos* measurements. Pourbaix & Arenou (2001) and Zucker & Mazeh (2001) demonstrated that in these circumstances the small i 's were an artifact of HBG's analysis. Indeed, McGrath et al. (2002) HST astrometric observation of ρ^1 Cnc (55 Cnc), a star estimated by HBG to have a particularly low inclination orbit, placed an upper limit on its reflex motion, confirming that its companion is sub-stellar.

Colleagues and I combined NIRSPEC spectroscopy with a modified cross-correlation analysis to search for the companion to ρ CrB. If the companion has the mass of a late M spectral type main-sequence star, it should lie within the sensitivity limits of the technique (e.g., Mazeh et al., 2003). I describe here our search for the companion in the ρ CrB system by infrared spectroscopy; these results also appear in Bender et al. (2005).

5.2 Observations and Data Reduction

ρ CrB was observed on four occasions in the spring of 2001 with NIRSPEC on the Keck II telescope, with and without AO (see Table 5.1). I extracted the spectra using REDSPEC and determined the dispersion solution using the OH emission

lines of the night sky. Chapter 2.2.1 describes these procedures in more detail.

Application of the infrared spectroscopic technique to the detection of low mass secondaries requires good templates for the primary and the secondary; Chapter 2.3 describes the observations and processing of the NIRSPEC template suite. Prior analyses with these templates (e.g., Prato et al., 2002; Mazeh et al., 2002) used only NIRSPEC order 49 because it is nearly completely free of terrestrial absorption. To reach the low flux levels expected for ρ CrB's companion, however, required increasing the number of stellar spectral lines available, and hence the spectral range of the data. This necessitated using additional spectral orders and dealing with the contamination from terrestrial absorption shown in Figure 2.2. Because orders 50–53 are badly contaminated by a variety of atmospheric species, and order 45 falls off the detector in one nod position (see 2.3), I concentrated on trying to correct atmospheric absorption only in the spectra of orders 46, 47, and 48.

Terrestrial absorption lines are usually removed by dividing the target spectrum by a featureless stellar spectrum observed nearly simultaneously at the same airmass. I took a different approach because I had to correct many template spectra obtained in different observing sessions, without the benefit of simultaneously observed calibrators. At the level of precision necessary for ρ CrB, the CO₂ and CH₄ absorption bands are independent of weather and vary only with airmass. Therefore, M. Simon and L. Prato obtained NIRSPEC spectra of five A0 stars on 2002 July 17, over the range of airmasses of the ρ CrB and template spectra. I removed the Brackett lines by fitting them with Lorentzian pro-

files and used the terrestrial absorption lines in orders 46, 47, and 48 to register each observation on a sub-pixel scale. For each of the terrestrial lines, I fitted the dependence of the absorption on airmass, and was thereby able to interpolate terrestrial absorption spectra at the exact airmasses of the ρ CrB and template spectra. This procedure worked well for order 47 and less well in orders 46 and 48, probably because their telluric lines are deeper and have more complex structure than those in order 47. The residuals in orders 46 and 48 only affect a few percent or less of the free spectral range of these orders so I considered them negligible. Figure 5.1 shows the order 46–49 ρ CrB spectra measured on 2001 June 2, with orders 46, 47, and 48 corrected for telluric absorption.

5.3 The Companion-to-Primary Flux Ratio of ρ Coronae Borealis

The procedure used to search for evidence of ρ CrB’s companion is similar to the two-dimensional cross-correlation analysis used for spectroscopic binaries, which identifies the templates that provide the best matching primary and secondary, the ratio of the secondary and primary fluxes, α , and the radial velocities of the components. The measured amplitude of ρ CrB’s reflex velocity is 67 m s^{-1} (Noyes et al., 1997). If its companion had the $0.14 M_{\odot}$ mass reported by Gatewood et al. (2001), the maximum velocity difference of the primary and secondary would be 0.4 km s^{-1} . This is less than the $\sim 1 \text{ km s}^{-1}$ velocity precision of the cross-correlation technique, so I did not expect to detect a significant ve-

locity difference. To obtain a velocity difference large enough to detect reliably, $> 1 \text{ km s}^{-1}$, would require that the companion have mass $\lesssim 0.05 M_{\odot}$; the flux of such a substellar object blended with a G star would be too small to detect spectroscopically. I therefore regarded the velocity difference of the components as fixed at 0 and focused on measuring the system's flux ratio.

I wrote a routine to model binaries from pairs of templates at prescribed flux ratios, to cross-correlate them with the ρ CrB spectra, and to identify the model most closely matching ρ CrB. With this, I analyzed separately the ρ CrB spectra in orders 46–49 for each of the four observing sessions using a wide selection of templates. The highest correlation values resulted from using HD4614 or Gl160 for the primary template, depending on the particular ρ CrB spectrum, and the late M-type templates for the secondary. Changing the secondary spectral type by a few subclasses resulted in negligible changes in the correlation, and I concluded that I could only discriminate between early- and late-type M star secondaries. Based on this, I averaged the flux ratios resulting from the late-type secondaries Gl406, LHS292, Gl644C, LHS2351, and LHS2065 for each ρ CrB spectrum. These averaged values are my measured flux ratios and are listed in Table 5.2. The arithmetic mean of the values in Table 5.2 is -0.0034 . This small flux ratio, and the large scatter around it, from -0.0260 to 0.0164 , suggest that the observations have not detected the companion. The primary and secondary templates are not likely to match exactly the effective temperature and metallicity of the ρ CrB primary and companion. The fact that the average flux ratio is essentially zero indicates that any such mismatch is not causing a systematic

error.

To interpret the apparent non-detection I must derive an upper bound, at a specified level of significance, on the flux ratio. The conventional approach would be to calculate the mean of the measured flux ratios in Table 5.2, to assume they follow a Gaussian distribution and derive the standard deviation of the mean, and to use this to place confidence limits on an upper bound. The measured flux ratios, however, do not necessarily follow a Gaussian distribution, and the number of measurements, 16, is too few to test the assumption reliably. I chose, therefore, to use the data itself to model a large number of observations, and from these directly measure the probabilities of a detection at a certain flux ratio, independent of underlying statistical assumptions. Chapter 5.4 describes this approach.

5.4 Estimate of the Flux Ratio Upper Bound

5.4.1 Model Binaries

In this section, I describe my estimate of the upper bound on the ratio of the companion flux to that of ρ CrB that follows from the measurements in Table 5.2. My approach began by analyzing sets of model binaries. To ensure the models closely represented the original observations, I used the observed ρ CrB spectra as the basis for the model primaries. I subdivided each observed ρ CrB spectrum at wavelengths where there were no lines, into smaller sections with lengths from 10 to 60 Å. I reassembled these sections in random sequences to

create a set of 500 unique model primaries for each observation, with absorption lines, noise characteristics, and free spectral range identical to the original ρ CrB spectrum. Figure 5.2 shows examples of reassembled model primaries derived from the 2001 January 7 ρ CrB spectra. I used the M7 spectral type star LHS2351 for the secondary in all of the models, and combined it, unmodified, with the randomized primaries at eight flux ratio values, from 0.001 – 0.020, to create the model binary spectra. This provided 128 sets (four observations times four orders times eight flux ratios) of 500 model binaries each, with which to evaluate the measured flux ratios in Table 5.2.

I analyzed the model binaries in the same way as the original ρ CrB spectra (see 5.3). For each set of models, I cut and reassembled a matching set of primary templates from either HD4614 or Gl160, depending on which was used in the corresponding ρ CrB analysis. I restricted the analysis to only the M6.5 spectral type star LHS292 for the secondary template because the correlation value is insensitive to small changes in the secondary spectral type (see 5.3).

The analysis produced 500 “measured” flux ratios for each of the 128 sets of models. For a given set of models, the measured flux ratios scattered around the input value. Figure 5.3 shows two of these distributions from 2001 January 7, order 49, $\alpha = 0.010$, and $\alpha = 0.005$, along with the corresponding measured value of -0.0046 from Table 5.2.

5.4.2 Flux Ratio Upper Bound

From each of the model distributions I used an approach suggested by S. Zucker to determine the probability that the corresponding ρ CrB observation returned a flux ratio as small as the one measured. Consider, for example, the results for 2001 January 7, order 49. If the actual flux ratio were 0.010, the probability that the observation and its analysis produces a flux ratio as small as the one measured, -0.0046 , is given by the number of model binaries that returned flux ratios of equal value or smaller. Figure 5.3*a* shows the model distribution derived for this case; 24 out of 500 models (probability=0.048) produced an α smaller than -0.0046 . If, then, the true α were 0.010, the probability of a measurement producing a value as low as or lower than -0.0046 is unlikely, and I could consider 0.010 an upper bound with 95% confidence ($1 - 0.048 \sim 0.95$). Suppose that instead the true α were smaller, 0.005. In this case, a larger number of models, now 76 out of 500, or 15%, give an α as small as the measured one (Figure 5.3*b*). I would therefore consider 0.005 as an upper bound with only 85% confidence.

For each of the 16 observations that I modeled, I calculated, at the eight input model flux ratios, the probability of measuring a flux ratio as low as or lower than the measured value in Table 5.2. To combine those probability values into one value, I use Fisher's method to combine independent p -values (Fisher, 1932). In this method, one first calculates the product of probabilities. This value, according to Fisher (1932), is distributed in a known way, and I can use its known

distribution to infer the new probability. The product value, k , is

$$k = \prod_{i=0}^{n-1} p_i. \quad (5.1)$$

Fisher (1932) showed that the statistic $F = -2 \ln k$ has a χ^2 distribution with $2n$ degrees of freedom. Following Fisher's recipe¹, I use this known distribution to calculate P , the combined p -value from the 16 probabilities. Figure 5.4 shows P as a function of input flux ratio. The combined probability curve intersects the 99% confidence level at a flux ratio of 0.005. Similarly, the flux ratio 0.0024 can be ruled out with 90% confidence.

5.5 Discussion

I consider the flux ratio from $1.55 \mu\text{m}$ to $1.65 \mu\text{m}$ as equivalent to that in the H -band because spectra of late M dwarfs between $1.4 \mu\text{m}$ and $1.7 \mu\text{m}$ are not marked by the very deep H_2O absorption that is characteristic of L spectral type dwarfs (e.g. Leggett et al., 2001). The 2MASS H -band magnitude of ρ CrB is 3.99. This is in excellent agreement with its *Hipparcos* V magnitude of 5.39, and the $V - H$ color of 1.36 for a GOV spectral type star (Cox, 2000, ch. 7). With the *Hipparcos* distance of 17.3 ± 0.2 pc, ρ CrB's absolute H -band magnitude is $M_H = 2.8$. The flux ratio upper bound (see 5.4.2) therefore corresponds to an H -band brightness limit for the companion of $M_H = 8.6$ at the 99% confidence level and $M_H = 9.3$ at the 90% confidence level.

Figure 5.5 shows the absolute H magnitude versus mass, 10 Gyr isochrone

¹See also <http://www.loujost.com>

calculated by Baraffe et al. (1998) for low mass stars and brown dwarfs, with the values for masses less than $0.1 M_{\odot}$ updated from Baraffe et al. (2003). At the scale of the figure, the 5 Gyr isochrone is indistinguishable from the one for 10 Gyr. I also plot the locations of main-sequence dwarfs whose masses have been measured dynamically; the references are cited in the figure caption. For reference, the figure shows the companion-to-primary flux ratio upper bounds calculated in Chapter 5.4. The flux ratio upper bound at the 99% confidence level, $\alpha = 0.005$, falls at $M \sim 0.15 M_{\odot}$, close to Gatewood et al. (2001)'s reported mass of the companion, $0.14 \pm 0.05 M_{\odot}$. Similarly, $\alpha = 0.0024$ sets an upper bound on the mass of $M \sim 0.11 M_{\odot}$ with 90% confidence. While these mass upper bounds do not provide either a definitive confirmation or rejection of Gatewood et al. (2001)'s reported companion mass, they do suggest strongly that the true mass is smaller than their value.

The analysis described in Chapter 5.3 and Chapter 5.4, and illustrated by the histograms in Figure 5.3 shows that by increasing the spectral range through the use of several orders the infrared spectroscopic technique can detect binaries with $1.6 \mu\text{m}$ flux ratios in the range of 0.01 to 0.02. This is a significant advance over previous detections at flux ratios of 0.04 to 0.05 (Mazeh et al., 2003).

5.6 Summary

1) The measurements set upper limits of 0.0024 and 0.005 on the ratio of the $1.6 \mu\text{m}$ flux of ρ CrB's companion to that of ρ CrB, at the 90% and 99% confidence levels, respectively.

2) Using Baraffe et al. (1998, 2003)'s calculations of the *H*-band mass versus luminosity relation, these flux limits correspond to mass upper bounds of $0.11 M_{\odot}$ and $0.15 M_{\odot}$ at the 90% and 99% confidence limits, respectively.

3) This analysis tested the sensitivity of the cross-correlation technique when using multiple orders. The results indicate that binaries with $1.6 \mu\text{m}$ flux ratios as low as 0.01 to 0.02 are detectable by high spectral resolution infrared spectroscopy.

Bibliography

- Baraffe, I., Chabrier, G., Allard, F., & Hauschildt, P. H. 1998, *A&A*, 337, 403
- Baraffe, I., Chabrier, G., Barman, T. S., Allard, F., & Hauschildt, P. H. 2003, *A&A*, 402, 701
- Bender, C., Simon, M., Prato, L., Mazeh, T., & Zucker, S. 2005, *AJ*, 129, 402
- Cox, A. N. 2000, *Allen's Astrophysical Quantities* (4th ed. New York; Springer)
- Delfosse, X., Forveille, T., Ségransan, D., Beuzit, J.-L., Udry, S., Perrier, C., & Mayor, M. 2000, *A&A*, 364, 217
- Fisher, R. A. 1932, *Statistical methods for research workers* (4th ed.; Edinburgh: Oliver and Boyd)
- Forveille, T., Beuzit, J.-L., Delfosse, X., Ségransan, D., Beck, F., Mayor, M., Perrier, C., Tokovinin, A., & Udry, S. 1999, *A&A*, 351, 619
- Gatewood, G., Han, I., & Black, D. C. 2001, *ApJ*, 548, L61
- Gatewood, G. D. 1987, *AJ*, 94, 213
- Han, I., Black, D. C., & Gatewood, G. 2001, *ApJ*, 548, L57
- Henry, T. J., Franz, O. G., Wasserman, L. H., Benedict, G. F., Shelus, P. J., Ianna, P. A., Kirkpatrick, J. D., & McCarthy, Jr., D. W. 1999, *ApJ*, 512, 864
- Henry, T. J. & McCarthy, Jr., D. W. 1993, *AJ*, 106, 773
- Leggett, S. K. 1992, *ApJS*, 82, 351
- Leggett, S. K., Allard, F., Geballe, T. R., Hauschildt, P. H., & Schweitzer, A. 2001, *ApJ*, 548, 908

- Leggett, S. K., Golimowski, D. A., Fan, X., Geballe, T. R., Knapp, G. R., Brinkmann, J., Csabai, I., Gunn, J. E., Hawley, S. L., Henry, T. J., Hindsley, R., Ivezić, Ž., Lupton, R. H., Pier, J. R., Schneider, D. P., Smith, J. A., Strauss, M. A., Uomoto, A., & York, D. G. 2002, *ApJ*, 564, 452
- Martin, C., Mignard, F., Hartkopf, W. I., & McAlister, H. A. 1998, *A&AS*, 133, 149
- Mazeh, T., Prato, L., Simon, M., Goldberg, E., Norman, D., & Zucker, S. 2002, *ApJ*, 564, 1007
- Mazeh, T., Simon, M., Prato, L., Markus, B., & Zucker, S. 2003, *ApJ*, 599, 1344
- McGrath, M. A., Nelan, E., Black, D. C., Gatewood, G., Noll, K., Schultz, A., Lubow, S., Han, I., Stepinski, T. F., & Targett, T. 2002, *ApJ*, 564, L27
- Noyes, R. W., Jha, S., Korzennik, S. G., Krockenberger, M., Nisenson, P., Brown, T. M., Kennelly, E. J., & Horner, S. D. 1997, *ApJ*, 483, L111
- Pourbaix, D. & Arenou, F. 2001, *A&A*, 372, 935
- Prato, L., Simon, M., Mazeh, T., McLean, I. S., Norman, D., & Zucker, S. 2002, *ApJ*, 569, 863
- Ségransan, D., Delfosse, X., Forveille, T., Beuzit, J.-L., Udry, S., Perrier, C., & Mayor, M. 2000, *A&A*, 364, 665
- Torres, G., Henry, T. J., Franz, O. G., & Wasserman, L. H. 1999, *AJ*, 117, 562
- Zucker, S. & Mazeh, T. 2001, *ApJ*, 562, 549

Table 5.1. Log of ρ CrB Observations

UT Date	Observing Mode	Total. Exp. (s)
2001 Jan 7	AO	640
2001 Feb 2	non-AO	960
2001 May 3	non-AO	840
2001 Jun 2	non-AO	840

Table 5.2. Measured Companion-to-Primary Flux Ratios at $1.6\ \mu\text{m}$

Observation Date	NIRSPEC Order	α
2001 Jan 7	46	-0.0100
	47	0.0125
	48	-0.0090
	49	-0.0046
2001 Feb 2	46	-0.0084
	47	0.0068
	48	-0.0114
	49	0.0164
2001 May 3	46	-0.0148
	47	0.0065
	48	-0.0148
	49	-0.0012
2001 Jun 2	46	-0.0260
	47	0.0118
	48	-0.0020
	49	-0.0054

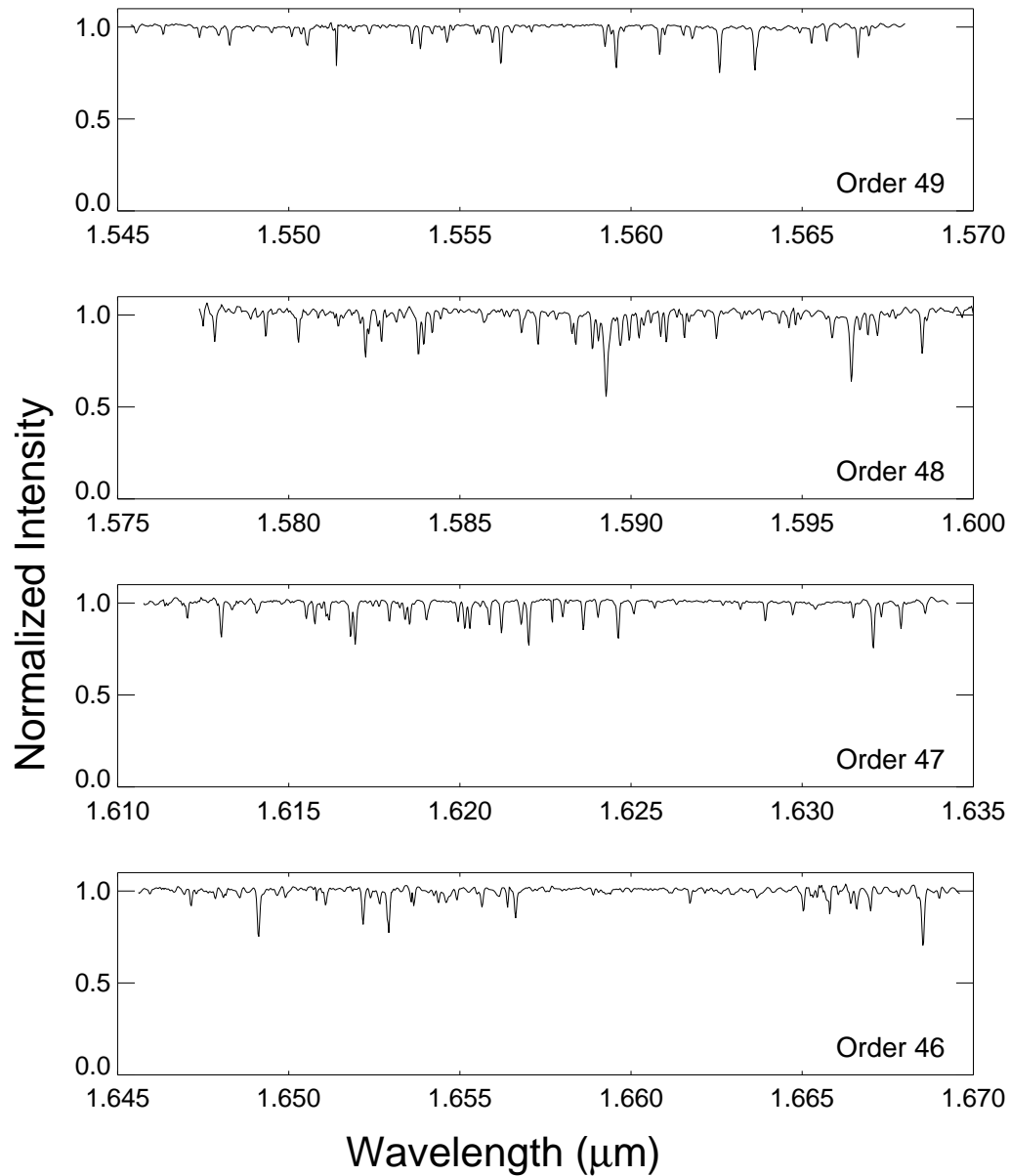


Figure 5.1 NIRSPEC spectrum of ρ CrB from 2001 June 2 for orders 46–49. The spectra have been flattened and normalized to their continuum levels. The terrestrial absorption lines in orders 46, 47, and 48 have been removed by ratioing with calculated spectra.

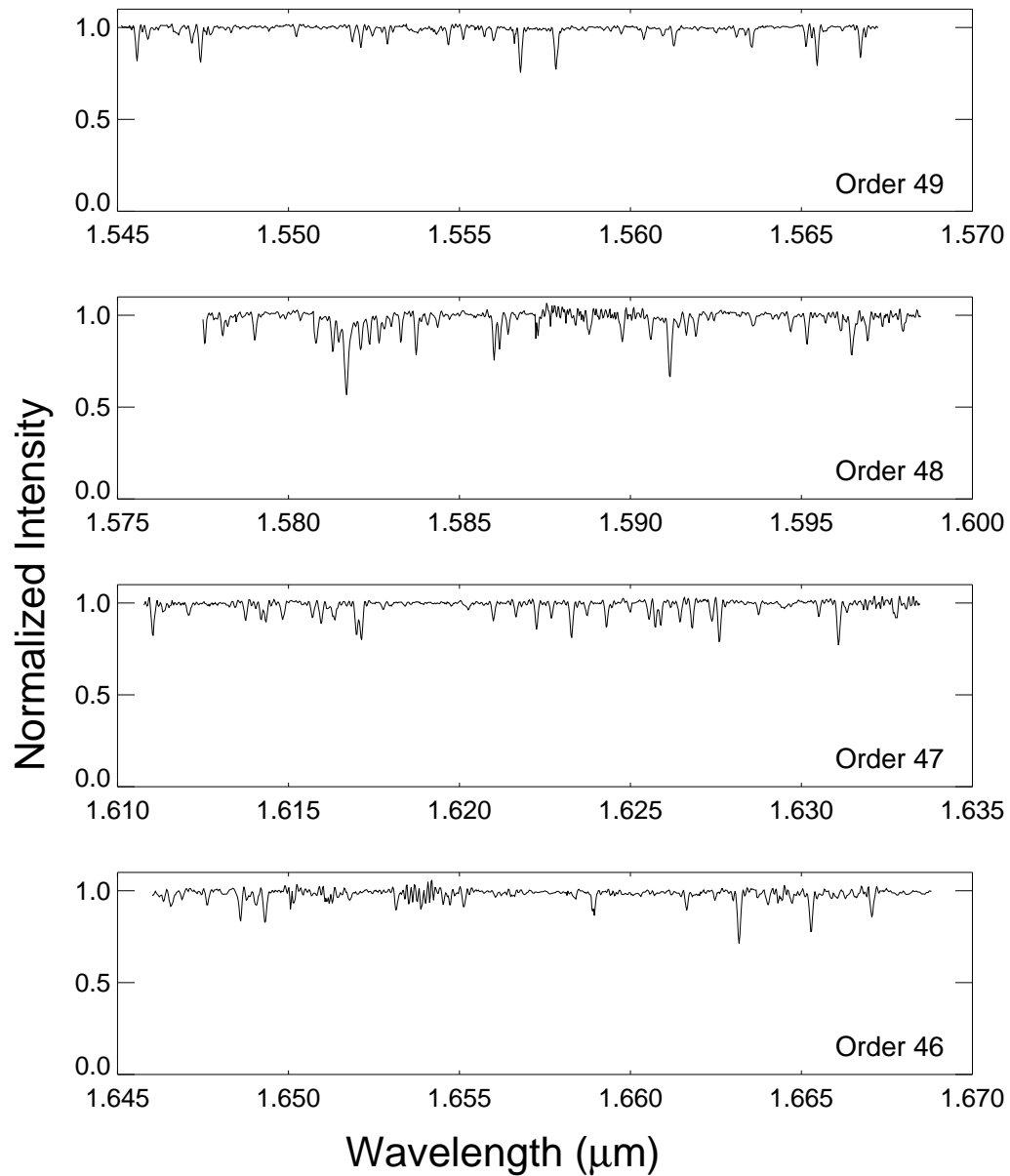


Figure 5.2 Sample primary spectra from the 2001 January 7 model set. The ρ CrB spectra were subdivided, at wavelengths with no spectral lines, into smaller sections with lengths 10 – 60 Å. The sections were reassembled randomly to create unique spectra with absorption lines, noise characteristics, and spectral range identical to the original ρ CrB spectra.

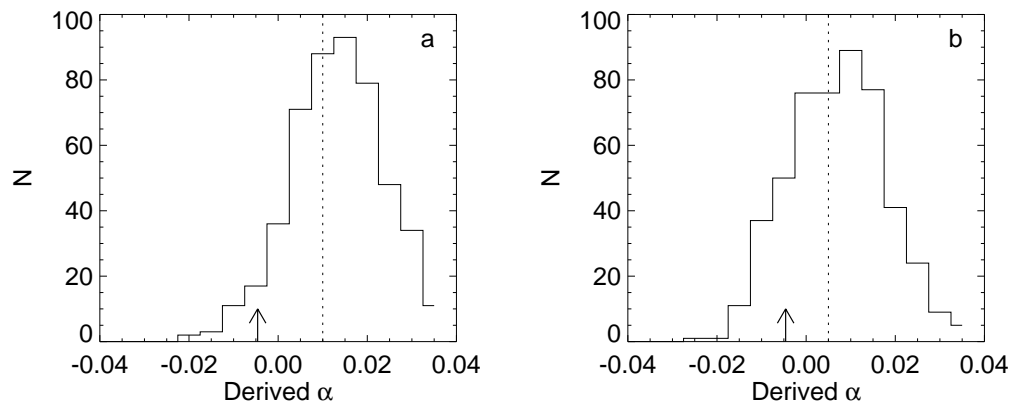


Figure 5.3 The distribution of derived flux ratios in a sample of 500 model binaries having the characteristics of the ρ CrB order 49 spectrum measured in 2001 January 7 and the companion Gl406 at flux ratio (a) $\alpha = 0.010$ and (b) $\alpha = 0.005$. The dashed line indicates the input α and the arrow the measured value of -0.0046 from (Table 5.2).

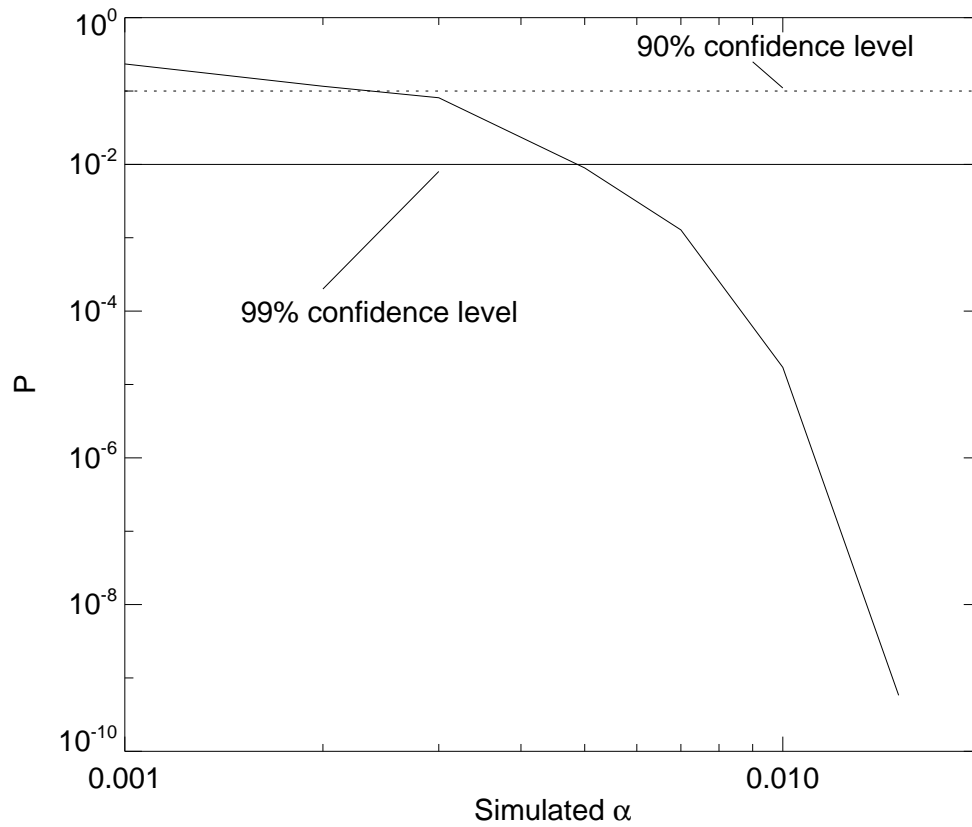


Figure 5.4 The curve shows the combined probabilities that my 16 measurements (four spectral orders on four occasions) have a flux ratio less than or equal to the measured value, as a function of the model binary input flux ratio. The straight lines with constant probability show the 90% and 99% confidence levels and intersect the curve of combined probabilities at flux ratios of 0.0024 and 0.005, respectively.

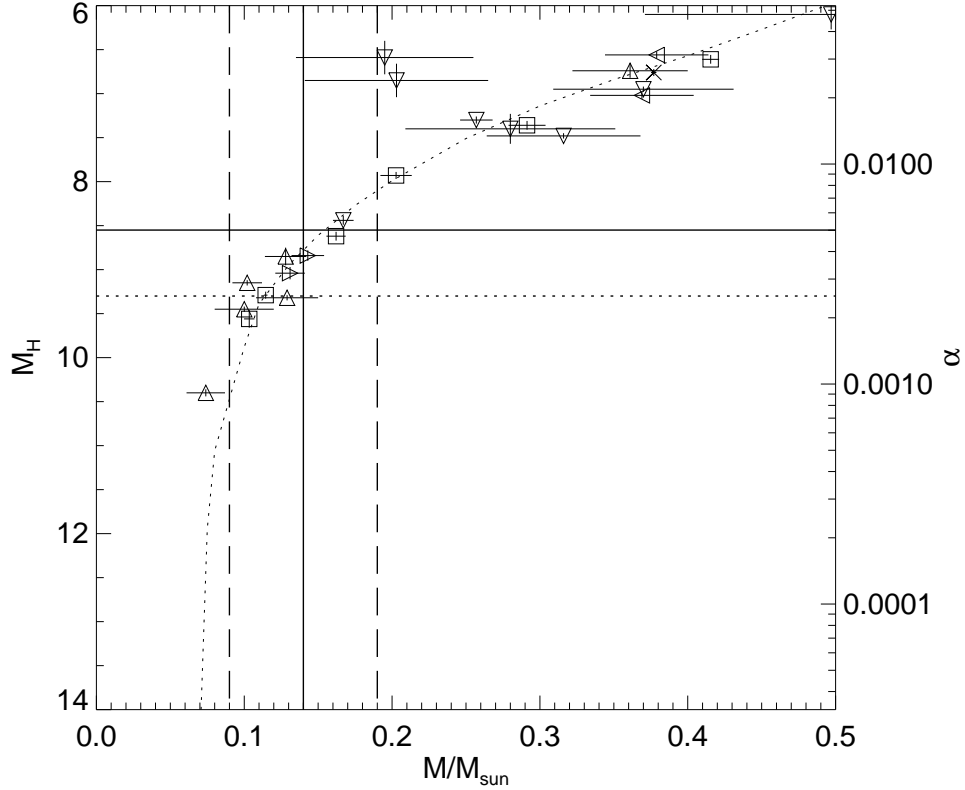


Figure 5.5 Absolute H -band magnitude versus mass; the companion-to-primary flux ratio at $1.6 \mu\text{m}$, α , is also shown for reference. The dotted curve corresponds to the 10 Gyr isochrone from Baraffe et al. (1998), with values for $M \leq 0.1 M_{\odot}$ updated by Baraffe et al. (2003). The vertical lines with constant mass represent the result and 1σ error estimate of Gatewood et al. (2001). The horizontal lines at $M_H = 8.6$ and $M_H = 9.3$ represent my flux ratio limits of 0.005 and 0.0024 for ρ CrB's companion at the 99% and 90% confidence limits, and correspond to mass upper bounds of $0.15 M_{\odot}$ and $0.11 M_{\odot}$, respectively. The data points are compiled from the literature and the symbols correspond to their source as follows: *upward-pointing triangles*, Henry et al. (1999); *downward-pointing triangles*, Henry & McCarthy (1993); *squares*, Ségransan et al. (2000); *crosses*, Forveille et al. (1999); *rightward-pointing triangles*, Torres et al. (1999); *leftward-pointing triangles*, Martin et al. (1998). The M_H values come from these and Delfosse et al. (2000), Leggett et al. (2002), and Leggett (1992).

Chapter 6

Closing Remarks

The investigations presented in Chapters 3–5 all use high resolution infrared spectroscopy and cross-correlation analyses. Each, however, uses the technique in a different way to address different scientific problems. In the Hyades binary analysis, I took advantage of the fact that the cluster members are extremely well studied. I sought to contribute only one small piece, namely K_2 for known SB1s. Because of that focused scope, I was able to measure a large sample of binaries in a relatively short amount of time, and subsequently derive a number of ancillary results. Similar analyses of other clusters would be scientifically interesting, but also potentially complicated if the cluster members lacked the extensive legwork that was available for the Hyades. Over the next decade, I expect that similar information will become available for a number of nearby clusters, and a better understanding of binary star formation, not just in a localized environment, but in a more global sense, will emerge.

In contrast to the Hyades, my study of Gl569 set out to completely analyze a unique, dynamical system. Our goal was to determine the most fundamen-

tal of stellar parameters, the individual component masses, by combining a full SB2 analysis with a well determined astrometric orbit. Precise measurements of very low mass stars and brown dwarfs are critical for constraining the models that describe these objects, yet only a handful of such measurements currently exist. As my discussion of the age of Gl569 demonstrates, models in this mass regime are still quite uncertain. Yet, they are utilized regularly in the literature to characterize a variety of observations. Many additional low mass binaries, with one or both components of brown dwarf mass, are now known (e.g. LP 349-25, 2MASS18457+25, LP415-20). Until recently, however, Gl569B held a singular advantage over most of them: Gl569A is an ideal natural guide star for an AO system. During the 2007A observing semester, the Keck II telescope is scheduled to operate for the first time NIRSPEC with the AO system *and* the Laser Guide Star (LGS)¹. Using the LGS, NIRSPEC with AO can target previously unobservable, isolated brown dwarf binaries with small velocity separations, and spatially resolve their components to more easily measure their radial velocities. I expect that with this new opportunity, many such targets will be the subject of long term spectroscopic monitoring, and precise masses will soon be available.

In the analysis of ρ CrB, I did not attempt to measure the motion of the companion, but instead predicted at what velocity it would lie and searched for a signal at that location. Although I did not detect the companion, the upper limit flux ratio that I achieved, 0.005 at 99% confidence, is nearly an order of magnitude more sensitive than the previous best result achieved by Mazeh and colleagues with the cross-correlation technique. If future improvements to the technique

¹<http://www2.keck.hawaii.edu/observing/instavail.html>

can increase the sensitivity an additional order of magnitude, then the direct detection of the light from extra-solar planets orbiting nearby stars is possible. More than 200 such planets are known indirectly, through observations of their host stars. Planned ground and space based facilities and instruments, including interferometers, coronagraphs, and other high contrast imagers, will eventually detect and characterize the light from these planets. However, the spectroscopic approach illustrated with ρ CrB offers the opportunity to detect some of them now, using instruments that are already available. During the coming semesters, I plan to carry out an investigation using high resolution infrared spectroscopy to search for predicted CO and CH₄ absorption in a sample of the brightest known extra-solar planets. My intent is to not only directly detect these planets, but to do so in a way that constrains current models of their atmospheric composition and improves estimates of their temperature and mass.